



LIBERATORIA PER L'ARCHIVIAZIONE DELLA TESI DI DOTTORATO

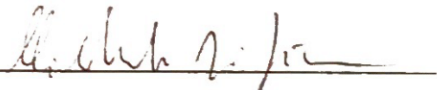
Al Magnifico Rettore
del Politecnico di Bari

Il sottoscritto Di Gioia Michele nato a Bitonto (BA) il 07/01/1995, residente a Bitonto (BA) in via Michele Larovere 11, e-mail michele.digioia@poliba.it, iscritto al 3° anno di Corso di Dottorato di Ricerca in Industria 4.0 ciclo XXXVI ed essendo stato ammesso a sostenere l'esame finale con la prevista discussione della tesi dal titolo: "Development of compact electronics for optical sensors based on photoacoustic spectroscopy for the detection of gas traces".

DICHIARA

- 1) di essere consapevole che, ai sensi del D.P.R. n. 445 del 28.12.2000, le dichiarazioni mendaci, la falsità negli atti e l'uso di atti falsi sono puniti ai sensi del codice penale e delle Leggi speciali in materia, e che nel caso ricorressero dette ipotesi, decade fin dall'inizio e senza necessità di nessuna formalità dai benefici conseguenti al provvedimento emanato sulla base di tali dichiarazioni;
- 2) di essere iscritto al Corso di Dottorato di ricerca Industria 4.0 ciclo XXXVI corso attivato ai sensi del "Regolamento dei Corsi di Dottorato di ricerca del Politecnico di Bari", emanato con D.R. n.286 del 01.07.2013;
- 3) di essere pienamente a conoscenza delle disposizioni contenute nel predetto Regolamento in merito alla procedura di deposito, pubblicazione e autoarchiviazione della tesi di dottorato nell'Archivio Istituzionale ad accesso aperto alla letteratura scientifica;
- 4) di essere consapevole che attraverso l'autoarchiviazione delle tesi nell'Archivio Istituzionale ad accesso aperto alla letteratura scientifica del Politecnico di Bari (IRIS-POLIBA), l'Ateneo archiverà e renderà consultabile in rete (nel rispetto della Policy di Ateneo di cui al D.R. 642 del 13.11.2015) il testo completo della tesi di dottorato, fatta salva la possibilità di sottoscrizione di apposite licenze per le relative condizioni di utilizzo (di cui al sito <http://www.creativecommons.it/Licenze>), e fatte salve, altresì, le eventuali esigenze di "embargo", legate a strette considerazioni sulla tutelabilità e sfruttamento industriale/commerciale dei contenuti della tesi, da rappresentarsi mediante compilazione e sottoscrizione del modulo in calce (Richiesta di embargo);
- 5) che la tesi da depositare in IRIS-POLIBA, in formato digitale (PDF/A) sarà del tutto identica a quelle consegnate/inviata/da inviarsi ai componenti della commissione per l'esame finale e a qualsiasi altra copia depositata presso gli Uffici del Politecnico di Bari in forma cartacea o digitale, ovvero a quella da discutere in sede di esame finale, a quella da depositare, a cura dell'Ateneo, presso le Biblioteche Nazionali Centrali di Roma e Firenze e presso tutti gli Uffici competenti per legge al momento del deposito stesso, e che di conseguenza va esclusa qualsiasi responsabilità del Politecnico di Bari per quanto riguarda eventuali errori, imprecisioni o omissioni nei contenuti della tesi;
- 6) che il contenuto e l'organizzazione della tesi è opera originale realizzata dal sottoscritto e non compromette in alcun modo i diritti di terzi, ivi compresi quelli relativi alla sicurezza dei dati personali; che pertanto il Politecnico di Bari ed i suoi funzionari sono in ogni caso esenti da responsabilità di qualsivoglia natura: civile, amministrativa e penale e saranno dal sottoscritto tenuti indenni da qualsiasi richiesta o rivendicazione da parte di terzi;
- 7) che il contenuto della tesi non infrange in alcun modo il diritto d'Autore né gli obblighi connessi alla salvaguardia di diritti morali ed economici di altri autori o di altri aventi diritto, sia per testi, immagini, foto, tabelle, o altre parti di cui la tesi è composta.

Luogo e data BARI, 28/12/2023


Firma 

Il sottoscritto, con l'autoarchiviazione della propria tesi di dottorato nell'Archivio Istituzionale ad accesso aperto del Politecnico di Bari (POLIBA-IRIS), pur mantenendo su di essa tutti i diritti d'autore, morali ed economici, ai sensi della normativa vigente (Legge 633/1941 e ss.mm.ii.),

CONCEDE

- al Politecnico di Bari il permesso di trasferire l'opera su qualsiasi supporto e di convertirla in qualsiasi formato al fine di una corretta conservazione nel tempo. Il Politecnico di Bari garantisce che non verrà effettuata alcuna modifica al contenuto e alla struttura dell'opera.
- al Politecnico di Bari la possibilità di riprodurre l'opera in più di una copia per fini di sicurezza, back-up e conservazione.

Luogo e data BARI, 28/12/2023

Firma 



Politecnico
di Bari

Department of Electrical and Information Engineering
ELECTRICAL AND INFORMATION ENGINEERING

INDUSTRY 4.0 Ph.D. Program

SSD: ING-INF/01–ELECTRONICS

FIS/03 – MATERIALS PHYSICS

Final Dissertation

Development of compact electronics
for optical sensors based on
photoacoustic spectroscopy for the
detection of gas traces

by

Michele Di Gioia:

Supervisors:

Prof. PATIMISCO Pietro

Prof. MARZOCCA
Cristoforo

Coordinator of Ph.D Program:

Prof. Ciminelli Caterina

Course n°36, 01/11/2020-31/10/2023



Politecnico
di Bari

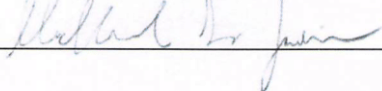
Department of Electrical and Information Engineering
ELECTRICAL AND INFORMATION ENGINEERING
INDUSTRY 4.0 Ph.D. Program
SSD: ING-INF/01–ELECTRONICS
FIS/03 – MATERIALS PHYSICS

Final Dissertation

Development of compact electronics
for optical sensors based on
photoacoustic spectroscopy for the
detection of gas traces

by

Michele Di Gioia :



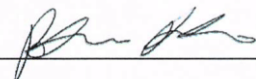
Referees:

Eng. CHALIKIAS
Nikolaos

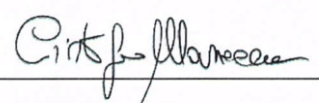
Prof. D'AMICO
Stefano

Supervisors:

Prof. PATIMISCO Pietro

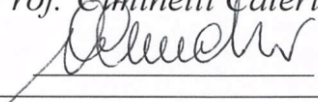


Prof. MARZOCCA
Cristoforo



Coordinator of Ph.D Program:

Prof. Giminelli Caterina



Summary

Introduction	3
Chapter 1: Quartz Enhanced Photoacoustic Spectroscopy	7
1.1 Fundamentals of Quartz Enhanced Photoacoustic Spectroscopy technique..	7
1.1.1 Wavelength modulation detection	11
1.1.2 Amplitude modulation detection for broadband absorbers	13
1.1.3 QEPAS with custom quartz tuning forks (QTFs)	14
1.2 QTF modeling	15
1.2.1 Mechanical model of a QTF	15
1.2.2 Electrical model of a QTF	17
1.3 Influence of pressure on QTF properties	20
Chapter 2: Front-end preamplifiers for QEPAS sensors	23
2.1 Signal conditioning chain of a QTF	23
2.2 Thevenin equivalent model of a QTF	26
2.3 Preamplifier configurations	30
2.3.1 Voltage amplifier	30
2.3.2 Transimpedance amplifier	44
2.3.3 Charge sensitive amplifier	53
Chapter 3: Lock-in Amplifier modeling for noise analysis	59
3.1 LIA working principle.....	59
3.2 Modeling of the lock-in filter	61
3.3 Influence of lock-in amplifier time constant in the three configurations.....	64
3.3.1 Voltage amplifier	65
3.3.2 Transimpedance amplifier	73
3.3.3 Charge sensitive amplifier	80
Chapter 4: Results	90
4.1 QEPAS sensor.....	90
4.1.1 Experimental setup	90
4.1.2 Measurements of resonance frequency and quality factor	92
4.2 Extraction of the electrical parameters of a QTF	98
4.3 QEPAS sensor with TIA for QTF readout.....	100

4.3.1 Experimental setup	100
4.3.2 Signal measurements	103
4.3.3 Noise measurements	106
4.4 QEPAS sensor with CSA for QTF readout.....	109
4.4.1 Signal measurements	109
4.4.2 Noise measurements	112
Chapter 5: Fully differential front-end, a further improvement	116
5.1 Architecture of a fully differential amplifier.....	116
5.2 Fully differential amplifiers for QTF readout	122
5.2.1 Fully differential transimpedance amplifier	122
5.2.2 Fully differential charge sensitive amplifier	125
5.2.3 Signal-to-noise ratio measurement with a fully differential CSA	127
Conclusions and future perspectives	130
Appendix.....	132
A.1 Fitting algorithm for the extraction of the electrical parameters of a QTF	132
A.1.1 Series and parallel resonant frequency of the QTF	132
A.1.2 Solving the system	132
A.1.3 Converting the parameters to double format	133
A.2 Measurement of the absolute humidity	133
A.2.1 Code running on the SERVER board	134
A.2.2 Code running on the CLIENT board	138
Bibliography	140

Introduction

Since the first decade of the 21st century, the rise of “Industry 4.0” technologies played a fundamental role in the automation of industrial processes. Thanks to the extraordinary developments of Internet of Things (IoT) and telecommunication industries, it is possible to significantly improve the quality of the production and optimize the deployment of human operators in the industrial environment. The core of the innovation introduced by Industry 4.0 is represented by the growing use of sensors in the industrial production chain. Indeed, sensors are useful to improve product quality and decrease production costs, thus allowing a more rapid production of quality goods [1-4]. In this way, human error is minimized, and the quality of production can be increased with minimum monitoring [5,6].

Among the different types of sensors, trace gas sensors play a crucial role in several industrial fields, such as oil and gas (O&G) field [7], industrial process control analysis [8] and environmental monitoring [9]. In particular, the market volatility in the O&G sector, induced by the recent COVID-19 pandemic, and the need for alternative green energy are leading the industry towards new forms of innovation [10]. Furthermore, major issues are represented by the cost of operations, such as the exploration and development of new O&G deposits, the lack of advanced monitoring systems, and environmental contamination deriving from crude oil production. Industrial applications require wide dynamic range of detection as well as real-time and in-situ monitoring of hazardous gases. For instance, hydrogen sulfide (H_2S) is often produced in oil fields, with a concentration ranging from part-per-million (ppm) to percentage levels [11]. According to the Occupational Safety and Health Administration (U.S. Department of Labor) the acceptable concentration limit for exposure to H_2S is 20 ppm for an eight-hour period [12]; higher concentrations can cause instant death [13]. Moreover, high concentrations of methane (CH_4) are transported through pipelines in O&G industries. Since leakages may occur in pipes, high concentrations of methane could escape and diluted with surrounding air. Consequently, trace gas sensors can be employed to detect the variation of CH_4

concentration in the air for safety, and to identify the location of the leakage.

Different types of gas sensors for trace gas detection can be listed, depending on their physical working principle: analytical sensors (gas-chromatography and mass spectrometers), electrochemical sensors and laser optical absorption sensors [14]. Analytical sensors are expensive, invasive, and bulky. Electrochemical sensors can be relatively specific to individual gas, have resolutions of gas concentration up to ppm, and are characterized by low power consumption. However, they experience hysteresis and suffer from humidity. Furthermore, they show a very slow response time, hence they are not suitable for real-time applications [14].

Optical techniques based on laser absorption spectroscopy (LAS) for trace gas sensing, compared to other techniques, are considerably faster with response times lower than 1 s, suffer from minimal drift, offer high gas specificity, and permit real time in-situ measurements. Direct LAS techniques are mainly based on light absorption ruled by the Lambert-Beer's law. Among the indirect LAS techniques [14,15], photoacoustic spectroscopy (PAS) is one of the most innovative and sensitive optical techniques for gas sensing. PAS is based on the detection of acoustic waves, which results from the absorption of modulated light in a specific targeted gas. Light absorbed excites a fraction of the ground-state molecular population into higher energy levels. These excited states subsequently relax through a combination of radiative and non-radiative pathways. No-radiative relaxations cause a local heating which in turn generates pressure waves that propagate far from the source. These weak sound waves can be detected by a microphone. The targeted gas is enclosed inside a resonant acoustic cell. The quality factor Q and the resonance frequency of an acoustic resonator typically fall in the ranges of 40-200 and 1-4 kHz, respectively. PAS does not require an optical detector because the sound wave generation is wavelength-independent. Other advantages include small size of the detection module, large linear dynamic range (from few % to part-per-trillion concentration range), and long-term stability [16]. These advantages make the PAS technology competitive with, and in many cases, preferred to, other trace gas sensing methods.

A significant improvement of the PAS technique was made by replacing the

microphone with a high- Q factor piezoelectric quartz tuning fork (QTF) with a resonance frequency close to 32.7 kHz. This frequency refers to the fundamental in-plane flexural mode in which the QTF prongs vibrate in opposite directions (antisymmetric vibrational mode). Its Q -factor is 100,000 in vacuum and $>10,000$ at normal atmospheric pressure. QTF-based PAS is referred to as quartz-enhanced photoacoustic spectroscopy (QEPAS).

In a QEPAS sensor, the minimum detection limit is strictly related to the signal-to-noise ratio (SNR), which, in turn, is influenced by the noise level of the readout electronics. In a standard QEPAS experiment, suitable analog front-end (AFE) electronics is needed, in order to readout the signal generated by the QTF. Typically, the AFE consists of a preamplifier, which boosts the current signal generated on the QTF by the piezoelectric effect, followed by a lock-in amplifier (LIA), needed to extract the desired harmonic component and to get rid of the unwanted noise. Thus, a proper design of both stages is mandatory to fully exploit the QEPAS technique.

My research activity was focused on the improvement of the state-of-art signal conditioning chain of a QEPAS sensor. In particular, initial efforts were focused on the study of different QTF configurations, and on the investigation of the influence of the pressure on the QTF properties. Then, a detailed study on the different preamplifier configurations which can be employed as QTF front-end electronics was conducted, together with an analysis of the impact of the LIA parameters on the overall SNR. Finally, a custom printed circuit board (PCB) was designed and tested in order to evaluate the pressure dependency of the SNR.

This thesis work is organized as follows:

- **Chapter 1:** In this section, the fundamentals of QEPAS technique are presented, focusing on the main detection schemes, and the mechanical and electrical model of a QTF is introduced. In addition, the influence of the pressure on the resonant frequency and quality factor of a T-shaped QTF coupled to a pair of resonator tubes is investigated, and a theoretical model is presented.
- **Chapter 2:** A brief description of the signal conditioning chain of a QTF is provided. Three different preamplifier configurations are presented (i.e.,

voltage, transimpedance and charge sensitive amplifier), with the modeling of signal and noise transfer functions. An analytical model was developed and then validated by means of SPICE simulations.

- **Chapter 3:** In this section, the working principle of the lock-in amplifier is described, and a behavioral model of a lock-in filter is proposed and compared with the outcome of SPICE simulations. A study of the influence of the lock-in filter time constant in each preamplifier configuration is presented and discussed.
- **Chapter 4:** In this section, measurements of the resonance frequency and quality factor of a T-shaped QTF are presented, in order to validate the theoretical model presented in the first chapter. Then, the pressure dependence of a standard QTF impedance is investigated. Finally, measurements of the SNR as a function of the pressure, employing both a transimpedance and a charge sensitive amplifier, are presented. Finally, a custom PCB implementing both configurations was assembled and employed as AFE in a QEPAS sensor for water vapor detection in laboratory air.
- **Chapter 5:** The advantages of a fully differential amplifier as QTF readout electronics are discussed in this last section. SPICE simulations of the SNR obtained with fully differential amplifier configurations are also shown. Then, a QEPAS experiment with a fully differential charge sensitive amplifier is presented, highlighting a remarkable improvement with respect to the results obtained employing a single-ended configuration.

Chapter 1: Quartz Enhanced Photoacoustic Spectroscopy

In this chapter, the working principles of Quartz Enhanced Photoacoustic Spectroscopy sensors are described. Then, the modeling of mechanical and electrical properties of the sensitive element is presented, together with a theoretical analysis of the influence of the pressure on the resonance properties of a Quartz Tuning Fork.

1.1 Fundamentals of Quartz Enhanced Photoacoustic Spectroscopy technique

Quartz-enhanced photoacoustic spectroscopy (QEPAS) is an alternative approach to photoacoustic detection of trace gas utilizing a quartz tuning fork (QTF) as a sharply resonant acoustic transducer to detect weak photoacoustic excitation and allowing the use of extremely small volumes [17,18]. Such an approach removes restrictions imposed on the gas cell by the acoustic resonance conditions. A quartz crystal is a natural candidate for such an application because it is a low-loss and low-cost piezoelectric material. High- Q quartz crystals are employed as a frequency standard in clock, watches and smart phones. Usually, QTFs with a resonant frequency of 2^{15} or ~ 32768 Hz are used. QTFs possess a quality factor $Q \approx 100,000$ or higher when encapsulated in vacuum and a $Q \approx 10,000$ at normal atmospheric pressure. Therefore, the corresponding energy accumulation time at atmospheric pressure is $t \approx 320$ ms.

Acoustically, QTF is a quadrupole, which provide good environmental noise immunity. In fact, the width of the QTF resonance at normal pressure is ~ 4 Hz, so only frequency components in this narrow spectral band can produce efficient excitation of the QTF vibrations. Sound waves in air at 32 kHz have an acoustic wavelength ~ 1 cm, and thus, if produced by external acoustic sources, such waves tend to apply a force in the same direction on the two QTF prongs positioned at a ~ 1 mm distance. As a result, such sound waves do not excite the piezoelectrically active mode in which the two

prongs move in opposite direction and zero electrical response is produced. Hence, there is only one way to cause the QTF to resonate via the photoacoustic effect to produce sound waves from a source located between the two QTF prongs. The standard way to realize such a condition is for the excitation laser beam to pass through the gap between the prongs without touching them.

The generation of a photoacoustic wave involves the energy transfer from internal to translational molecular degrees of freedom. If a rotational-vibrational state is excited, a collision-induced vibrational to translation (V-T) relaxation follows, with a time constant that for a particular molecule is dependent on the presence of other molecules and intermolecular interactions. QEPAS measurements are usually performed at a detection frequency of about 32 kHz and are more sensitive to the V-T relaxation rate compared to the conventional PAS which is commonly performed at $f_0 < 4$ kHz. In case of slow V-T relaxation with respect to the modulation frequency, the thermal waves in the gas cannot follow fast changes of the laser induced molecular vibration excitation. Thus, the generated photoacoustic wave is weaker than it would be in case of fast V-T energy equilibration [19]. For instantaneous V-T relaxation, the detected photoacoustic signal can be expressed as follows:

$$S \propto \frac{Q \cdot P \cdot \alpha}{f_0} \quad (1.1)$$

where f_0 is the QTF resonance frequency, Q its quality factor, α is the gas target absorption coefficient, and P is the laser power. Q typically ranges from 10^4 to 10^5 , depending on the carrier gas and the gas pressure.

The performance of QEPAS-based sensors can benefit from the consistently improved output powers of commercially available near infrared, mid-infrared, and far infrared lasers due to the technology developments by the semiconductor industry. Significant enhancements of the QEPAS signal-to-noise ratio have also been obtained as a result of the implementation of micro-resonators (mR). A mR is formed by one or two thin tubes and the QTF is positioned either between (on-beam QEPAS [20-24]) or adjacent to the tube(s) (off-beam QEPAS [25-30]) to probe the acoustic vibration excited in the gas contained inside the tubes. A sub system composed of the QTF and

the mR is called a spectrophone or acoustic detection module (ADM). In both on-beam or off-beam sensor configurations, it is critical that the photoacoustic exciting radiation does not hit the ADM, as otherwise an undesirable background that can be several times larger than the QTF thermal noise level arises, with a shifting fringe-like interference pattern shape, which limits the detection sensitivity [31,32]. A schematic of a typical QEPAS setup, as used in most reported QEPAS sensor systems, is shown in Fig. 1.1.

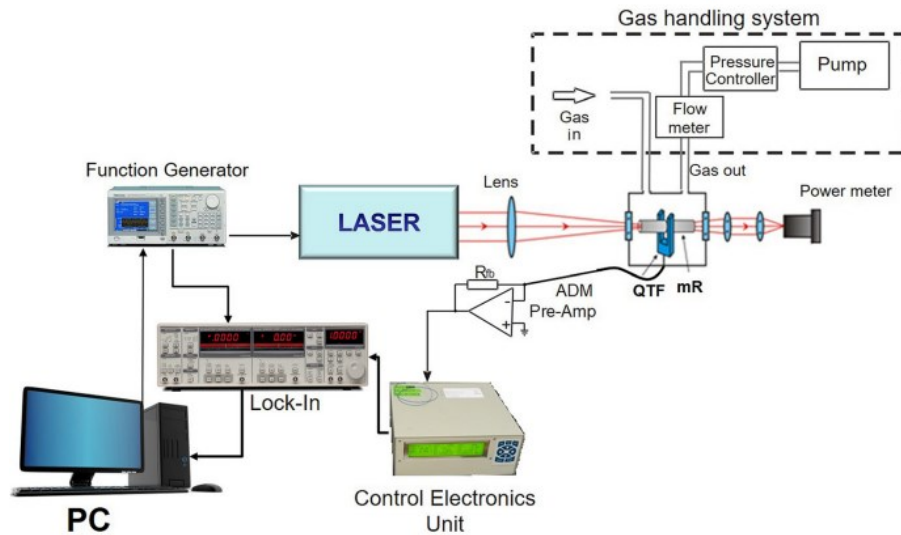


Figure 1.1 Schematic of a typical QEPAS sensor setup. QTF, quartz tuning fork; mR, acoustic micro-resonator; ADM, acoustic detection module; PC, personal computer.

A laser source, typically a quantum cascade laser (QCL) or an interband cascade laser (ICL), serves as the excitation source for generating the QEPAS signal. The ADM is mounted inside a vacuum-tight cell equipped with optical windows. The laser beam is focused by a lens between the QTF prongs and it passes through the ADM. A power meter is used for monitoring the laser power as well as for optical alignment. A function generator is used to sinusoidally dither the laser current at the QTF resonance frequency or one of its subharmonics. The flow rate and pressure of the sample gas passing through the ADM can be controlled and maintained by using a flow meter and pressure controller, respectively. A control electronics unit (CEU) is used to determine the main QTF parameters: dynamic resistance R , quality factor Q , and resonant frequency f_0 . The CEU is also designed to pass on the amplified signal from a transimpedance pre-

amplifier (Pre-Amp) to the lock-in amplifier to demodulate the QEPAS signal. A picture of an ADM is shown in Fig. 1.2.



Figure 1.2 Photograph of an ADM. An optical window and the gas inlet and outlet connectors are also visible.

QEPAS based sensor systems are usually operated with a wavelength modulation (WM) and $2f$ detection configuration in order to suppress background noise originating from spectrally nonselective absorbers (such as the mR, QTF, and the optical windows of the ADM). One important advantage of WM is that only the noise centered within the detection bandwidth will affect trace-gas measurements. In WM, the laser beam is wavelength modulated at $f_0/2$ frequency and the lock-in amplifier demodulates the QTF response at f_0 .

Spectral data can be acquired when the laser wavelength is scanned. For broadband gas species with unresolved rotational spectral structure, the WM approach is not usable since the laser source cannot be wavelength modulated with a sufficient spectral tuning coverage. Thus, the only possibility is to operate in an amplitude modulation (AM) configuration, where the laser is modulated at f_0 and the QEPAS signals are detected by the lock-in amplifier at the same f_0 frequency. Unlike WM QEPAS, AM QEPAS is not background free. However, this AM QEPAS background can be stable over several hours and hence allows background subtraction [33-35].

1.1.1 Wavelength modulation detection

The wavelength modulation (WM) technique is generally used to improve the QEPAS SNR and to minimize external acoustic noise for a QEPAS based sensor system. The WM description is based on an intensity representation of an optical wave, so that only the absorption of the sample is considered and dispersion effects due to the sample can be neglected. The description is based on the instantaneous laser frequency:

$$\nu(t) = \nu_0 - \Delta\nu \cdot \cos(\omega t) \quad (1.2)$$

where ν_0 is the optical carrier frequency and $\omega = 2\pi f$ is the modulation angular frequency due to the laser injection current modulated at the same angular frequency. In addition to frequency modulation, the current waveform applied to the QCL produces a sinusoidal modulation of the laser intensity and is given by:

$$I(t) = I_0 + \Delta I \cdot \cos(\omega t) \quad (1.3)$$

The amplitude ΔI of the sinusoidal intensity modulation is determined by the slope of the laser power versus the current characteristics, which is assumed constant across a wavelength scan. The instantaneous laser frequency interacts with the absorption feature. Expanding the absorption coefficient $\alpha(\nu(t))$ for a small $\Delta\nu$ we obtain:

$$\begin{aligned} \alpha(\nu(t)) = & \alpha_0 + \left. \frac{\partial \alpha}{\partial \nu} \right|_{\nu=\nu_0} \Delta\nu \cos(\omega t) \\ & + \left. \frac{1}{2} \frac{\partial^2 \alpha}{\partial \nu^2} \right|_{\nu=\nu_0} (\Delta\nu)^2 \cos^2 \omega t + \dots \end{aligned} \quad (1.4)$$

where α_0 can be considered to be the background absorption contribution. The laser is modulated both in intensity and in wavelength simultaneously. Thus, assuming a small absorption I_{abs} , from the Lambert-Beer law we have:

$$\begin{aligned} I_{abs}(t) = & [I_0 + \Delta I \cos(\omega t)] \\ & \cdot \left[1 - L \left(\alpha_0 + \left. \frac{\partial \alpha}{\partial \nu} \right|_{\nu=\nu_0} \Delta\nu \cos(\omega t) \right. \right. \\ & \left. \left. + \frac{1}{2} \left. \frac{\partial^2 \alpha}{\partial \nu^2} \right|_{\nu=\nu_0} (\Delta\nu)^2 \cos^2 \omega t \right) \right] \end{aligned} \quad (1.5)$$

L is the effective length over which the absorption takes place to produce an acoustic wave detectable by the QTF (in other words, L is comparable with the thickness t_0 of the QTF). Hence, the $I\omega$ -signal, $S_{I\omega}$, is given by:

$$S_{1\omega} = L\Delta I\alpha_0 - L \left. \frac{\partial \alpha}{\partial \nu} \right|_{\nu=\nu_0} \Delta \nu \quad (1.6)$$

and the 2ω -signal $S_{2\omega}$ is given by:

$$S_{2\omega} = -L\Delta I \left. \frac{\partial \alpha}{\partial \nu} \right|_{\nu=\nu_0} \Delta \nu + \frac{I_0}{2} \left. \frac{\partial^2 \alpha}{\partial \nu^2} \right|_{\nu=\nu_0} (\Delta \nu)^2 \quad (1.7)$$

This result shows that the background absorption contributes to the $S_{1\omega}$, whereas it does not contribute to $S_{2\omega}$. If we assume that the absorption coefficient has a pure Lorentzian line-shape, $S_{1\omega}$ has a pure first derivative line-shape with a constant background; $S_{2\omega}$ consists of two terms: the first term, arising from a residual amplitude modulation is proportional to the first derivative, whereas the second is the second-derivative expression arising from the laser wavelength modulation. Hence, $S_{2\omega}$ is not a pure second derivative of the Lorentzian line-shape but is distorted by a contribution originating from the residual amplitude modulation. This distortion does not affect the peak position of $S_{2\omega}$ since the first derivative of the Lorentzian line-shape vanishes when $\nu = \nu_0$.

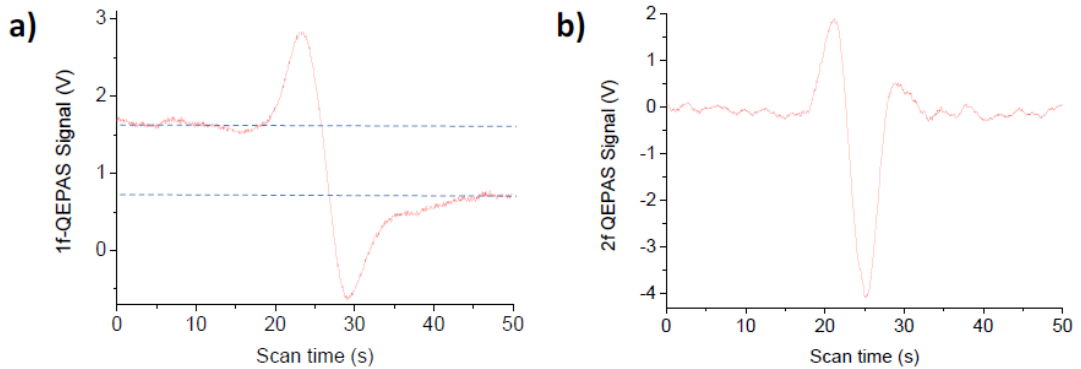


Figure 1.3 $1f$ -QEPAS (a) and $2f$ -QEPAS (b) spectral scans of 2.6 % of CO_2 in N_2 at a gas pressure of 50 Torr of a CO_2 line centered at $2,311.515 \text{ cm}^{-1}$. Blue lines highlight the strong background of the spectral $1f$ -QEPAS acquisition.

The generated QEPAS signal is usually demodulated by means of a lock-in amplifier both at the fundamental frequency f or the successive harmonics nf . When the laser light is modulated at the resonant frequency f_0 and QEPAS signal is demodulated at the same frequency, the demodulated signal is usually called $1f$ -QEPAS signal, while

when the laser light is modulated at the $f_0/2$ and QEPAS signal is demodulated at f_0 , the demodulated signal is referred to as $2f$ -QEPAS signal. In this case, the QTF detects sound oscillations at the second harmonic of the modulation frequency caused by the double intersection of the absorption line by the laser line during a modulation period. In Fig. 1.3 $1f$ -QEPAS ($2f$ -QEPAS) spectral scan of a 2.6 ‰ of CO₂ in N₂ mixture is depicted at a total gas pressure of 50 Torr, obtained by current modulation at $f_0 = 32809.1 \text{ Hz}$ ($f_0/2 = 16504.55 \text{ Hz}$) and a peak-to-peak voltage amplitude of 2.8 V acquired by using a bare QTF (i.e., without mR tubes) and a CW DFB QCL targeting the CO₂ (01¹1)–(01¹0) P(29) rotational-vibrational transition centered at 2,311.515 cm⁻¹ and with a line-strength of $7.458 \cdot 10^{-20} \text{ cm/mol}$.

A strong background signal was observed for the $1f$ approach, originating from stray light ending up on the walls of the acoustic detection module. This is confirmed by the observation that the amplitude of this offset strongly increases with a misalignment of the laser beam in lateral directions so that the beam wings touch the QTF. Instead, it was experimentally observed that the $2f$ approach is background-free. Distortions in the demodulated signal displaying an asymmetry on both sides of the spectrum around the peak (see Fig. 1.3b) can be associated to an amplitude intrinsic modulation contribution, which is introduced by current modulation. The laser wavelength modulation amplitude Δf and light intensity modulation ΔI must be optimized at each gas pressure for a highest $2f$ -QEPAS signal.

1.1.2 Amplitude modulation detection for broadband absorbers

Vibrational spectra of most molecules consisting of more than five atoms are so dense that infrared absorption spectra of such polyatomic molecules consist of 100–200 cm⁻¹ broad bands. Spectroscopic identification of these species requires laser excitation sources with a wide spectral coverage. However, distributed feedback (DFB) or Fabry-Perot (FP) QCLs cannot be wavelength modulated with a sufficient spectral tuning coverage for broadband absorption features. Thus, QEPAS detection of such molecules will require amplitude modulation (AM) of the laser radiation. The laser is operated at f_0 by means of square wave amplitude current modulation and the QEPAS signals are

detected by a lock-in amplifier at the same f_0 frequency. Unlike WM QEPAS, AM QEPAS is not background free. Residual absorption of laser radiation by the cell windows as well as scattered radiation absorbed inside the gas cell produce a sound at the QTF resonant frequency, thus generating a coherent background. However, this background can be stable over several hours, which allows background subtraction.

Typically, for every spectral point, both signal and background components normalized to the laser power are acquired. In post-processing, the in-phase and the quadrature components of the photoacoustic signal were calculated, respectively and by vector subtraction, it is possible to remove the background signal [33,34,36,37].

1.1.3 QEPAS with custom quartz tuning forks (QTFs)

Prior to 2013, all the QEPAS sensors reported in the literature employed commercial standard QTFs operating at the fundamental in-plane flexural resonant mode, with a frequency of ~ 32.7 kHz. However, the standard QTFs structure and its operating frequency were optimized for timing purposes and not for spectroscopic applications. Two main factors pose limitations to the use of standard QTFs for QEPAS sensing. First, the QEPAS signal depends strongly on the energy relaxation rates associated with the targeted gas species. The relaxation time constant τ_T depends on the specific molecule and on the specific gas carrier (typically either air or N₂) and intermolecular interactions. For gases, vibrational-translational (V-T) time constants τ_T fall typically in the μs temporal range [38]. To ensure that the energy transfer occurs efficiently for a fast modulation f of the incident laser radiation, it is necessary to satisfy the condition $f \ll 1/2\pi\tau_T$ [39]. Therefore, QEPAS is more sensitive to the energy relaxation rate compared to the conventional PAS, which is commonly performed at $f < 4$ kHz [40,41]. For gas species with a slow relaxation rate (such as CO, CO₂ and NO), the thermal waves in the gas cannot follow fast changes of the laser induced molecular vibration excitation. Thus, the generated photoacoustic wave is weaker than it would be in case of fast V-T energy equilibration [14]. Second, standard 32 kHz-QTFs are characterized by a small volume between their prongs ($\sim 0.3 \times 0.3 \times 3 \text{ mm}^3$). Hence, the use of light sources with a limited beam quality, like LED, a fiber amplified laser, or a

laser emitting in the THz spectral region ($\lambda > 30 \mu\text{m}$), is precluded, since they do not allow adequate focalization of the excitation beam between the prongs spaced by $\sim 300 \mu\text{m}$. The best method to circumvent these limitations is to employ QTFs with larger prongs spacing and operation frequencies possibly $< 20 \text{ kHz}$ to approach gas relaxation rates, but typically a decrease in f leads to a decrease of the resonance Q -factor [42], so that a trade-off optimization of the above parameters must be found.

1.2 QTF modeling

1.2.1 Mechanical model of a QTF

A QTF can be considered as two identical cantilevers coupled by a low-loss quartz bridge. A schematic of a QTF is shown in Fig. 1.4.

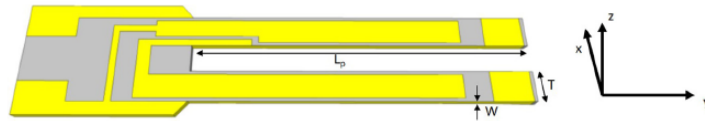


Figure 1.4 Schematic of a custom QTF with a gold contact pattern. The coordinate system with the y -axis parallel to the beam axis of the prong is depicted. In this way, the prongs bending for in-plane flexural modes occur in the xy -plane.

The in-plane flexural vibrations modes of the two prongs can be classified as in phase (symmetric) and out of phase (antisymmetric). The flexural antisymmetric modes, in which the two prongs oscillate in antiphase, are the only vibrational modes employed in QEPAS based sensor systems [43]. The resonance frequencies of the QTF can be calculated in the approximation of an independent cantilever vibrating in in-plane modes. The first two flexural modes are shown in Fig. 1.5.

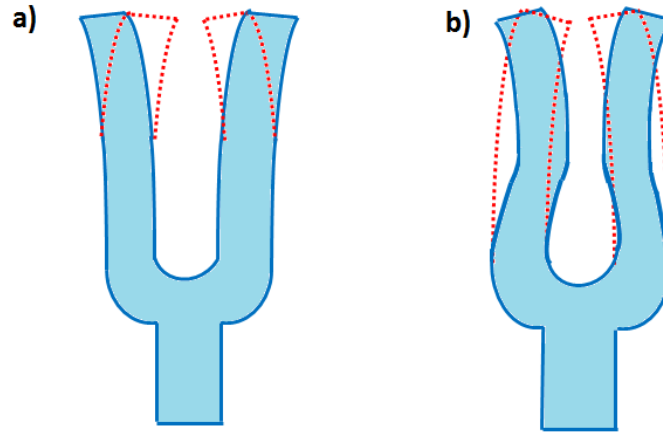


Figure 1.5 (a) First in-plane vibrational mode of a tuning fork. (b) Third in-plane vibrational mode of a tuning fork.

In the first flexural mode, the tines move in opposite directions and the center of mass of the QTF remains unchanged. The flexural mode vibration can be modeled by considering that each prong of the tuning fork behaves as a clamped beam. When the force is removed from the displaced beam, the beam will return to its original shape. Assuming the elastic modulus, inertia and cross-sectional area are constant along the beam length, the equation for that vibration is given by the following fourth-order differential equation, according to the Euler-Bernoulli approximation:

$$EI \frac{\partial^4 y}{\partial x^4}(x, t) + \rho A \frac{\partial^2 y}{\partial t^2}(x, t) = 0 \quad (1.8)$$

where ρ is the density of the material, E the Young modulus of the material, t is the time, $A = w \cdot y_0$ and x and y directions in the plane of the QTF. Equation 1.8 can be solved by separation of variables, assuming that the displacement can be separated into two parts; one that depends on position and the other on time. This leads to a simplified differential equation for the y direction that can be solved by superimposing boundary conditions. These boundary conditions come from the support of the QTF. The fixed end must have zero displacement and zero slope due to the clamp, while the free end cannot have a bending moment or a shearing force (free-clamped boundary conditions). The general solution is a linear combination of trigonometric equations leading to the frequency equation for the cantilever beam [44]:

$$\cos(k_n y_0) \cosh(k_n y_0) = -1 \quad (1.9)$$

where k_n are the wavenumbers related to the eigenfrequencies f_n , given by the following expression:

$$f_n = \frac{\pi K}{8y_0^2} \sqrt{\frac{E}{\rho}} n^2 \quad (1.10)$$

where $K = \left(\frac{1}{\sqrt{12}}\right) w_0$ and $n = \left(\frac{\rho A}{EI} \omega_n^2\right)^{\frac{1}{4}}$. U-shaped QTFs are mass-produced for timing application used in electronic clocks and smartphones. The standard QTF has a resonant frequency of ~ 32 kHz, with a gap between the prongs of ~ 300 μm , and prongs that are 3.2 mm long and 0.33 mm wide. Such QTFs have been widely used in all mid-IR QEPAS based sensors reported in the literature to-date, because of their commercial availability and ultra-low cost. Chromium/gold layer are deposited on both sides of the QTF to create electrodes, which collect the electrical charges induced by the mechanical deformation.

1.2.2 Electrical model of a QTF

QTFs can be designed to resonate at any frequency in the 4–200 kHz range and beyond, since resonance frequencies are defined by the properties of the piezoelectric material and by its geometry. The interaction between the laser modulated beam and a trace gas leads to the generation of acoustic waves that mechanically bend the QTF prongs. Hence, the electrode pairs of the QTF will be electrically charged due to the quartz piezoelectricity. Piezoelectricity is the coupling between internal dielectric polarization and strain, and is present in most crystals lacking a center of inversion symmetry. When a stress is applied to these materials, it induces a displacement of charge and a net electric field. The effect is reversible: when a voltage is applied across a piezoelectric material, it is accompanied by a strain. Due to this intrinsic coupling of strain and charge displacement a QTF can be modeled both mechanically and electrically (see Fig. 1.6).

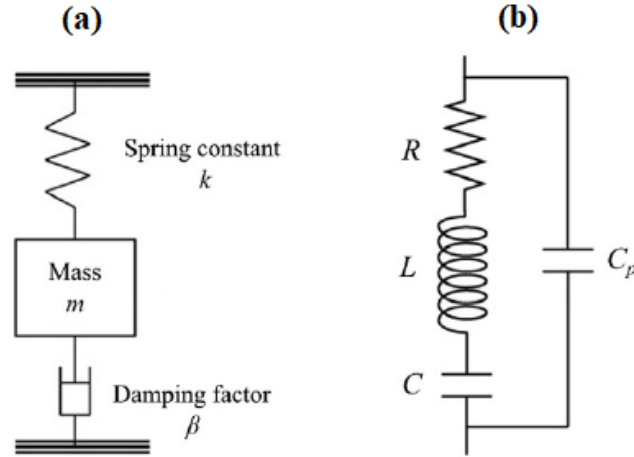


Figure 1.6 (a) Mechanical and (b) electrical model of a QTF. R , L , and C are the electrical resistance, inductance, and capacitance of the QTF, respectively. C_p is its parasitic capacitance. [45]

In particular, the electrical behavior of a QTF can be effectively described by the Butterworth-Van Dyke model (see Fig. 1.6b). In this way, the QTF parameters as a mechanical oscillator correspond to equivalent electrical parameters of a series RLC circuit: mass (m) to inductance (L), rigidity (k) to inverse capacity ($1/C$) and damping β to resistance R [17]. C_p is the parallel stray capacitance of the QTF. The resonant frequency is given by:

$$f_0 = \frac{1}{2\pi} \sqrt{\frac{1}{LC}} \quad (1.11)$$

and the quality factor is:

$$Q = \frac{1}{R} \sqrt{\frac{L}{C}} \quad (1.12)$$

The resonance properties of a QTF can be obtained by analyzing its response to a sinusoidal electrical excitation with amplitude V_0 . The electrical response of a QTF can be determined by solving the equivalent circuit [14,46] represented in Fig. 1.7.

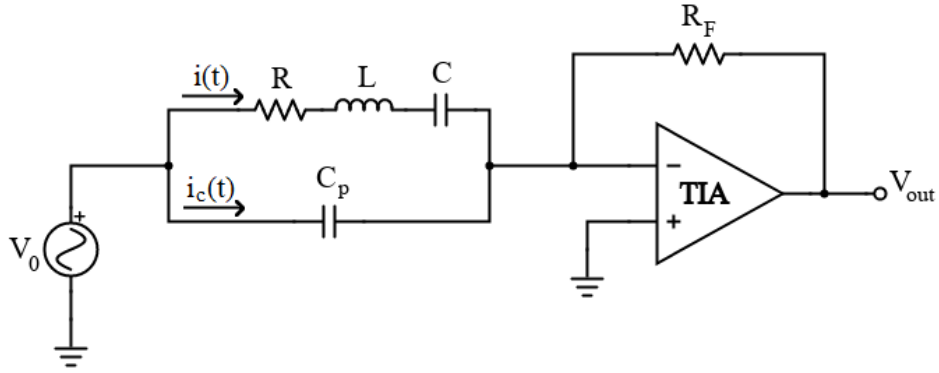


Figure 1.7 Equivalent circuit for QTF characterization. TIA is the transimpedance amplifier, R_F is the feedback resistor.

The current through the RLC circuit $i(t)$ is associated with the prong's vibration, whereas $i_c(t)$ is the stray current generated by C_p . The impedance Z of this circuit is given by:

$$\frac{1}{Z(\omega)} = j\omega C_p + \frac{1}{j\omega L + R + \frac{1}{j\omega C}} \quad (1.13)$$

The output current is given by the sum of $i(t)$ and $i_c(t)$ and is converted into a voltage signal by a transimpedance amplifier with a feedback resistor R_F . By solving the circuit represented in Fig. 1.7, the output signal amplitude V_{out} of the amplifier is retrieved as a function of the angular frequency of the excitation $\omega = 2\pi f$:

$$V_{out} = \frac{A\omega}{Q\omega_0} \frac{\sqrt{1 + 2C' \left(1 - \frac{\omega^2}{\omega_0^2}\right) + C'^2 \left(1 - \frac{\omega^2}{\omega_0^2}\right)^2 + C'^2 \left(\frac{\omega}{\omega_0 Q}\right)^2}}{\left(1 - \frac{\omega^2}{\omega_0^2}\right)^2 + \left(\frac{\omega}{\omega_0 Q}\right)^2} \quad (1.14)$$

where $A = V_0 \cdot R_F / R$; $Q = L \cdot \omega_0 / R$; $\omega_0 = 2\pi f_0$; and $C' = C_p / C$.

The output signal amplitude calculated by using Eq. 1.14 is plotted in Fig. 1.8a,b at different C' values while keeping A , Q and f_0 fixed, and (b) at different Q values while keeping A , C' and f_0 fixed.

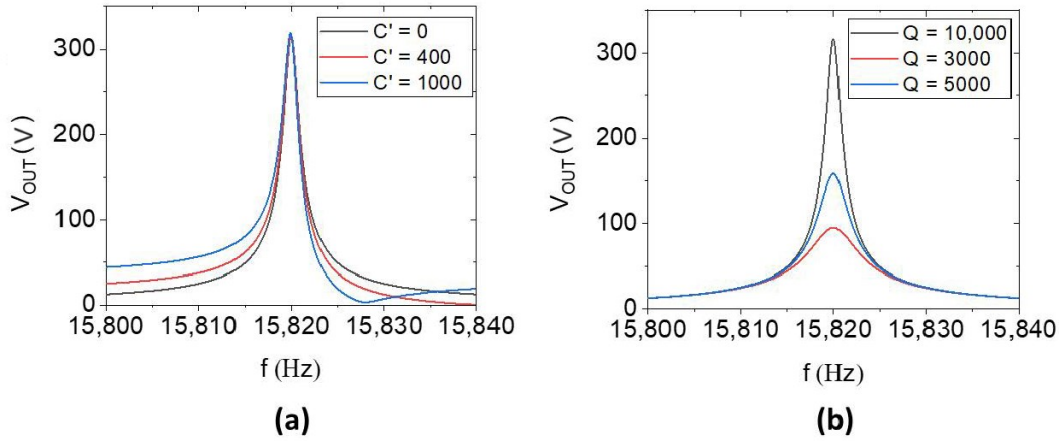


Figure 1.8 (a) Resonance curve of a QTF for different values of $C' = C_p/C$, with $A = 2 \cdot 10^{-8}$, $f_0 = 15820$ Hz, $Q = 10000$. (b) Resonance curve of a QTF for different values of Q with $A = 2 \cdot 10^{-8}$, $f_0 = 15820$ Hz, $C' = 0$. The output signals were obtained applying a $V_0 = 1$ V input signal.

All curves are characterized by a peak at the resonance frequency f_0 of the QTF. As C' , i.e., the stray capacitance, increases, the stray current creates a right-left asymmetry with respect to the peak value and a local minimum appears on the right side, as in the blue curve in Fig. 1.8a. In the case in which the stray capacitance can be neglected (black curve in Fig. 1.8a), the electrical response of the QTF can be represented by a Lorentzian line-shape. As the Q -factor increases (see Fig. 1.8b) the equivalent electrical resistance the QTF at the resonance decreases, leading to a higher resonance peak value, and the width at half maximum (FWHM) of the resonance curve decreases.

1.3 Influence of pressure on QTF properties

When the QTF is vibrating in air, the prong loses energy due to interaction with the surrounding medium. This effect can be modelled in the Euler–Bernoulli theory as an additional inertia caused by the motion of the molecules in the air and a viscous drag force acting on the prongs. Defining u as an additive mass per unit of length and C_d as the damping parameter, Equation 1.8 becomes [44]:

$$EI \frac{\partial^4 y}{\partial x^4}(x, t) + (\rho A + u) \frac{\partial^2 y}{\partial t^2}(x, t) + C_d \frac{\partial y(x, t)}{\partial t} = 0 \quad (1.15)$$

In the realistic case of a negligible damping, if $u \ll \rho A$, the additive mass causes a normalized shift on the frequency of the fundamental mode given by:

$$\Delta f = \frac{f'_0 - f_0}{f'_0} = \frac{u}{2\rho A} \quad (1.16)$$

where f_0 are the QTF resonance frequencies when prongs vibrate in air. In steady motion, the additive mass is proportional to the density of air ρ_{air} , thus $u = \rho_{air}$ [47]. According to the ideal gas law, $\rho_{air} = MP/R\Theta$, where $M = 28.964$ kg/mol is the molar mass, P is air pressure, $R = 62.3637$ m³ · Torr/K · mol is the gas constant, and Θ is the QTF temperature.

Air damping also affects the Q -factor of the QTF resonance mode. The contribution due to air damping was derived by Hosaka et al. [40]. In the viscous region, the dynamics can be described by the Navier–Stokes equation which leads to an expression for the Q -factor contribution Q_{air} related to air damping given by:

$$Q_{air} = \frac{4\pi\rho T w^2 f_0}{3\pi\mu w + \frac{3}{4}\pi w^2 \sqrt{4\pi\rho_{air}\mu} f_0} \quad (1.17)$$

where μ is the coefficient of the viscosity of air.

Thermoelastic and support losses are intrinsic dissipation mechanisms and can be assumed as pressure-independent. Hao et al. [48] developed a model to describe support losses as the effect of a shear force exerted from the vibrating beam on the QTF support, which excites elastic waves propagating into the support with a wavelength greater than the prong width w . With this assumption, the quality factor contribution Q_{sup} related to support losses can be simplified as:

$$Q_{sup} = A_n \frac{L^3}{T^3} \quad (1.18)$$

with the coefficients A_n depending on the n -th QTF resonance mode. Thermoelastic losses are due to the inhomogeneity of the stress field, which, in turn, causes an inhomogeneous, local increase in temperature. This temperature gradient is an additional channel of energy dissipation [49]. The corresponding Q -factor contribution Q_{TED} depends upon prong geometry and can be expressed as:

$$Q_{TED} \propto \frac{T^3}{L^2} \quad (1.19)$$

These theoretical models describe each loss mechanism as standalone and their dependence on the main physical parameters is explicated. Each loss contribution is independent from the other, but all occur simultaneously for a vibrating QTF prong.

Chapter 2: Front-end preamplifiers for QEPAS sensors

In Quartz Enhanced Photoacoustic Spectroscopy, a proper design of the quartz tuning fork (QTF) read-out electronics is required to optimize the signal-to-noise ratio (SNR), and in turn, to improve the minimum detection limit of the gas concentration [50]. The analog front-end (AFE) electronics usually employed in QEPAS experiments consists of a preamplifier, which boosts the signal level, followed by a lock-in amplifier (LIA), that retrieves the desired harmonic component and filters out the unwanted noise.

In this chapter, a brief overview of the signal conditioning chain of a QEPAS sensor is presented. Then, a theoretical study of the main preamplifier configurations employed as analog front-end for QTF is introduced, focusing both on the signal and noise characterization at the output of the different preamplifiers.

2.1 Signal conditioning chain of a QTF

The QTF acts as a piezoelectric sensor which transduces the mechanical strain induced by an acoustic wave into a current signal [51-53], which is in turn proportional to the concentration of the target gas [14,54,55]. Nevertheless, this signal must be properly processed by means of suitable front-end electronics, to provide useful information about the concentration of the detected analyte.

The first stage of the QTF signal conditioning chain consists of an analog preamplifier, which converts the piezo-current into a voltage signal which is amplified (through a gain factor) to increase the amplitude of the output signal. Operational amplifiers (OPAMPs) are usually employed as dedicated readout for QTFs [56], and can work as voltage amplifiers, charge sensitive amplifiers (CSA) or transimpedance amplifiers (TIA).

A sketch of the schematic of the main amplifier configurations is shown in Fig.

2.1.

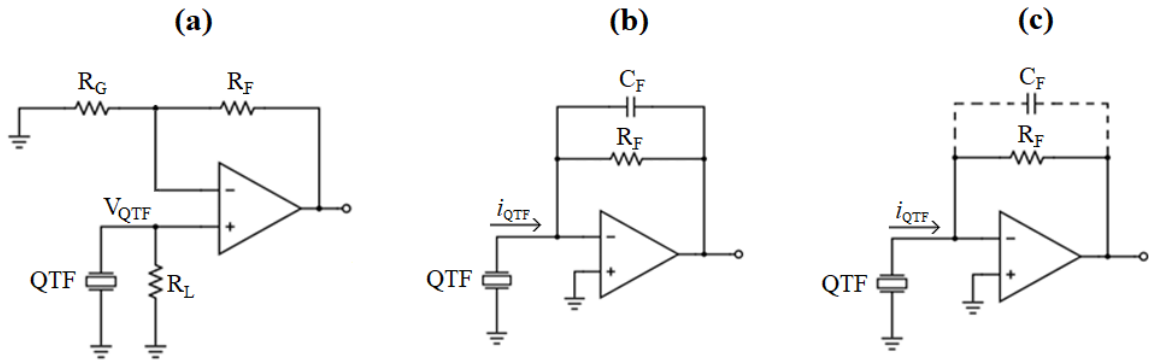


Figure 2.1 Basic preamplifier configurations for the readout of a quartz tuning fork: (a) voltage amplifier, (b) charge sensitive amplifier, (c) transimpedance amplifier.

The voltage amplifier (Fig. 2.1a) consists of an OPAMP used in non-inverting configuration; the voltage gain of the stage is determined by R_F and R_G resistors according to the following formula:

$$A_V = 1 + \frac{R_F}{R_G} \quad (2.1)$$

The resistor R_L is needed to bias the non-inverting input of the operational amplifier, since the QTF behaves as an open circuit at low frequencies.

Since the QTF behaves as a resistance around its resonance frequency, the use of a bias resistor is a generally accepted solution to convert the QTF piezo-current into a voltage signal [50,54,56]. The effects of the QTF stray capacitance could be limited employing a suitable compensation network [91,92]. Moreover, a capacitor could be added in series to R_G [60], to reduce the offset at the input of the OPAMP.

The charge sensitive amplifier (Fig. 2.1b) is an inverting amplifier in which the feedback network consists of the parallel connection of a resistor R_F and a capacitor C_F . The feedback resistor is needed to close the feedback loop at DC and to provide a discharge path to C_F , thus preventing the saturation of the amplifier [57]. Moreover, thanks to the virtual short circuit between the inputs of the OPAMP [50,55,58], the parasitic capacitance of the QTF and the input capacitance of the OPAMP are grounded and do not contribute significantly to the output signal. If R_F is sufficiently high with

respect to the impedance of C_F at the operating frequency (for instance $R_F \cong 100 \text{ M}\Omega$), the gain of the CSA depends on the ratio between the QTF capacitance C_S and the external capacitor C_F [56,59]. Nevertheless, since C_F cannot be too low (otherwise it would be comparable to the parasitic capacitance of the board), this configuration does not allow high gain values.

Finally, in the transimpedance amplifier (Fig. 2.1c), the QTF piezo-current is converted to a voltage signal [60] by means of the feedback resistor R_F . The dashed capacitor C_F represents the stray capacitance associated to R_F ; if the impedance of this capacitance is not negligible with respect to R_F at the signal frequency, it creates a low-pass filter with a time constant $\tau_F = R_F \cdot C_F$, which remarkably attenuates the output signal [56,59]. This configuration allows to achieve higher gains with respect to the CSA configuration. For this reason, TIA is the most employed configuration for QTF readout [61-67].

The amplified signal is then fed to a lock-in amplifier, used for extracting a desired harmonic component of the input signal in an extremely noisy environment [68]. Figure 2.2 represents the scheme of a dual-phase lock-in amplifier, usually employed in QEPAS measurements.

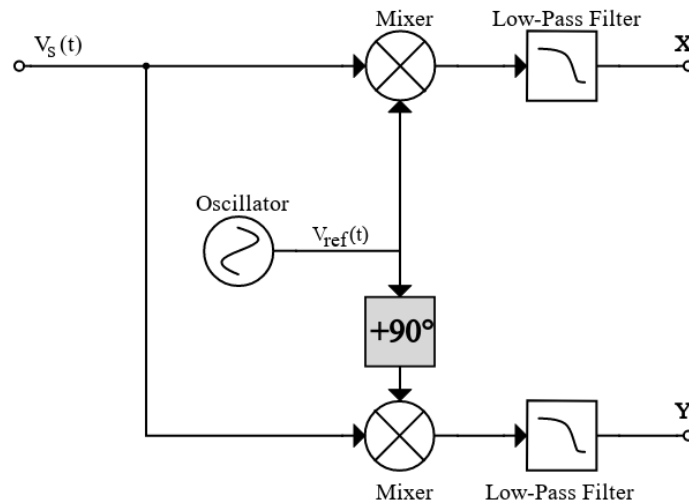


Figure 2.2 Sketch of a dual-phase lock-in amplifier. $V_s(t)$ is the input signal, $V_{ref}(t)$ is the reference signal provided by the oscillator. X and Y are the in-phase and out-of-phase output signal components, respectively.

The preamplifier output signal $V_s(t)$ is mixed with a reference signal $V_{ref}(t)$ generated by an oscillator (typically the TTL output of a waveform generator) and with its 90 degrees phase shifted version. Then a low-pass filter (LPF) preserves the DC components at the output of the mixers. Therefore, by choosing f_{ref} equal to the frequency of the signal f_s , the LPF output signal will depend on the amplitude of the input signal and on the phase shift ϕ between the input signal and the reference signal. On top of that, the output signal will be influenced only by the noise component around the reference frequency, thus getting rid of the noise floor overlapped to the input signal.

The X output of the LIA is referred to as in-phase component, since it reaches its maximum value when the phase shift ϕ is zero:

$$X \propto A_s \cdot \cos(\Phi) \quad (2.2)$$

where A_s is the amplitude of the input signal. The Y output signal is referred to as out-of-phase component:

$$Y \propto A_s \cdot \sin(\Phi) \quad (2.3)$$

Starting from these components, it is possible to retrieve the amplitude R of the output signal and the phase shift ϕ with the following expressions:

$$R = \sqrt{X^2 + Y^2} \propto A_s \quad (2.4)$$

$$\Phi = \arctg\left(\frac{Y}{X}\right) \quad (2.5)$$

2.2 Thevenin and Norton equivalent model of a QTF

Being the QTF a piezoelectric resonator, its mechanical parameters can be associated to corresponding electrical parameters. As already reported in section 1.2, the Butterworth – Van Dyke model can be efficiently employed to characterize the electrical behavior of a QTF. In addition, each amplifier configuration is characterized by its transfer function, which in turn depends on the parameters of the QTF. To separate the contributions of the QTF parameters from those of the preamplifier, as well as to simplify the overall transfer function at the output of the preamplifier, the

Butterworth – Van Dyke model will be replaced by its equivalent Thevenin model, according to the scheme shown in Fig. 2.3.

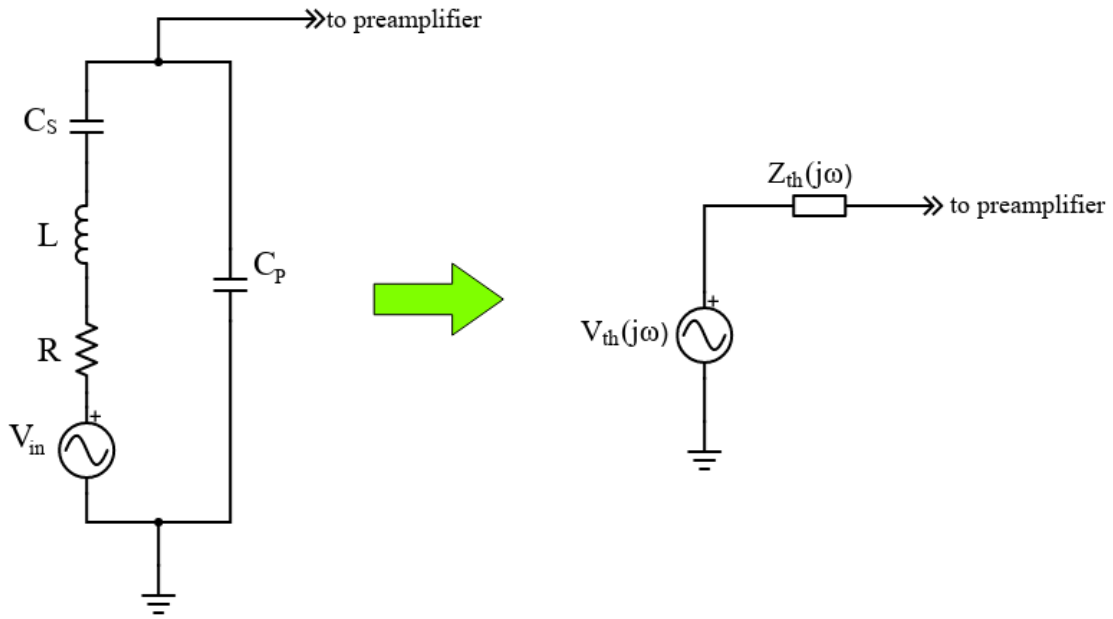


Figure 2.3 Thevenin equivalent model of a quartz tuning fork. V_{in} is the QTF internal signal generated by the piezoelectric effect, $V_{th}(j\omega)$ is the Thevenin equivalent voltage, and $Z_{th}(j\omega)$ is the Thevenin equivalent impedance.

With this model, the QTF is represented as the series connection between an equivalent voltage source and an equivalent impedance. $V_{th}(j\omega)$ is the voltage across the QTF pins when no load is applied to it, and can be easily computed as the division of V_{in} on the parasitic capacitance C_p :

$$V_{th}(j\omega) = \frac{1}{1 + \frac{C_p}{C_s}} \cdot \frac{V_{in}(j\omega)}{(1 - \omega^2 LC_{eq}) + j\omega RC_{eq}} \quad (2.6)$$

where $C_{eq} = C_p C_s / (C_p + C_s)$.

$Z_{th}(j\omega)$ is the equivalent impedance obtained shorting the signal source V_{in} corresponding to the impedance of the QTF:

$$\begin{aligned}
 Z_{th}(j\omega) &= Z_{QTF}(j\omega) \\
 &= \frac{1}{j\omega(C_P + C_S)} \cdot \frac{(1 - \omega^2 LC_S + j\omega RC_S)}{(1 - \omega^2 LC_{eq} + j\omega RC_{eq})}
 \end{aligned}
 \tag{2.7}$$

This schematization can be used to model the QTF when a voltage readout configuration is employed, as depicted in Fig. 2.4.

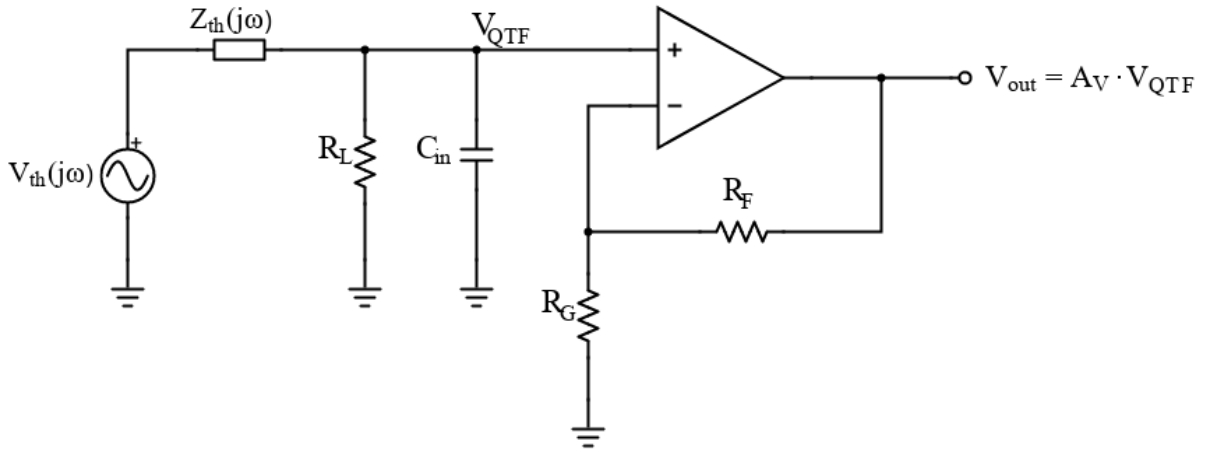


Figure 2.4 Equivalent circuit for the voltage mode readout of the QTF. C_{in} is the input capacitance of the operational amplifier.

The voltage on the non-inverting input of the OPAMP corresponds to the division of $V_{th}(j\omega)$ on the input impedance of the operational amplifier. The output voltage is then obtained by multiplying this voltage division by the voltage gain A_V of the amplifier (see Eq. 2.1).

When a current mode approach is used (i.e., a TIA or a CSA), it is convenient to model the QTF with the Norton equivalent model (see Fig. 2.5).

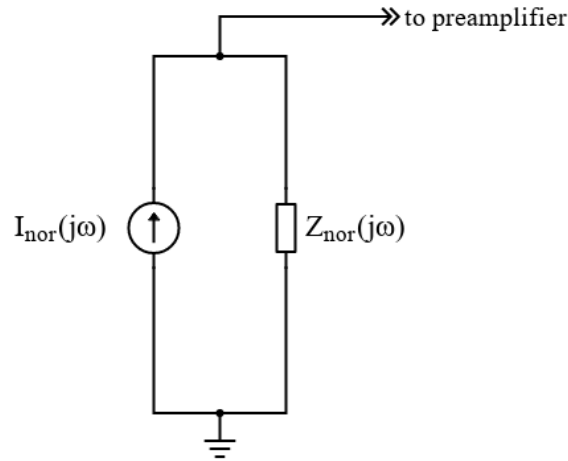


Figure 2.5 Norton equivalent model of the QTF. $I_{nor}(j\omega)$ is the Norton equivalent current and $Z_{nor}(j\omega)$ is the Norton equivalent impedance.

The QTF is represented as the parallel connection between an equivalent current source $I_{nor}(j\omega)$ and an equivalent impedance $Z_{nor}(j\omega)$. $I_{nor}(j\omega)$ is the current that flows between the QTF pins if they are shorted, and its expression can be easily derived by the Thevenin equivalent model:

$$I_{nor}(j\omega) = \frac{V_{th}(j\omega)}{Z_{th}(j\omega)} = V_{in} \cdot \frac{j\omega C_s}{(1 - \omega^2 LC_s) + j\omega RC_s} \quad (2.8)$$

The equivalent impedance $Z_{nor}(j\omega)$ is derived with the same procedure described in the Thevenin equivalent model, therefore it coincides with the impedance of the QTF $Z_{QTF}(j\omega)$.

If a transimpedance or charge sensitive amplifier is used for the QTF readout, the QTF can be easily represented with the Norton model, to retrieve the voltage of the output signal, as shown in Fig. 2.6.

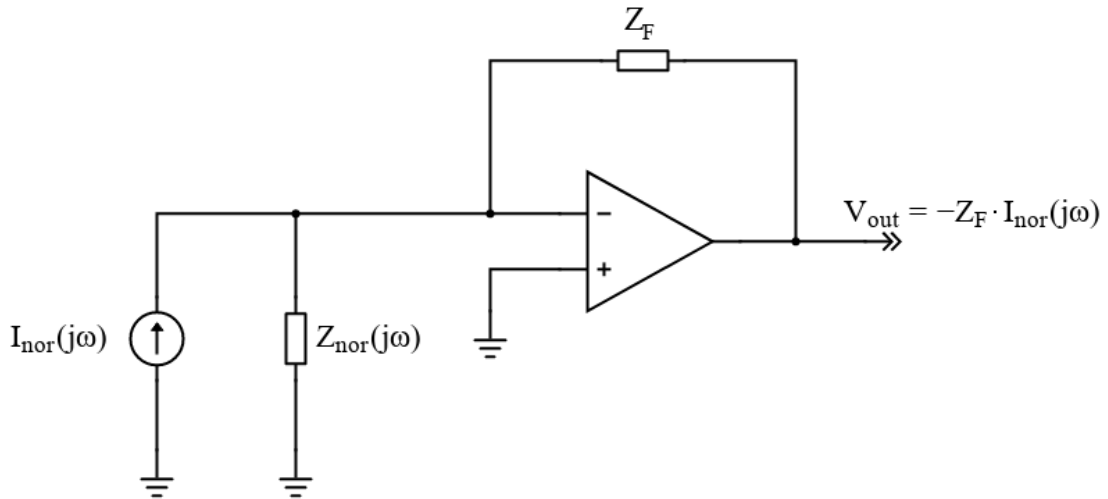


Figure 2.6 Equivalent circuit of a QTF current mode amplifier. Z_F is the impedance of the feedback network.

The impedance $Z_{nor}(j\omega)$ is grounded by the virtual short circuit imposed by the OPAMP. The virtual ground on the inverting input of the OPAMP does not influence the mechanical resonance of the QTF, as long as its fundamental mode is excited. As a consequence, assuming that the input bias current of the OPAMP is negligible, the output voltage can be easily calculated as the product between the feedback impedance Z_F and $I_{nor}(j\omega)$. This model can be applied for both TIA and CSA configuration; the only difference is that Z_F is a resistive impedance in the transimpedance amplifier, while it is a capacitive impedance in the charge sensitive amplifier.

2.3 Preamplifier configurations

The analog preamplifier represents the most critical stage in the signal conditioning chain of a QTF, since it influences the overall signal-to-noise ratio (SNR) and, in turn, the minimum detection limit of a QEPAS sensor [50]. For the calculation of the SNR, it is necessary to derive the signal transfer function and identify the main noise contributions in each configuration. Therefore, a theoretical analysis of the above-mentioned amplifier configurations is useful to underline advantages and drawbacks of each amplifier configuration, with the final target of choosing the best configuration to

be employed in a QEPAS sensor.

2.3.1 Voltage amplifier

As discussed in the previous section, the Butterworth–Van Dyke circuit and an equivalent Thevenin source were employed to model the QTF when excited by an acoustic wave [17] to find an analytical expression of the output signal V_{out} as a function of frequency for the circuit in Fig. 2.4. Straightforward calculations provide the expression of the transfer function $H_v(j\omega)$ between the internal voltage $V_{in}(j\omega)$ and the output voltage $V_{out}(j\omega)$:

$$H_v(j\omega) = \frac{V_{out}(j\omega)}{V_{in}(j\omega)} = A_v \cdot \frac{j\omega C_S R_L}{1 - \omega^2(LC_S + R_L R C_{pt} C_S) + j\omega[(R_L + R)C_S + R_L C_{pt} - \omega^2 L C_{pt} C_S R_L]} \quad (2.9)$$

where $C_{pt} = C_P + C_{in}$ is the total parasitic capacitance at the non-inverting input of the operational amplifier.

The squared modulus of $H_v(j\omega)$ describes the dependence of the squared amplitude of the circuit in the frequency domain:

$$|H_v(j\omega)|^2 = \frac{A_v^2}{\frac{\left(1 - \frac{\omega^2}{\omega_R^2}\right)^2}{\omega^2 R_L^2 C_S^2} + \left(1 + \frac{C_{pt}}{C_S}\right)^2 \left[\left(1 - \frac{\omega^2}{\omega_P^2}\right) + \frac{R}{R_L} \frac{C_S}{C_{pt} + C_S}\right]^2} \quad (2.10)$$

where $\omega_R = 1/\sqrt{LC_S + R_L R C_{pt} C_S}$ is the angular frequency corresponding to a pure real value for $H_v(j\omega)$ and $\omega_P = 1/\sqrt{LC_S C_{pt}/(C_S + C_{pt})} = 1/\sqrt{LC_{eq,tot}}$ is the parallel-resonant angular frequency of the QTF as loaded in the circuit shown in Fig. 2.4.

AC SPICE simulations (Simulation Program with Integrated Circuit Emphasis) were carried out to confirm the validity of the expression in Eq. 2.10. A SPICE simulator associates a coded model to each component of an electric circuit, and solves it by applying Kirchoff's current or voltage law. It assigns nodes to a circuit and

attempts to solve the current and voltage values at the respective nodes. The SPICE simulator first generates nodal equations in the matrix format before solving them to obtain the values [69], thus providing an accurate description of the circuit behavior. The set of typical parameters listed in Table 2.1 has been used for the QTF in both the analytical model and SPICE simulations. Moreover, in SPICE simulations, C_{in} is included in the model of the AD8067, provided by Analog Devices. AD8067 is a low-noise, high speed, FET input operational amplifier. Thanks to its very low input bias current, it is suitable for precision and high gain applications [70].

Parameter	Value
C_P	5 pF
C_S	5.2424 fF
L	4.5 kH
R	92.7 k Ω
C_{in}	1.5 pF
R_F	47 k Ω
R_G	1 k Ω

Table 2.1 Parameter values used to compare the results of expression in Eq. 2.10 to SPICE simulations.

The series-resonant frequency f_S of the QTF is:

$$f_S = \frac{\omega_S}{2\pi} = \frac{1}{2\pi\sqrt{LC_S}} = 32768 \text{ Hz} \quad (2.11)$$

whereas its quality factor Q is

$$Q = \frac{1}{\omega_S RC_S} = 10^4 \quad (2.12)$$

which are typical values for a standard 32.7 kHz-QTF used in a QEPAS sensor [14,17,18,71].

Moreover, the gain of the non-inverting configuration is $A_v = 48$ and the parallel-resonant frequency of the QTF is $f_P = \omega_P/2\pi = 32,781$ Hz. The value of $C_P \cong C_P +$

C_S could be found by measuring the equivalent capacitance of the QTF at low frequencies by mean of a capacitance meter. The ratio C_S/C_P is extracted by the ratio f_P/f_S after measuring the parallel and series-resonant frequencies of the QTF, where the circuit exhibits the minimum and maximum admittance, respectively. Finally, L can be calculated from f_S , knowing C_S , while R is extracted from the quality factor Q of the QTF [56]. Figure 2.7 shows the comparison between the results provided by the SPICE simulations and the analytical model for three different values of R_L (100 k Ω , 500 k Ω , and 2.5 M Ω).

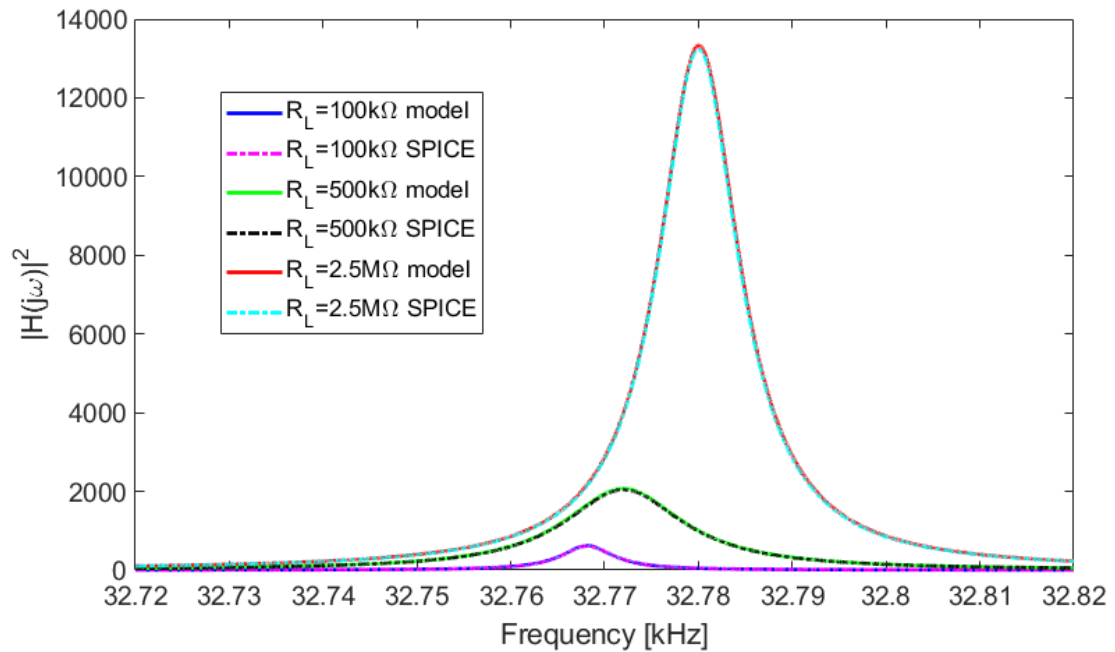


Figure 2.7 Comparison between SPICE simulations and analytical model in Eq. 2.10 of the frequency response of the circuit in Fig. 2.4 for $R_L = 100 \text{ k}\Omega$, $500 \text{ k}\Omega$ and $2.5 \text{ M}\Omega$.

The perfect matching between the two models demonstrates that Eq. 2.10 can be used to accurately represent the behavior of the circuit in Fig. 2.4. The maximum difference between the peak frequencies of corresponding curves is in the order of a few hundredths of Hz and the mean absolute percentage error between corresponding curves is about 1.8%.

As shown in Fig. 2.7, the output signal amplitude and the peak frequency f_{peak}

strongly depend on the value of the resistor R_L . This is particularly relevant for an optimal choice of the operating frequency in the QEPAS technique, aimed at exploiting as much as possible the resonance properties of the QTF. Figure 2.8 shows the f_{peak} trend as a function of R_L . This curve was retrieved computing $|H_v(j\omega)|^2$ for different values of R_L and then applying MATLAB code to retrieve f_{peak} values.

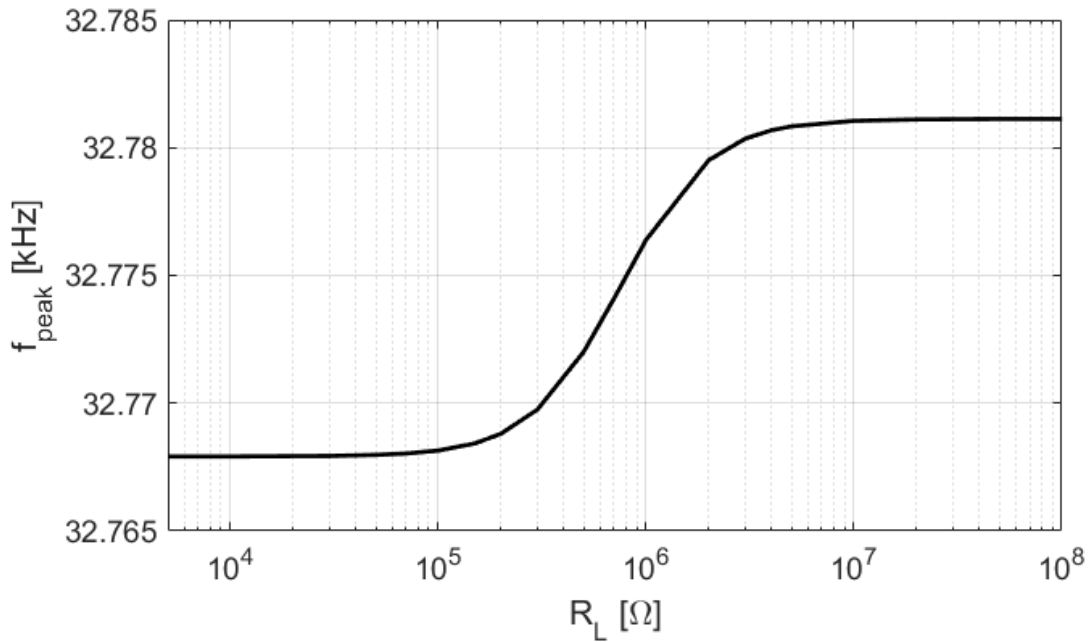


Figure 2.8 Peak frequency f_{peak} of $|H_v|^2$ as a function of R_L .

For R_L values lower than 100 k Ω , f_{peak} tends to the series-resonant frequency $f_S = 32768$ Hz; whereas, for R_L values higher than 2 M Ω , f_{peak} tends to the parallel-resonant frequency $f_P = 32781$ Hz.

The behavior of the peak position as a function of R_L value can be explained considering the two terms which compose the denominator of the function $|H_v(j\omega)|^2$ in Eq. 2.10, reported here for ease of reading as $Den1$ and $Den2$:

$$Den1(\omega) = \frac{\left(1 - \frac{\omega^2}{\omega_R^2}\right)^2}{\omega^2 R_L^2 C_S^2}, \quad Den2(\omega) = \left(1 + \frac{C_{pt}}{C_S}\right)^2 \left[\left(1 - \frac{\omega^2}{\omega_P^2}\right) + \frac{R}{R_L} \cdot \frac{C_S}{C_{pt} + C_S} \right]^2 \quad (2.13)$$

The behavior of $Den1(\omega)$ and $Den2(\omega)$ as a function of frequency is reported in Fig. 2.9a and 2.9b for $R_L = 100 \text{ k}\Omega$ and $R_L = 10 \text{ M}\Omega$, respectively.

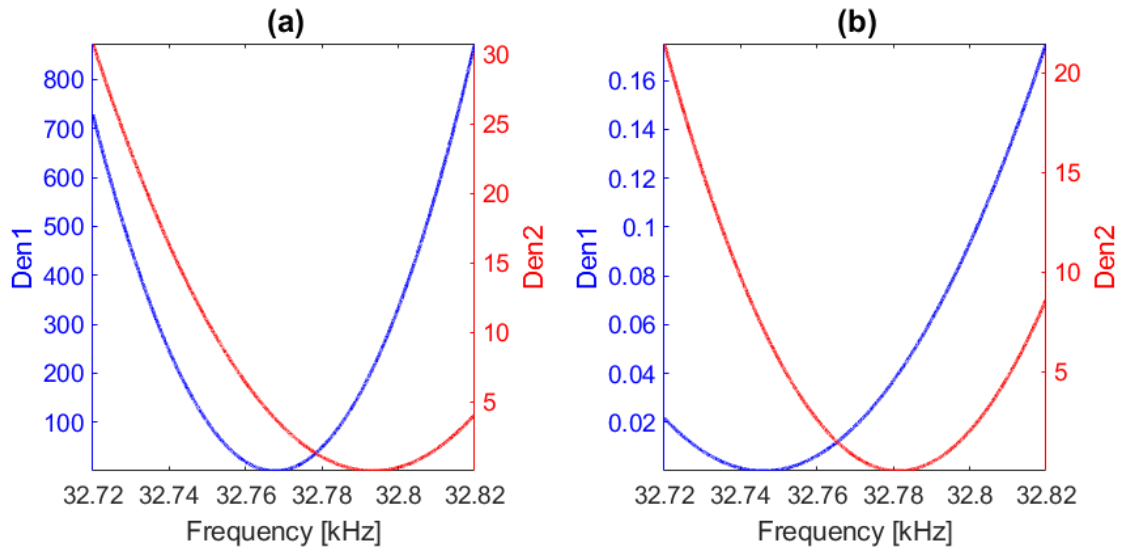


Figure 2.9 Behavior of $Den1(f)$ and $Den2(f)$ in Eq. 2.13 as a function of frequency for (a) $R_L = 100 \text{ k}\Omega$ and (b) $R_L = 10 \text{ M}\Omega$.

Results show that $Den1(\omega)$ is strongly dependent on the value of R_L . In the investigated frequency range:

- (i) the maximum value of $Den1(\omega)$ varies from 868.3 (Fig. 2.9a) to 0.17 (Fig. 2.9b)
- (ii) the blue curve at $100 \text{ k}\Omega$ varies more rapidly than the $Den1(\omega)$ curve at $10 \text{ M}\Omega$ in the frequency range close to the minimum
- (iii) the frequency where the $Den1(\omega)$ minimum occurs decreases by more than 20 Hz, from 32,768 Hz (Fig. 2.9a) to 32,746 Hz (Fig. 2.9b).

Conversely, the dependence of $Den2(\omega)$ on R_L is only due to the term $\frac{R}{R_L} \frac{C_S}{C_{pt} + C_S}$, which is negligible when $R_L \geq 1\text{M}\Omega$, since $C_S \ll C_{pt}$ and $R_P \ll R_L$.

In addition:

- (i) the red curve maximum value varies from 30.8 (Fig. 2.9a) to 21.5 (Fig. 2.9b)
- (ii) Variations of $Den2(\omega)$ values in the frequency range close to the minimum value are slightly different at 100 k Ω and at 10 M Ω
- (iii) the difference frequency where the $Den2(\omega)$ minimum occurs is about 13 Hz, from 32,794 Hz (Fig. 2.9a) to 32,781 Hz (Fig. 2.9b).

As a result, for $R_L < 100\text{ k}\Omega$, the contribution of $Den1(\omega)$ becomes dominant, so that when R_L decreases, the minimum value of the denominator of $|H_v(j\omega)|^2$ tends to the zero of $Den1(\omega)$ function, located at $\omega = \omega_R$. Moreover, in this range of R_L values, ω_R could be approximated to ω_S :

$$\omega_R = \frac{1}{\sqrt{LC_S + R_L RC_{pt} C_S}} \cong \frac{1}{\sqrt{LC_S}} = \omega_S \quad (2.14)$$

and the peak of $|H_v(j\omega)|^2$ tends to the series-resonant frequency of the QTF. Instead, for $R_L > 2\text{ M}\Omega$, $Den1(\omega)$ becomes less relevant and $Den2(\omega)$ tends to be dominant in the sum of the two terms. Therefore, the minimum of the sum tends to the zero of $Den2(\omega)$. Finally, for the values of R_L , this zero is very close to $\omega = \omega_P$, thus, the peak of $|H_v(j\omega)|^2$ is almost coincident with the parallel-resonant frequency of the QTF.

The trend of the peak value of $|H_v(j\omega)|^2$ as a function of R_L value is shown in Fig. 2.10. The same method applied for Fig. 2.8 was used to obtain this curve.

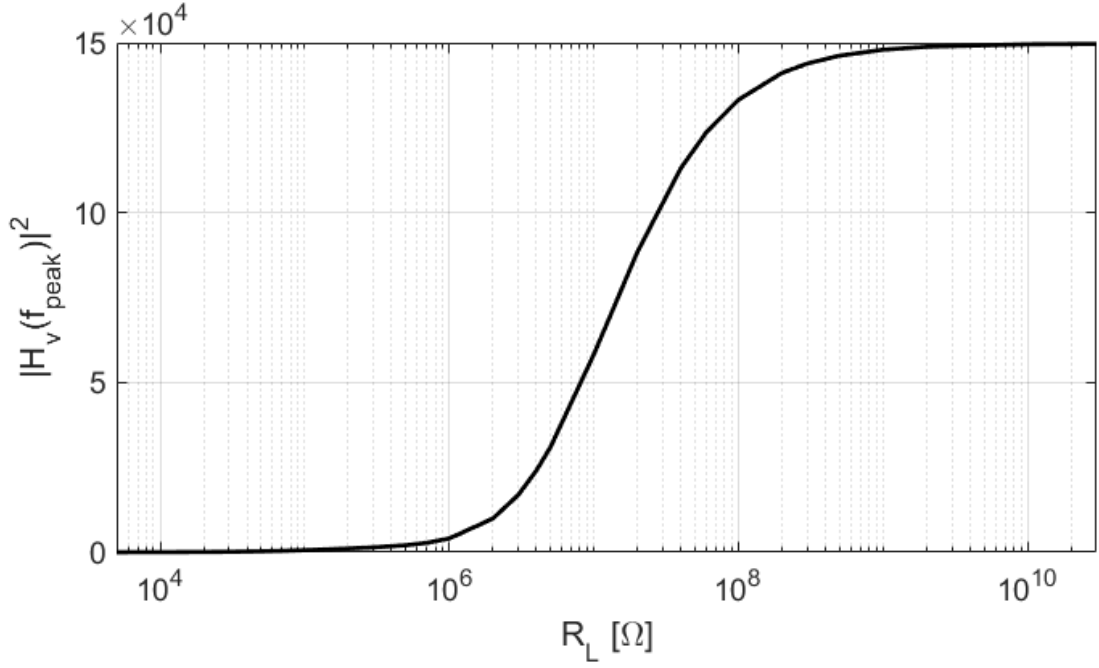


Figure 2.10 Peak value of $|H_v|^2$ as a function of R_L .

The peak value of $|H_v(j\omega)|^2$ is an increasing function of R_L up to a saturation value at $R_L > 1 \text{ G}\Omega$. As discussed in the previous section, for large values of R_L , $\omega_{peak} = 2\pi f_{peak}$ is very close to the parallel-resonant angular frequency ω_P and the peak of $|H_v(j\omega)|^2$ tends to the following value:

$$|H_v(j\omega_{peak})|^2 \cong |H_v(j\omega_P)|^2 \cong A_v^2 \cdot \frac{\omega_P^2 R_L^2 C_S^2}{\left(1 - \frac{\omega_P^2}{\omega_R^2}\right)^2} \quad (2.15)$$

The denominator of Eq. 2.15 can be rewritten as:

$$\begin{aligned} 1 - \frac{\omega_P^2}{\omega_R^2} &= 1 - \frac{LC_S + R_L RC_{pt} C_S}{LC_{eq,tot}} \\ &= \frac{L(C_{eq,tot} - C_S) - R_L RC_{pt} C_S}{LC_{eq,tot}} \\ &\cong -\frac{R_L RC_{pt}}{L} \end{aligned} \quad (2.16)$$

Since $C_{eq,tot} \cong C_S$ and R_L is very large, it results:

$$|H_v(j\omega_{peak})|^2 \cong A_v^2 \frac{\frac{1}{LC_{eq,tot}} R_L^2 C_S^2}{\frac{R_L^2 R^2 C_{pt}^2}{L^2}} \cong A_v^2 \frac{LC_S}{R^2 C_{pt}^2} \quad (2.17)$$

which is independent on R_L .

However, the performance of the QEPAS technique will depend on the SNR obtained at the output of the preamplifier, not only on the amplitude of the signal. Therefore, for maximizing the SNR, it is mandatory to carry out a detailed study of the electronic noise contributions that are involved in the circuit.

The most relevant contributions to the total electronic noise at the output of the voltage-mode preamplifier are shown in Fig. 2.11.

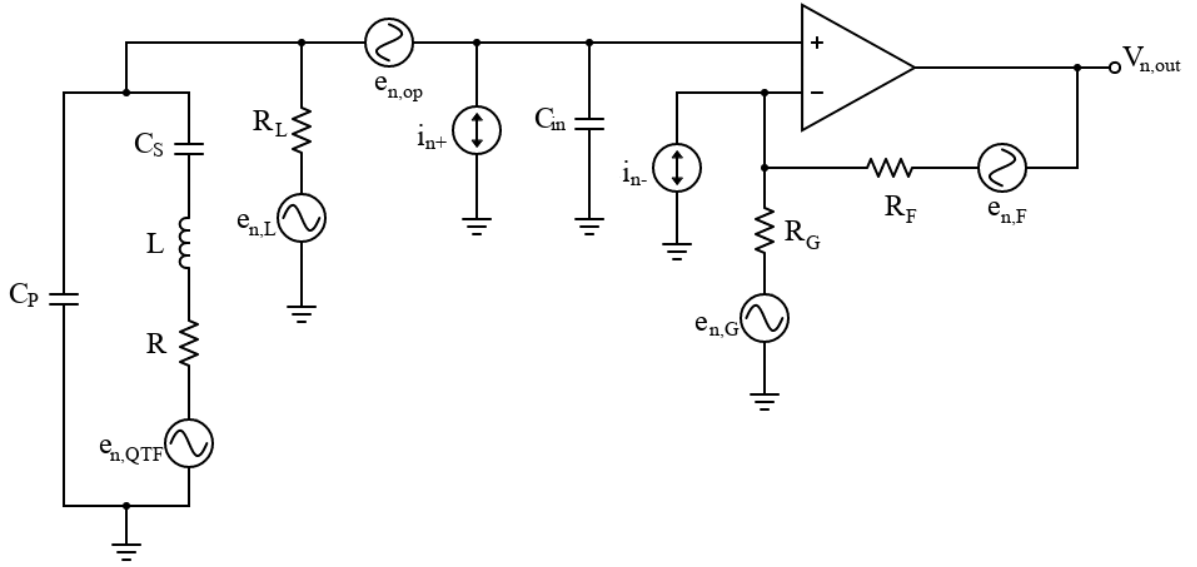


Figure 2.11 Noise contributions in the circuit of Fig. 2.4.

In the following calculation, the phase noise was neglected [72] and only the main electronic noise contributions were considered. Each resistor R_i of the circuit was associated to its thermal noise voltage source, $e_{n,i}^2 = 4kTR_i$. The OPAMP noise was characterized by means of the classic equivalent input noise voltage ($e_{n,op}$) and current (i_{n+} and i_{n-}) sources. To simplify the study without losing accuracy, it is possible to neglect the noise contributions of R_F and R_G , composing the feedback network, due to the small values of these resistors. For the same reasons, the equivalent noise current i_{n-} .

associated to the inverting input of the OPAMP likewise does not give any relevant contribution. Moreover, all the sources in Fig. 2.11 can be considered independent, so that the total output noise power spectral density $S_{n_{tot}}(\omega)$ can be evaluated as follows:

$$S_{n_{tot}}(\omega) \cong S_{n_{QTF}}(\omega) + S_{n_L}(\omega) + S_{n_{op}}(\omega) + S_{n_{i_{n+}}}(\omega) \quad (2.18)$$

where the terms of the right-hand side come from R , R_L , $e_{n_{op}}$, and i_{n+} , respectively. In Eq. 2.18, the single terms are the product of the spectral density of each noise source multiplied by the squared modulus of the transfer function between the noise source and the output of the circuit, determined using the superposition principle [73].

Concerning the noise associated to the resistor R , the transfer function $S_{n_{QTF}}(\omega)$ between the source $e_{n_{QTF}}$ and the output of the preamplifier is $H_v(j\omega)$, thus:

$$S_{n_{QTF}}(\omega) = 4kTR \cdot |H_v(j\omega)|^2 \quad (2.19)$$

As a consequence, the behavior of $S_{n_{QTF}}(\omega)$ as a function of both the frequency and R_L is the same discussed previously.

Let us now consider the noise contribution from the resistor R_L . The transfer function between the source e_{n_L} and the output of the front-end is:

$$\begin{aligned} H_L(j\omega) &= \frac{V_{n.out}(j\omega)}{e_{n_L}(j\omega)} \\ &= A_v \frac{1 - \omega^2 LC_S + j\omega RC_S}{1 - \frac{\omega^2}{\omega_R^2} + j\omega[(R_L + R)C_S + R_L C_{pt} - \omega^2 LC_{pt} C_S R_L]} \end{aligned} \quad (2.20)$$

The denominators of $H_v(j\omega)$ and $H_L(j\omega)$ are the same and the two transfer functions differ only in their numerator. The contribution of the thermal noise of the resistor R_L to the total output noise spectral density is:

$$S_{n_L}(\omega) = 4kTR_L |H_L(j\omega)|^2 \quad (2.21)$$

Figure 2.12 shows the behavior of S_{n_L} as a function of the frequency, for four different values of R_L (100 k Ω , 500 k Ω , 6 M Ω , and 20 M Ω).

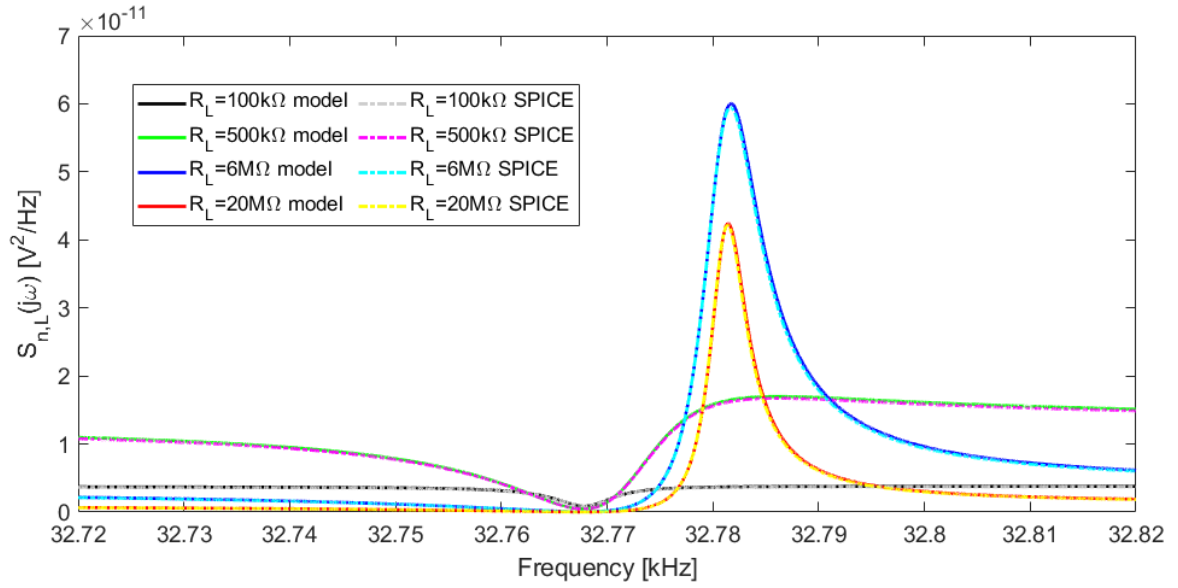


Figure 2.12 Comparison between SPICE simulations and analytical model described in Eq. 2.21 of the output noise spectral density contribution from the thermal noise of R_L , for four different values of the resistor: 100 k Ω , 500 k Ω , 6 M Ω , and 20 M Ω .

The curves calculated with Eq. 2.21 and those obtained by SPICE simulation are in excellent agreement. The function $|H_L(j\omega)|$ has a minimum located at $\omega = \omega_S$, since, at the series-resonant frequency, the Butterworth–Van Dyke impedance model of the QTF is reduced to R , which is the minimum value. Accordingly, also $S_{n,L}(\omega)$ exhibits a minimum at the same frequency value. Furthermore, a peak appears around the parallel-resonant frequency for increasing values of R_L . Figure 2.13 reports the behavior of the peak value of $S_{n,L}(\omega)$ as a function of R_L varying from 500 k Ω to 20 M Ω .

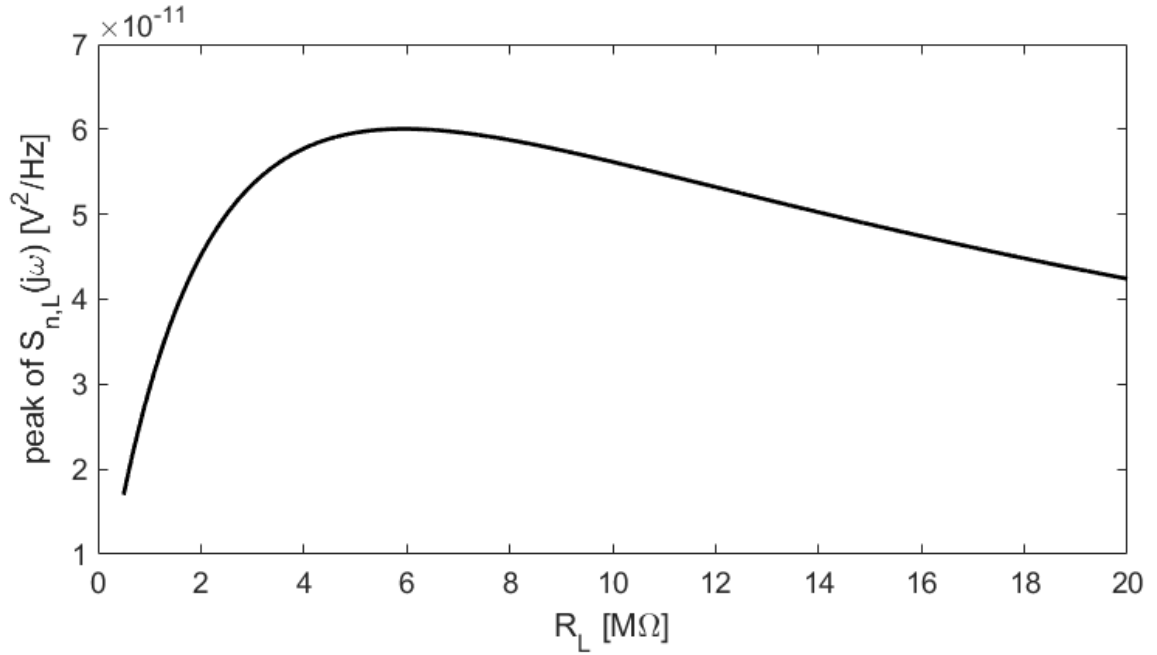


Figure 2.13 Peak of the output noise spectral density contribution due to R_L as a function of R_L itself.

Using the set of parameters listed in Tab. 2.1, starting from low values of R_L , the peak appears at $R_L = 500$ kΩ (dashed magenta and green curves in Fig. 2.12), then increases up to $R_L = 6$ MΩ (Fig. 2.13). Beyond this value, the peak decreases for increasing values of R_L and the function $S_{n,L}(\omega)$ assumes lower values in the frequency range under investigation.

For what concerns the noise contributions considered up to now, Figures 2.10 and 2.13 suggest that it is convenient to work with large values of the resistor R_L because the amplitude of the output signal increases with R_L (see Fig. 2.10) and the noise contribution due to this resistor decreases (see Fig. 2.13), whereas the contribution from the thermal noise of R has exactly the same frequency behavior of the signal. Let us now consider the contribution of the input equivalent voltage noise of the OPAMP to the total output noise, namely:

$$S_{n,op}(\omega) = e_{n,op}^2 \cdot |H_{en}(j\omega)|^2 \quad (2.22)$$

Since the flicker noise was considered negligible in the narrow bandwidth of interest, namely, around the QTF resonance frequency, the input equivalent noise

voltage has a constant power spectral density, i.e., it can be considered as a white noise. The value of $e_{n,op}$ has been set at 6.6 nV/ $\sqrt{\text{Hz}}$, as reported in the data sheet of the AD8067 [70]. The transfer function $H_{en}(j\omega)$ can be expressed as follows:

$$H_{en}(j\omega) = \frac{V_{n,out}(j\omega)}{e_{n,op}(j\omega)} \quad (2.23)$$

$$= A_v \frac{1 - \omega^2(LC_S + R_L R C_P C_S) + j\omega[(R + R_L)C_S + R_L C_P - \omega^2 L C_P C_S R_L]}{1 - \omega^2(LC_S + R_L R C_{pt} C_S) + j\omega[(R + R_L)C_S + R_L C_{pt} - \omega^2 L C_{pt} C_S R_L]}$$

in which the numerator differs from the denominator only for the capacitance $C_{pt} = C_P + C_{in}$ replaced by C_P . This contribution can be considered as constant in the frequency range investigated for QEPAS applications.

The contribution of the input equivalent current noise i_{n+} to the overall output noise spectral density $S_{n,tot}(\omega)$ is

$$S_{n,i_{n+}}(\omega) = i_{n+}^2(\omega) R_L^2 |H_L(j\omega)|^2 \quad (2.24)$$

Using Eq.s 2.24 and 2.21, the contributions to $S_{n,tot}(\omega)$, due to i_{n+} and R_L , respectively, can be compared as:

$$\frac{S_{n,i_{n+}}(\omega)}{S_{n,L}(\omega)} = \frac{i_{n+}^2(\omega) R_L}{4kT} \quad (2.25)$$

The contribution of $S_{in+}(\omega)$ can be neglected with respect to $S_{n,L}(\omega)$ when

$$i_{n+}^2(\omega) \ll \frac{4kT}{R_L} \quad (2.26)$$

For a large R_L value, i.e., 100M Ω , $S_{in+}(\omega)$ will be negligible at room temperature when $i_{n+} \ll 13$ fA/ $\sqrt{\text{Hz}}$. Since the AD8067 has FET inputs, $i_{n+}(\omega)$ cannot be considered white, but is a linear function of the frequency, in the range where the flicker noise can be neglected [75]. In our model, the value of $i_{n+}(\omega)$ at 10 kHz was set to 1 fA/ $\sqrt{\text{Hz}}$, a slightly higher value than the one reported in the datasheet of the OPAMP, which is 0.6 fA/ $\sqrt{\text{Hz}}$ [70], and the slope of the linear function was set to +20 dB/dec [75]. Figure 2.14 shows the excellent correspondence between the analytical model used for $i_{n+}(\omega)$ and the input equivalent noise current resulting from a simulation carried out with the

SPICE model of the AD8067.

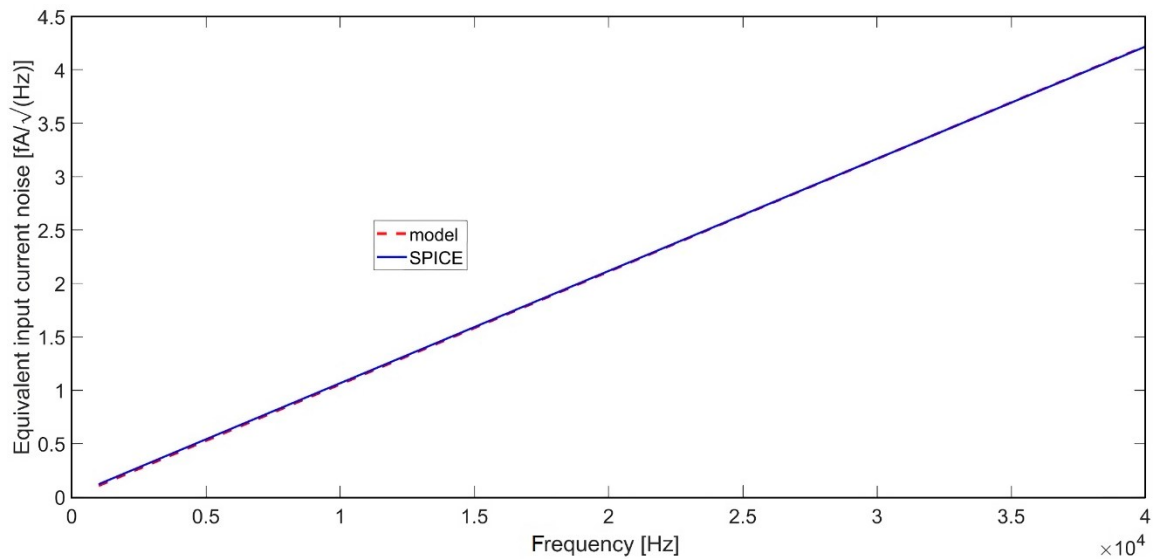


Figure 2.14 Fitting between the analytical model and SPICE simulations of the input equivalent noise current of the AD8067.

It is worth noticing that around the resonance frequencies of the QTF, the level of $i_{n+}(\omega)$ remains lower than the limit of $13 \text{ fA}/\sqrt{\text{Hz}}$ determined above. Thus, the contribution $S_{in+}(\omega)$ is negligible with respect to $S_{n,L}(\omega)$ in the noise analysis of the circuit without losing accuracy.

The analysis carried out so far allows for a comparison of the terms in Eq. 2.18 to understand which ones are dominant for the output noise spectral density of the preamplifier. Figure 2.15 compares the spectral contributions of the OPAMP and the resistors R and R_L to the overall $S_{n,tot}(\omega)$ at the output of the circuit. The terms due to $e_{n,op}$ and i_{n+} , namely, $S_{n,op}(\omega)$ and $S_{n,in+}(\omega)$, respectively, are summed, for retrieving the overall noise contribution of the OPAMP ($S_{opamp}(\omega)$) and allowing for a comparison of the analytical model with the results of SPICE simulations, in which the two terms are not distinguishable. The same R_L values of Fig. 2.10 were considered ($100 \text{ k}\Omega$, $500 \text{ k}\Omega$, $6 \text{ M}\Omega$, and $20 \text{ M}\Omega$).

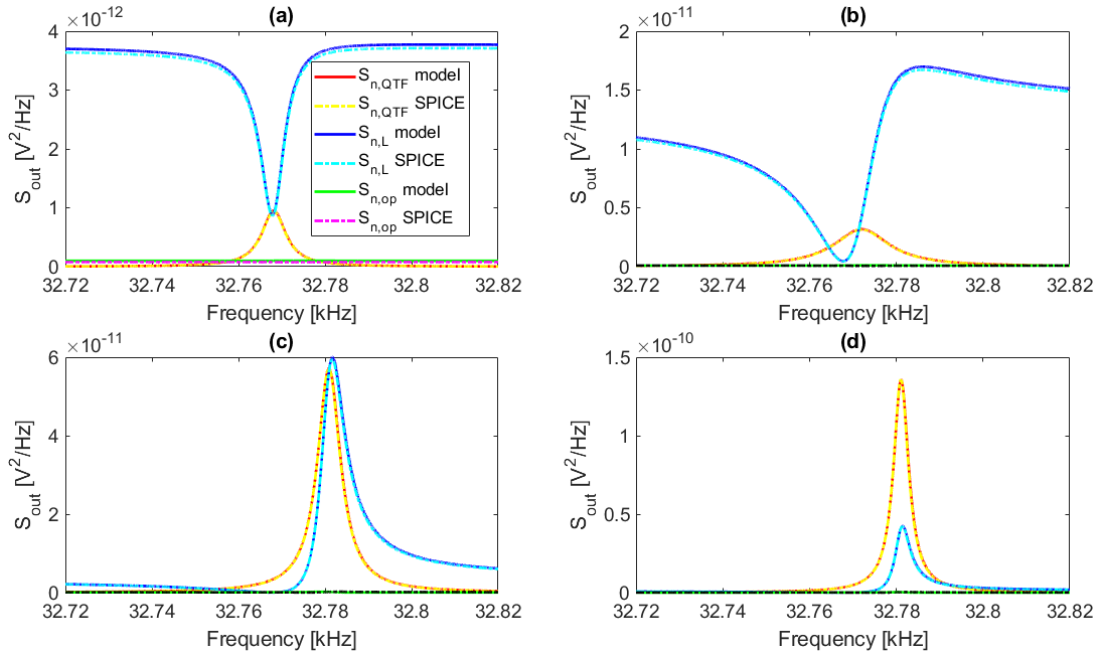


Figure 2.15 Contributions to the overall output noise spectral density due to the OPAMP and resistors R and R_L , for (a) $R_L = 100 \text{ k}\Omega$, (b) $R_L = 500 \text{ k}\Omega$, (c) $R_L = 6 \text{ M}\Omega$, (d) $R_L = 20 \text{ M}\Omega$: comparison between the results obtained with the analytical model and SPICE simulations.

For all the considered cases, the results provided by the analytical model and the SPICE simulations exhibit a very good agreement. In addition, the contribution of the OPAMP to the total output noise is always negligible compared to the sum of the contributions from R_L and R . $S_{n,L}(\omega)$ tends to overcome $S_{n,p}(\omega)$ for $R_L < 6 \text{ M}\Omega$ (Fig. 2.15a,b), whereas the opposite trend is observed when the value of R_L is larger than $6 \text{ M}\Omega$ (Fig. 2.15c,d). This confirms the previous conclusion about the advantage of working with large values of the resistor R_L in order to achieve good performance in terms of SNR.

2.3.2 Transimpedance amplifier

The QTF model described in section 2.2, together with the parameters listed in Tab. 2.1, was employed to retrieve an analytical expression of the signal output voltage in a transimpedance amplifier, as a function of the frequency. Figure 2.16 shows the

equivalent schematic circuit of a Transimpedance Amplifier (TIA).

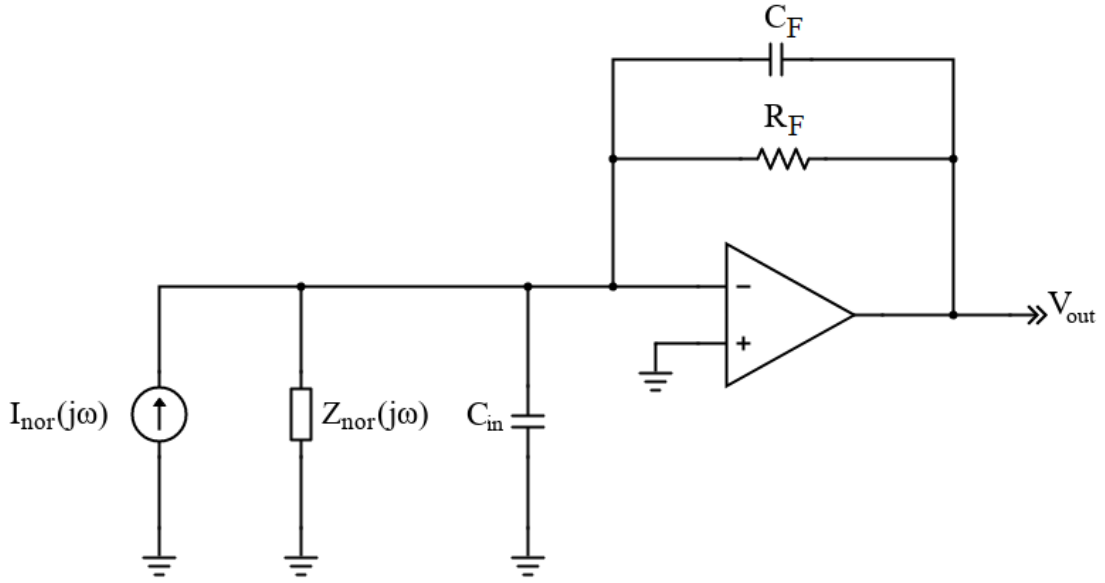


Figure 2.16 Equivalent circuit diagram of a transimpedance amplifier. $I_{nor}(j\omega)$ is the equivalent Norton current (see eq. 2.8), $Z_{nor}(j\omega)$ is the equivalent Norton impedance and coincides with the QTF impedance.

The total input capacitance C_{in} is 4 pF, corresponding to the sum of the differential input capacitance and common-mode input capacitance of the AD8067 OPAMP [70]. C_F is the stray capacitance in parallel to the R_F , due to feedback resistor parasitic and to the interconnections of the electronic components on the printed circuit board. As already mentioned, $I_{nor}(j\omega)$ is forced to flow in the feedback network, hence the squared module of the signal transfer function can be expressed as follows:

$$|H_{TIA}(j\omega)|^2 = \frac{\omega^2 C_S^2}{\left(1 - \frac{\omega^2}{\omega_S^2}\right)^2 + \omega^2 R^2 C_S^2} \cdot \frac{R_F^2}{1 + \omega^2 \tau_F^2} \quad (2.27)$$

where $\tau_F = R_F \cdot C_F$ is the time constant of the feedback network.

Figure 2.17 shows the comparison between the results obtained with the analytical model and SPICE simulations for three different values of R_F (1 M Ω , 5 M Ω and 10 M Ω).

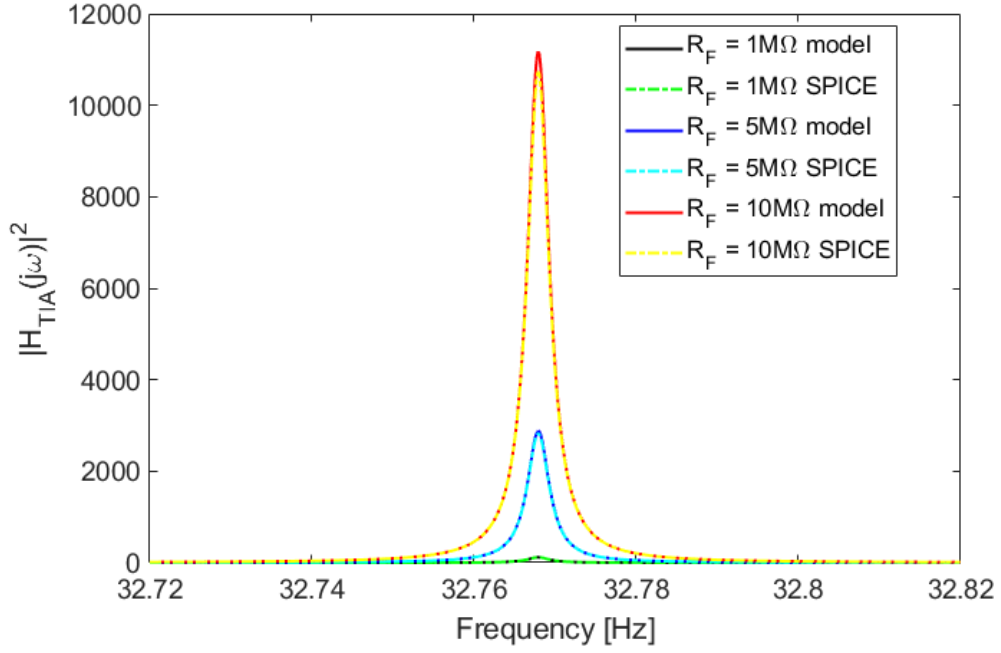


Figure 2.17 Comparison between analytical model and SPICE simulations of the signal transfer function, for $R_F = 1 \text{ M}\Omega$, $5 \text{ M}\Omega$ and $10 \text{ M}\Omega$. A stray capacitance C_F of 100 fF was considered.

The peak value of $|H_{TIA}(j\omega)|^2$ always occurs at the series-resonant angular frequency ω_S , regardless of the value of R_F . If the impedance associated to C_F is negligible with respect to R_F , the transfer function in correspondence of the series resonance frequency is given by:

$$|H_{TIA}(j\omega_S)|^2 = \frac{R_F^2}{R^2} \quad (2.28)$$

In addition, the curves obtained with the analytical model are in good agreement with the outcome of SPICE simulations. Therefore, Eq. 2.27 can be efficiently used to characterize the frequency response of the circuit in Fig. 2.16.

Nevertheless, it is worth noticing that the peak value of $|H_{TIA}(j\omega)|$ is influenced by the parasitic capacitance C_F , as can be deduced from Fig. 2.18.

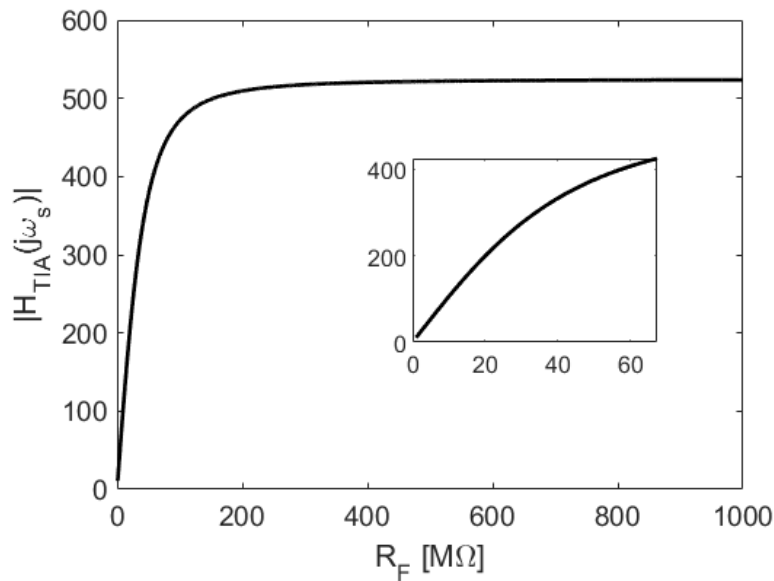


Fig. 2.18 Module of the TIA transfer function at the series-resonant frequency as a function of the feedback resistor R_F .

When $R_F < 20 \text{ M}\Omega$, $|H_{TIA}(j\omega_s)|$ tends to increase linearly with R_F , as the impedance of the feedback capacitance is much higher than R_F . For values of R_F higher than $20 \text{ M}\Omega$, the peak value of the transfer function module starts to deviate from the linear trend; for $R_F > 200 \text{ M}\Omega$ the peak saturates to a constant value. Therefore, the most important guideline for designing the layout of the amplifier board is to minimize the stray capacitance and preserve the gain of the transimpedance stage.

Noise analysis can be performed following the same procedure described in the previous section. The equivalent circuit for the calculation of the output spectral noise density is shown in Fig. 2.19.

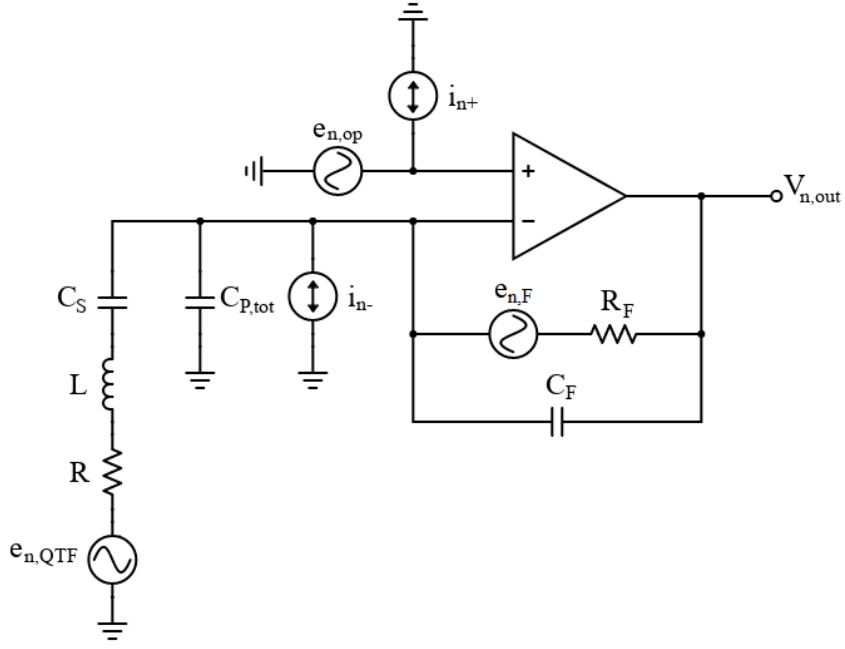


Figure 2.19 Equivalent circuit for the calculation of the output noise spectral density in a transimpedance amplifier. $C_{P,tot}$ is the sum of the parasitic capacitance of the QTF C_P and the input parasitic capacitance of the OPAMP C_{in} .

In a transimpedance amplifier, the equivalent noise current at the non-inverting input flows to the ground, hence i_{n+} does not provide any meaningful contribution to the total output noise.

As already observed, the transfer function associated to the noise contribution of R is identical to the signal transfer function, hence:

$$S_{n,QTF}(\omega) = 4kTR \cdot |H_{TIA}(j\omega)|^2 \quad (2.29)$$

Considering Eq. 2.28, Eq. 2.29 can be rewritten as follows:

$$S_{n,QTF}(\omega_S) = 4kT \frac{R_F^2}{R} \quad (2.30)$$

The transfer function associated to the voltage noise of the OPAMP is:

$$|H_{e_n}(j\omega)|^2 = \frac{(1 - \omega^2(LC_S + R_F R C_S (C_{P2} + C_F)))^2 + \omega^2(RC_S + R_F(C_S + C_{P2} + C_F) - \omega^2 L R_F C_S (C_{P2} + C_F))^2}{(1 - \omega^2(LC_S + R_F R C_S C_F))^2 + \omega^2(RC_S + R_F C_F - \omega^2 L R_F C_S C_F)^2} \quad (2.31)$$

where C_{P2} is the sum between C_P and the common mode input capacitance C_{CM} . This function peaks in correspondence of $\omega_{e_n,peak} = 1/\sqrt{LC_S + R_F RC_S C_F}$, which coincides with ω_S if τ_F is much shorter than the QTF time constant. In addition, if $R_F \ll 1/\omega C_F$:

$$\begin{aligned} S_{n,op}(\omega_S) &= e_n^2 \left[\left(1 + \frac{R_F}{R}\right)^2 + \omega_S^2 R_F^2 C_{P2}^2 \right] \\ &\cong e_n^2 \left(1 + \frac{R_F}{R}\right)^2 \end{aligned} \quad (2.32)$$

Therefore, at the series resonant frequency, the output noise spectral density associated to the voltage noise of the OPAMP is proportional to the squared value of the feedback resistance.

The contribution from the equivalent noise current at the inverting input of the OPAMP can be computed as follows:

$$S_{n,i_{n-}}(\omega) = i_{n-}^2 \cdot \frac{R_F^2}{1 + \omega^2 R_F^2 C_F^2} \cong i_{n-}^2 R_F^2 \quad (2.33)$$

Finally, the R_F noise contribution is:

$$S_{n,R_F}(\omega) = 4kTR_F \cdot \frac{1}{1 + \omega^2 R_F^2 C_F^2} \cong 4kTR_F \quad (2.34)$$

It is worth noticing that the noise contributions from i_{n-} and R_F do not depend on frequency, hence they can be considered as white noise sources. Figure 2.20 depicts the main noise contributions at the output of the transimpedance amplifier as a function of the frequency.

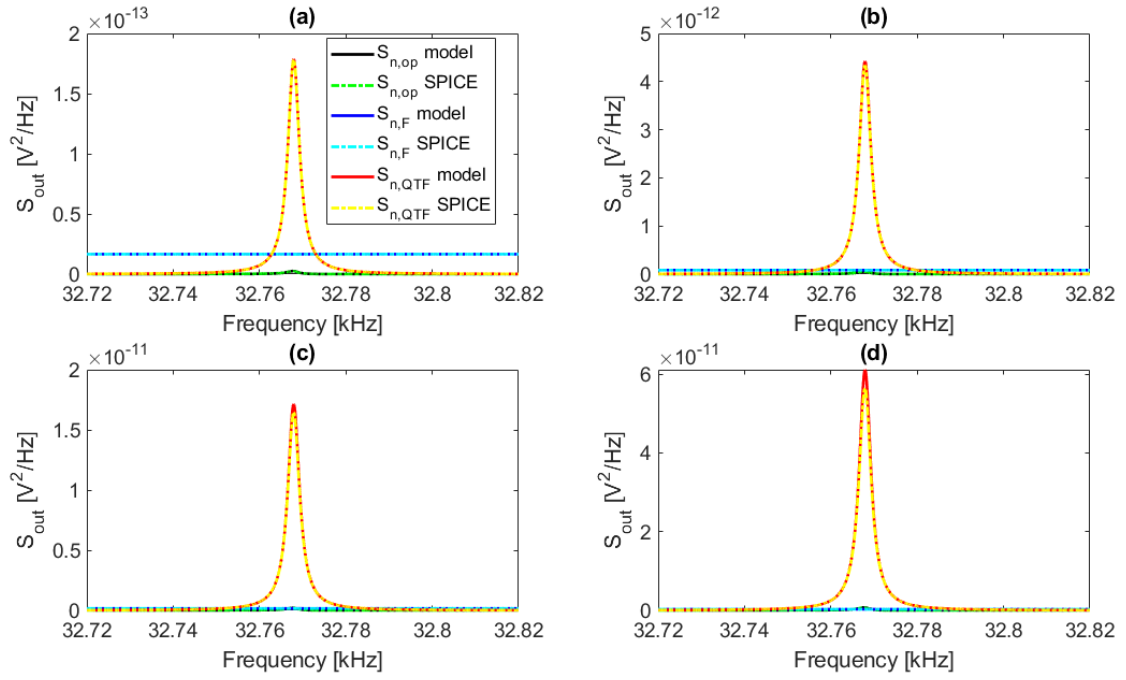


Figure 2.20 Contributions to the overall output noise spectral density due to the OPAMP and resistors R_F and R , for (a) $R_F = 1 \text{ M}\Omega$, (b) $R_F = 5 \text{ M}\Omega$, (c) $R_F = 10 \text{ M}\Omega$, (d) $R_F = 20 \text{ M}\Omega$: comparison between the results obtained with the analytical model and SPICE simulations.

The figure shows a good matching between the analytical model and data obtained by SPICE simulations. Moreover, the noise contribution associated to the intrinsic resistance of the QTF is the dominant one, while R_F and OPAMP noise contributions are negligible for increasing values of the feedback resistance. In particular, the SNR normalized to a 1 Hz integration bandwidth, associated to the noise contribution of R_F only at the series-resonant frequency, is:

$$SNR_{R_F}(\omega_S) = \frac{\frac{R_F^2}{R^2}}{4kTR_F} = \frac{1}{4kT} \frac{R_F}{R^2} \quad (2.35)$$

which is an increasing function of R_F . Hence, even though $S_{n,F}$ increases along with the feedback resistance, it can be neglected for $R_F > 5 \text{ M}\Omega$, without losing reliability.

The normalized SNR associated to the OPAMP voltage noise is:

$$\begin{aligned}
 SNR_{op}(\omega_S) &= \frac{\frac{R_F^2}{R^2}}{e_n^2 \left(1 + \frac{R_F}{R}\right)^2} \\
 &\cong \frac{\frac{R_F^2}{R^2}}{e_n^2 \cdot \frac{R_F^2}{R^2}} = \frac{1}{e_n^2}
 \end{aligned}
 \tag{2.36}$$

This contribution depends only on the input noise spectral density of the operational amplifier and can be optimized by working with a low-noise OPAMP, such as the AD8067.

The analysis presented so far is valid whenever the gain of the transimpedance stage corresponds to the feedback impedance of the amplifier at the series-resonant frequency, depending on whether the condition of virtual short-circuit between the inputs of the OPAMP is respected. This condition is satisfied when the return ratio $|\vartheta(j\omega)|$ of the amplifier is high enough at ω_S . In a feedback loop circuit, the return ratio is defined as the ratio between the controlling variable and the dependent variable, when the independent source is set to zero. Figure 2.21 shows the equivalent circuit for the calculation of the return ratio.

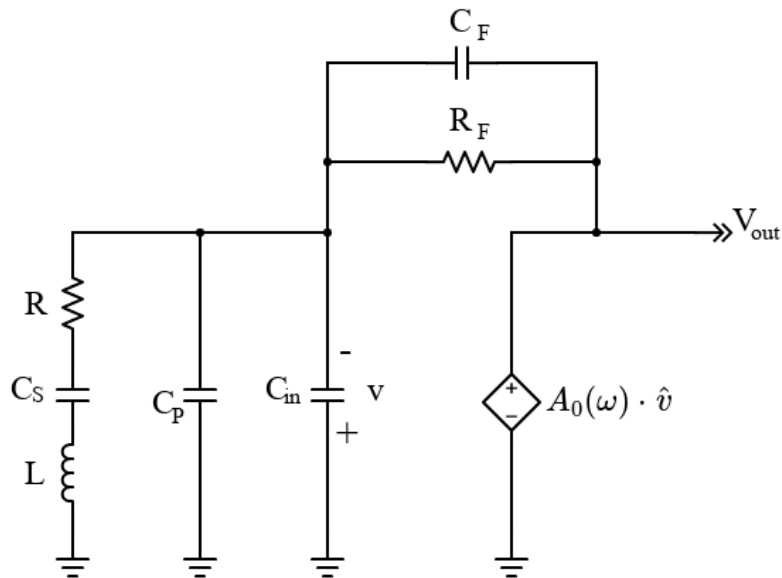


Figure 2.21 Equivalent circuit for the calculation of the return ratio.

The return ratio can be calculated with the following expression:

$$\vartheta(j\omega) = -\frac{v}{\hat{v}} \quad (2.37)$$

The study of the return ratio of the preamplifier is crucial to evaluate the stability of the analyzed configuration. The most important parameter which quantifies the stability of a feedback loop amplifier is the phase margin (PM). The phase margin is defined by the following expression:

$$PM = 180^\circ + \angle\vartheta(j\omega_x) \quad (2.38)$$

where ω_x is the frequency where the module of the return ratio is 0 dB.

A feedback loop system is stable only if the phase margin is positive; indeed, if the phase margin is close to zero degrees, the feedback of the system becomes positive, and the output signal of the circuit will oscillate without control, thus compromising the stability of the system.

Taking into account Eq. 2.37 and Fig. 2.21, the return ratio of the amplifier schematized in Fig. 2.14 is:

Furthermore, the study of the return ratio of the preamplifier is crucial to evaluate the phase margin and, in turn, the stability of the analyzed configuration.

The return ratio of the amplifier schematized in Fig. 2.16 is:

$$\vartheta(j\omega) = \frac{A_0(\omega) (1 + j\omega R_F C_F)(1 - \omega^2 L C_S + j\omega R C_S)}{1 - \omega^2 [L C_S + R_F R C_S (C_F + C_{P,tot})] + j\omega [R C_S + R_F (C_S + C_F + C_{P,tot}) - \omega^2 L R_F C_S (C_F + C_{P,tot})]} \quad (2.39)$$

where $A_0(\omega)$ is the open-loop gain of the AD8067 OPAMP as a function of the angular frequency [70]. The module of the return ratio shows a pole at $\omega_{pole} = 1/R_F(C_F + C_S + C_{P,tot})$ and a zero at $\omega_{zero} = 1/R_F C_F$. For $R_F = 10 \text{ M}\Omega$:

$$f_{pole} = \frac{\omega_{pole}}{2\pi} \cong 1.6 \text{ kHz} \quad (2.40)$$

$$f_{zero} = \frac{\omega_{zero}}{2\pi} \cong 160 \text{ kHz} \quad (2.41)$$

The open-loop gain of the AD8067 has a pole at $f_{OL} \cong 64 \text{ kHz}$; the first pole of $|\vartheta(j\omega)|$ is f_{pole} . As a consequence, the Gain Bandwidth product GBW of the TIA is:

$$GBW_{tia} = A_0 \cdot f_{pole} \cong 7 \text{ MHz} \quad (2.42)$$

$$A_0 = \frac{GBW_{op}}{f_{OL}} \cdot \sqrt{2} \quad (2.43)$$

where A_0 is the DC value of the open-loop gain and $GBW_{op} \cong 200 \text{ MHz}$ is the gain bandwidth product of the AD8067. Therefore, since f_{zero} is located between f_{OL} and GBW_{tia} , the phase margin is about 90 degrees, thus ensuring an excellent stability. Moreover, the module of the return ratio in correspondence of the series-resonant frequency is about 33 dB, which guarantees a good virtual short-circuit between the inputs of the operational amplifier. Figure 2.22 shows SPICE simulations of magnitude and phase of the return ratio for four different values of feedback resistance ($R_F = 1 \text{ M}\Omega$, $5 \text{ M}\Omega$, $10 \text{ M}\Omega$, $20 \text{ M}\Omega$).

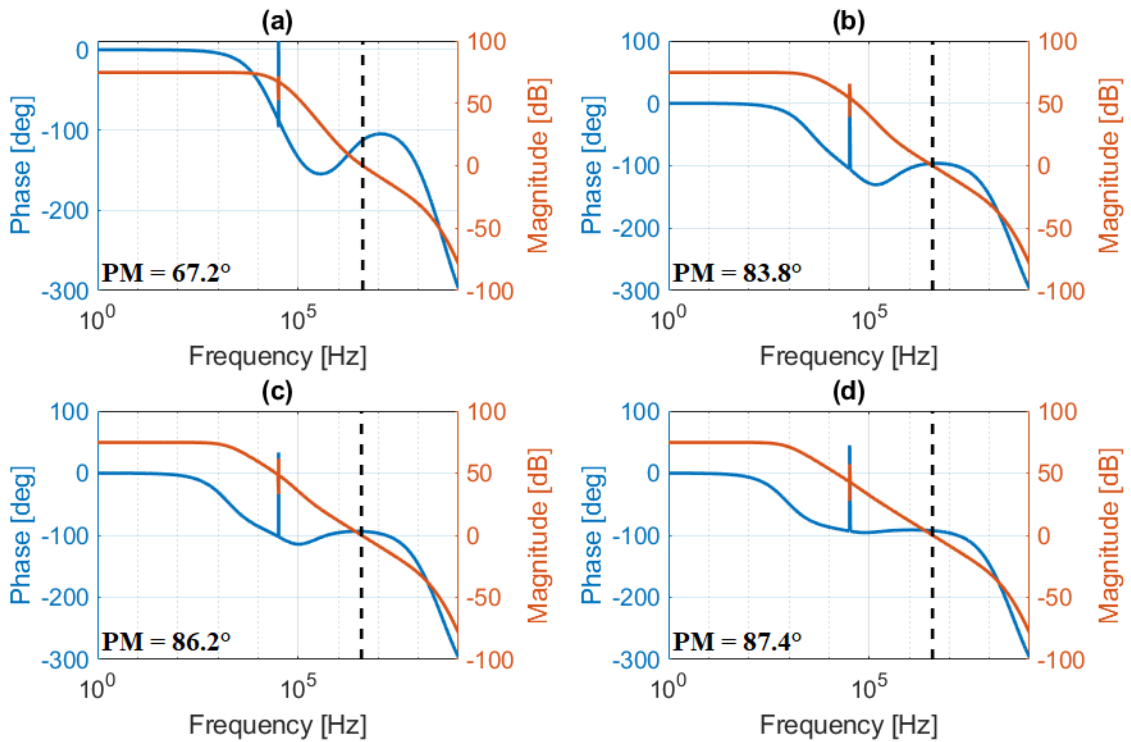


Figure 2.22 Magnitude and phase of the return ratio for (a) $R_F = 1 \text{ M}\Omega$, (b) $R_F = 5 \text{ M}\Omega$, (c) $R_F = 10 \text{ M}\Omega$, (d) $R_F = 20 \text{ M}\Omega$. Dashed black lines identify the frequencies at which the module of the return ratio is 0 dB.

The phase margin increases from 67.2° for $R_F = 1 \text{ M}\Omega$ up to 87.4° for $R_F = 20$

M Ω . Furthermore, as suggested by Eq. 2.35, increasing R_F improves the output SNR; as a preliminary result, the performance of a transimpedance amplifier may benefit from a high feedback resistance. However, it is worth mentioning that $|\vartheta(j\omega_S)|$ shows the opposite trend with respect to the phase margin: sweeping R_F from 1 M Ω to 20 M Ω causes a drop of $|\vartheta(j\omega_S)|$ from 52.3 dB to 27.6 dB, thus making the OPAMP virtual ground less effective. Moreover, since the impedance of the feedback network is limited by the parasitic capacitance C_F , it is not convenient to increase too much R_F . Therefore, the feedback resistance of a transimpedance amplifier must be properly chosen as a trade-off between the stability and reliability of the preamplifier.

2.3.3 Charge sensitive amplifier

The last examined configuration is the Charge Sensitive Amplifier (CSA). As already mentioned, the circuit diagram of a CSA and of a TIA are identical (see Fig. 2.16). The main difference is that in the CSA configuration, C_F is a physical capacitor and R_F is higher with respect to the transimpedance amplifier (~ 100 M Ω). The output signal is proportional to the electric charge deposited on the QTF due to piezoelectric effect [57, 58]:

$$V_{out}(t) = -\frac{q_{QTF}(t)}{C_F} = \frac{1}{C_F} \cdot \int_0^t i_{QTF}(\tau) d\tau \quad (2.44)$$

The feedback resistor R_F does not contribute to the output voltage, but it is needed to prevent the saturation of the operational amplifier. Since $1/\omega C_F \ll R_F$, the signal transfer function of the CSA can be calculated using the approximation in Eq. 2.27:

$$|H_{csa}(j\omega)|^2 = \left(\frac{C_S}{C_F}\right)^2 \frac{1}{(1 - \omega^2 LC_S)^2 + \omega^2 R^2 C_S^2} \quad (2.45)$$

At the series-resonant frequency:

$$|H_{csa}(j\omega_S)|^2 = \frac{1}{\omega_S^2 R^2 C_F^2} \quad (2.46)$$

A comparison with the gain of a TIA at the resonance frequency (see Eq. 2.28)

gives:

$$\frac{1}{\omega_S^2 R^2 C_F^2} = \frac{R_F^2}{R^2} \Rightarrow C_F = \frac{1}{\omega_S R_F} \quad (2.47)$$

Therefore, to get the same gain of a TIA with a 10 MΩ feedback resistance, a feedback capacitance of about 0.5 pF should be employed. However, this capacitance value is not feasible, as it is comparable to the stray capacitance of a printed circuit board. For this reason, high gains with a CSA cannot be reached. The comparison between the analytical model of the transfer function and data obtained by means of SPICE simulations is shown in Fig. 2.23, for four different values of C_F . The QTF parameters listed in Tab. 2.1 and the AD8067 SPICE model were employed in the analysis, while the feedback resistor R_F was set to 100 MΩ.

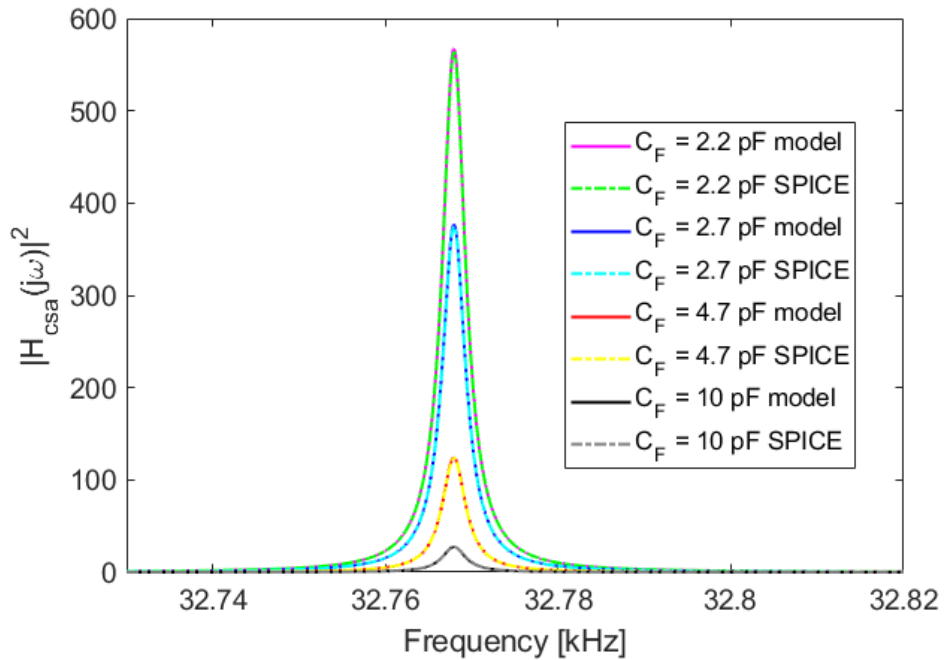


Figure 2.23 Comparison between analytical model and SPICE simulations of the signal transfer function, for $C_F = 2.2$ pF, 2.7 pF, 4.7 pF and 10 pF.

The curves computed with Eq. 2.45 and those obtained by SPICE simulations are in good agreement. It is worth noticing that, as already observed in the TIA configuration, the peak of the output signal lies at the series-resonant frequency,

regardless of the parameters of the readout electronics.

The equivalent circuit for the calculation of the output noise is identical to the one reported in Fig. 2.19. The contribution of the QTF intrinsic resistance to the output noise spectral density is:

$$S_{n,QTF}(\omega) = 4kTR \cdot |H_{csa}(j\omega)|^2 \quad (2.48)$$

At the series resonance frequency, it results:

$$S_{n,QTF}(\omega_S) \cong \frac{4kTR}{\omega_S^2 R^2 C_F^2} = \frac{4kT}{\omega_S^2 R C_F^2} \quad (2.49)$$

The i_n - noise contribution can be compared to the same contribution in the TIA configuration. Neglecting R_F and C_F in the CSA and in the TIA, respectively, one obtains:

$$S_{i_n,csa}(\omega_S) \cong \frac{i_n^2}{\omega_S^2 C_F^2} \quad (2.50)$$

$$S_{i_n,tia}(\omega_S) \cong i_n^2 \cdot R_F^2 \quad (2.51)$$

By comparing these expressions with Eqs. 2.46 and Eq. 2.28, it can be noticed that the reduction of the current noise in the CSA is proportional to the reduction of the gain at the resonance frequency. Hence, the contribution of the OPAMP current noise is negligible in the CSA as well.

The transfer function of the OPAMP voltage noise is expressed by:

$$S_{n,op}(j\omega) = e_n^2 \left(\frac{C_P + C_S + C_F}{C_F} \right)^2 \frac{\left(1 - \omega^2 \frac{LC_S(C_F + C_P)}{C_S + C_F + C_P} \right)^2 + \omega^2 R^2 \left(\frac{C_S(C_F + C_P)}{C_S + C_F + C_P} \right)^2}{(1 - \omega^2 LC_S)^2 + \omega^2 R^2 C_S^2} \quad (2.52)$$

This function peaks in correspondence of ω_S , where its value is:

$$S_{n,op}(j\omega_S) = e_n^2 \left[\left(1 + \frac{C_P}{C_F} \right)^2 + \frac{1}{\omega_S^2 R^2 C_F^2} \right] \cong \frac{e_n^2}{\omega_S^2 R^2 C_F^2} \quad (2.53)$$

Finally, the noise spectral density associated to the feedback resistor R_F is:

$$S_{n,F}(j\omega) = \frac{4kTR_F}{1 + \omega^2 R_F^2 C_F^2} \cong \frac{4kT}{\omega^2 R_F C_F^2} \quad (2.54)$$

which is almost constant around the series-resonant frequency.

Figure 2.24 displays the output noise spectral density associated to each noise contribution, for four different values of the feedback capacitor.

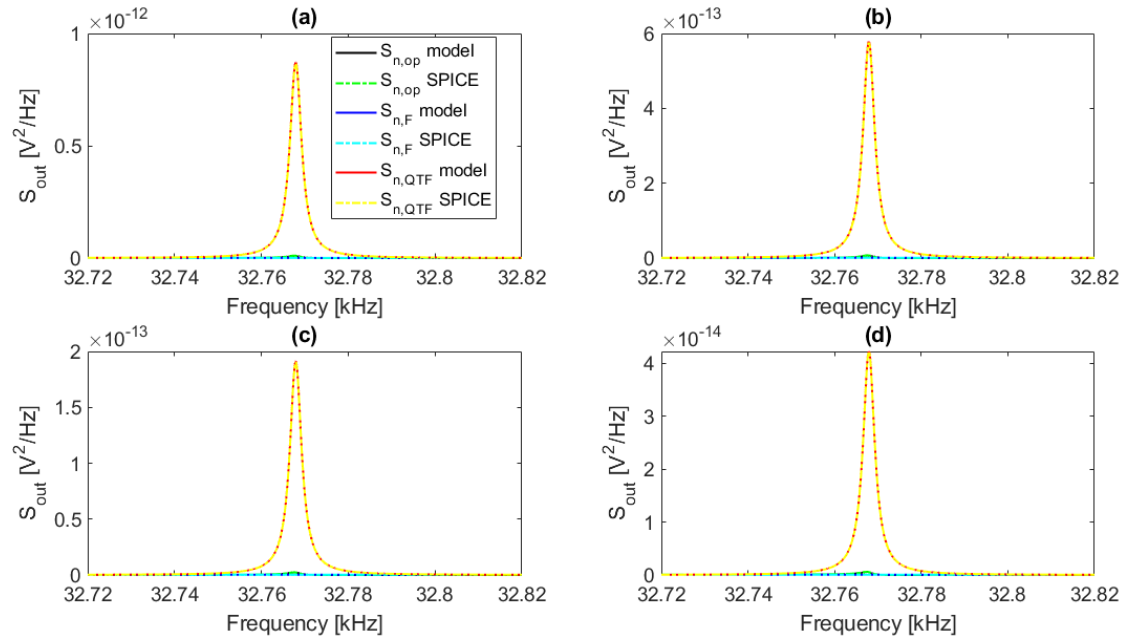


Figure 2.24 Contributions to the overall output noise spectral density due to the OPAMP and resistors R_F and R , for (a) $C_F = 2.2$ pF, (b) $C_F = 2.7$ pF, (c) $C_F = 4.7$ pF, (d) $C_F = 10$ pF: comparison between the results obtained with the analytical model and SPICE simulations.

As observed in the previously discussed configurations, the matching between the analytical model and the outcome of SPICE simulations is excellent. In addition, the dominant noise contribution is the one associated to the intrinsic resistance of the QTF, regardless of the value of C_F . The noise contributions associated to the OPAMP and to the feedback resistor are both negligible, regardless of the value of the gain parameter C_F . This behavior differs from what was observed in the analysis of the TIA configuration, where the contribution of the feedback resistor can be neglected only if

R_F is sufficiently high ($> 5 \text{ M}\Omega$). Since in the CSA configuration R_F is much higher than in TIA, the R_F output noise contribution is much lower (as suggested by Eq. 2.54). Moreover, the SNR associated to the noise of the feedback resistor is independent of C_F at the series-resonant frequency:

$$SNR_{R_F}(\omega_S) = \frac{\frac{1}{\omega_S^2 R^2 C_F^2}}{\frac{4kT}{\omega_S^2 R C_F^2}} = \frac{1}{4kTR} \quad (2.55)$$

Hence, this contribution depends only on R , which is an intrinsic parameter of the QTF.

As for the noise contribution of the OPAMP, SNR_{op} can be easily derived from Eq. 2.53:

$$SNR_{op}(\omega_S) = \frac{\frac{1}{\omega_S^2 R^2 C_F^2}}{\frac{e_n^2}{\omega_S^2 R^2 C_F^2}} = \frac{1}{e_n^2} \quad (2.56)$$

This ratio corresponds exactly to the one computed in TIA configuration (see Eq. 2.36), therefore, choosing a low-noise operational amplifier, the noise contribution from the OPAMP can be neglected in both configurations.

Let us now analyze the return ratio in the CSA configuration. The expression of the return ratio is identical to the one already discussed in the TIA configuration (see Eq. 2.39). The main difference is that R_F and C_F values are higher, hence the pole and the zero of the return ratio are located at lower frequencies. Considering Eqs. 2.40 and 2.41 for $C_F = 2.2 \text{ pF}$, one obtains:

$$f_{pole} = 142 \text{ Hz} \quad (2.57)$$

$$f_{zero} = 723.4 \text{ Hz} \quad (2.58)$$

Unlike the TIA configuration, f_{pole} and f_{zero} are closer to each other and further from the OPAMP pole f_{OL} . This implies that in correspondence of ω_S , the module of the return ratio is remarkably higher, thus ensuring a good virtual ground at the inputs of the amplifier.

Figure 2.25 shows the magnitude and phase of the return ratio in the CSA for C_F

= 2.2 pF, 2.7 pF, 4.7 pF and 10 pF.

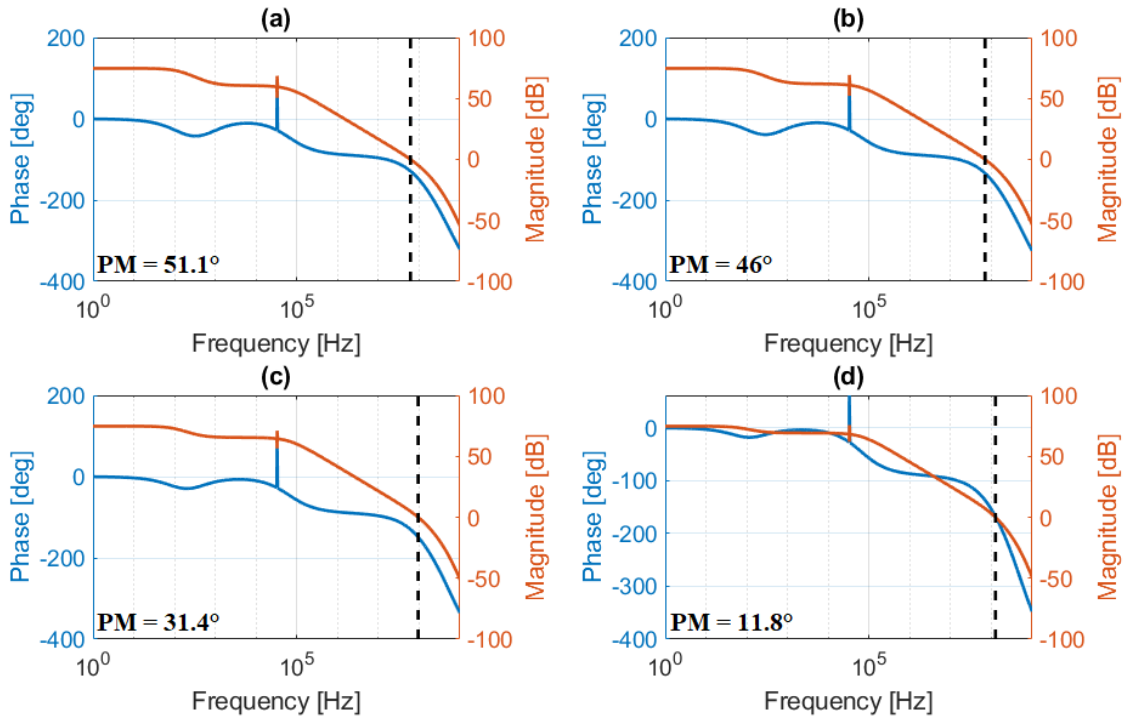


Figure 2.25 Magnitude and phase of the return ratio for (a) $C_F = 2.2$ pF, (b) $C_F = 2.7$ pF, (c) $C_F = 4.7$ pF, (d) $C_F = 10$ pF. Dashed black lines identify the frequencies at which the module of the return ratio is 0 dB.

The module of $|\vartheta(j\omega)|$ assumes its highest value (58.4 dB) for $C_F = 10$ pF, and decreases with the feedback capacitance, up to 45.9 dB for $C_F = 2.2$ pF. The unity gain frequency GBW is remarkably higher with respect to the TIA configuration, ranging from 62 MHz for $C_F = 2.2$ pF to 126 MHz for $C_F = 10$ pF. Therefore, GBW is very close to the out-of-band pole of the AD8067, which lies at about 334 MHz. Consequently, an increase of C_F beyond 2.7 pF leads to a drastic drop of the phase margin (11.8° for $C_F = 10$ pF), which may cause instabilities.

In conclusion, since the SNR is not affected by variations of C_F , it is preferable to work with low values of the feedback capacitor ($C_F < 3$ pF), keeping both a good phase margin and a high return ratio.

Chapter 3: Lock-in Amplifier modeling for noise analysis

The output signal of the analog preamplifier employed for the QTF readout needs further processing to successfully exploit its resonance properties. Synchronous detection techniques based on lock-in amplifiers (LIAs) are utilized in QEPAS to extract the desired signal harmonic from the noise floor [68]. The use of a LIA in the signal conditioning chain of a QEPAS sensor allows the enhancement of the SNR, thus improving the sensitivity of the sensing system [50]. LIAs exploit phase sensitive detection based on a mixer and an adjustable low-pass filter (LPF) to retrieve the output signal. In particular, the low-pass filter influences the noise level at the output of the LIA; therefore, the choice of the LPF time constant crucially impacts on the output SNR and, in turn, on the detection capabilities of the sensor.

In this chapter, a brief overview of the LIA working principle is provided, focusing on the time domain response of a low-pass filter. Finally, the influence of the LPF time constant on the output SNR for each preamplifier configuration is discussed, and results are compared.

3.1 Lock-in amplifier working principle

The structure of a LIA was described in section 2.2 and sketched in Fig. 2.2. The main feature of a LIA is its capability to retrieve low amplitude signals, up to few nV [69], in a noisy background, by means of a phase-sensitive detector (PSD). PSD consists of a multiplier and a low-pass filter (see Fig. 2.2).

Assuming that an analog signal is fed to the input of a LIA, this can be represented as the sum between the ω_s -frequency component to be extracted and all other components (treated as noise components), according to the Fourier theorem:

$$V_s(t) = A_s \cos(\omega_s t + \varphi_s) + \sum_{\omega_n} A_n \cos(\omega_n t + \varphi_n) \quad (3.1)$$

where the subscript “s” refers to the signal, and the subscript “n” refers to the noise components.

The reference signal $V_{ref}(t)$ is then multiplied by $V_s(t)$:

$$V_s(t) \cdot V_{ref}(t) = A_s A_{ref} \cos(\omega_s t + \varphi_s) \cos(\omega_{ref} t + \varphi_{ref}) + A_{ref} \cos(\omega_{ref} t + \varphi_{ref}) \sum_{\omega_n} A_n \cos(\omega_n t + \varphi_n) \quad (3.2)$$

This expression can be rewritten as follows:

$$\begin{aligned} V_s(t) \cdot V_{ref}(t) &= \frac{A_s A_{ref}}{2} \{ \cos[(\omega_s + \omega_{ref})t + (\varphi_s + \varphi_{ref})] \} \\ &+ \frac{A_s A_{ref}}{2} \{ \cos[(\omega_s - \omega_{ref})t + (\varphi_s - \varphi_{ref})] \} \\ &+ \frac{A_{ref}}{2} \sum_{\omega_n} A_n \cos[(\omega_n + \omega_{ref})t + (\varphi_n + \varphi_{ref})] \\ &+ \frac{A_{ref}}{2} \sum_{\omega_n} A_n \cos[(\omega_n - \omega_{ref})t + (\varphi_n - \varphi_{ref})] \end{aligned} \quad (3.3)$$

This signal is sent to a low-pass filter, which preserves only its DC component. Therefore, only the terms $\omega_s = \omega_{ref}$ and $\omega_n = \omega_{ref}$ are nonzero. As a result, the in-phase component of the output signal can then be expressed as:

$$V_x = \frac{A_s A_{ref}}{2} \cos(\varphi_s - \varphi_{ref}) + \frac{A_{ref} A_n}{2} \cos(\varphi_n - \varphi_{ref}) \quad (3.4)$$

Hence, the output signal of a LIA is sensitive to the phase difference between the ω_s -frequency component of the input signal and the reference one; moreover, only the noise component at the reference frequency affects the output signal.

The quadrature component is obtained employing a second PSD; the input signal is multiplied by the 90° shifted-version of the reference signal; the out-of-phase component can then be retrieved applying a low-pass filter to the output of the

multiplier:

$$V_y = \frac{A_s A_{ref}}{2} \sin(\varphi_s - \varphi_{ref}) + \frac{A_{ref} A_n}{2} \sin(\varphi_n - \varphi_{ref}) \quad (3.5)$$

The quadrature component is proportional to the sine of the phase shift between $V_s(t)$ and $V_{ref}(t)$ (see Eq. 2.3), therefore if A_{ref} is known, it is possible to get A_s and φ_s from the measured values of V_x and V_y .

PSDs can be implemented either in analog or in digital LIAs. In digital LIAs, the input signal is digitalized by means of an A/D converter [69]. Since the reference sine waves are computed with high resolutions (up to 20 bits of accuracy), digital LIAs show better harmonic suppression with respect to their analog version. In addition, they are offset-free and are not sensitive to amplitude drifts [69]. For these reasons, digital PSDs are usually preferable to analog PSDs.

3.2 Modeling of the lock-in filter

The low-pass filter of a PSD plays a key role in the maximization of the output SNR, since it suppresses the noise at the output of the LIA. As an approximation, let us consider an RC low-pass filter model [68]; its transfer function is:

$$H(j\omega) = \frac{1}{(1 + j\omega\tau)^n} \quad (3.6)$$

where τ is the time constant and n is the filter order.

The output signal of the LPF in the frequency domain can be easily retrieved by multiplying the filter transfer function by the Fourier transform of the demodulated signal. Since the demodulation operation shifts the spectrum of the LIA input signal around the reference frequency $\omega_{ref} = 2\pi f_{ref}$, the output signal of the lock-in amplifier is:

$$V_{out}(\omega) = V_{in}(\omega - \omega_{ref})H(j\omega) \quad (3.7)$$

Therefore, LIA operates as a bandpass filter, that picks out the frequency spectrum centered at f_{ref} and extends it on both sides by the LPF bandwidth [50,68]. When the

QTF is excited at its series-resonant frequency f_s , the spectral distribution of the preamplifier output signal can be modelled as a Dirac delta function. Consequently, the bandwidth of the LPF does not affect the LIA output signal. On the other hand, the input noise of the LIA (which corresponds to the output noise of the preamplifier) has its own proper spectral distribution, as shown in chapter 2. This implies that the output noise level depends both on the noise spectral density at the output of the preamplifier, and on the parameters of the low-pass filter. In particular, the cut-off frequency of the filter f_{3dB} depends either on the time constant τ and on the filter order n . The order n , in addition, contributes to the steepness of the filter: a higher value of n increases the filter roll-off, thus improving its selectivity, but makes the filter more complex.

The relationship between f_{3dB} , n and τ is expressed by the following relation [73]:

$$f_{3dB}^{(n)} = \frac{\sqrt{2^{1/n} - 1}}{2\pi\tau} \quad (3.8)$$

meaning that, for a fixed time constant, the cut-off frequency of the filter decreases as the filter order increases. Conversely, if the LPF order is fixed, f_{3dB} decreases as τ increases, thus making the filter more selective. This behavior is shown in Fig. 3.1.

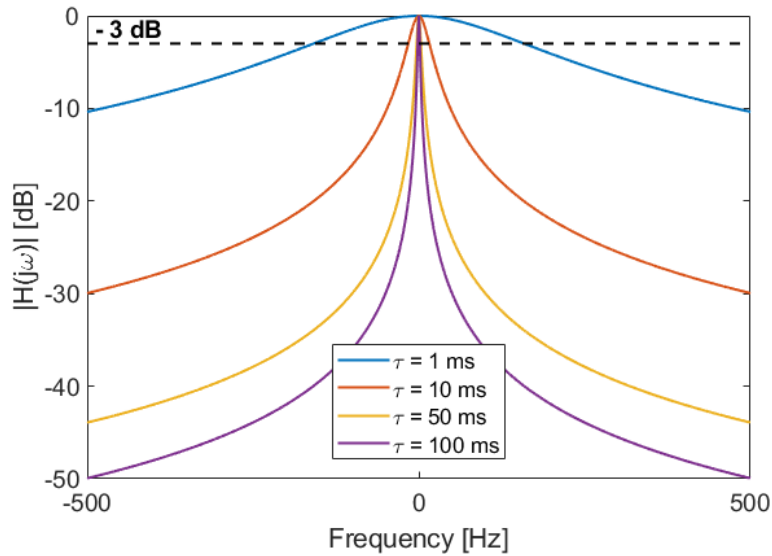


Figure 3.1 Magnitude of the transfer function of a first order LPF, for $\tau = 1$ ms, 10 ms, 50 ms and 100 ms.

It is convenient to define a filter in terms of its equivalent noise bandwidth (ENB),

rather than its cut-off frequency. The ENB is the bandwidth of an equivalent brick-wall filter with an equivalent white noise at the output as the filter under investigation [50,68]. The relation between the ENB, the order n and the time constant τ is:

$$ENB^{(n)} = \frac{(2(n-1))!}{(2^n(n-1)!)^2} \cdot \frac{1}{\tau} \quad (3.9)$$

To study the behavior of a low-pass filter in the time domain, it is useful to analyze the response of the system to a voltage step signal, as depicted in Fig. 3.2.

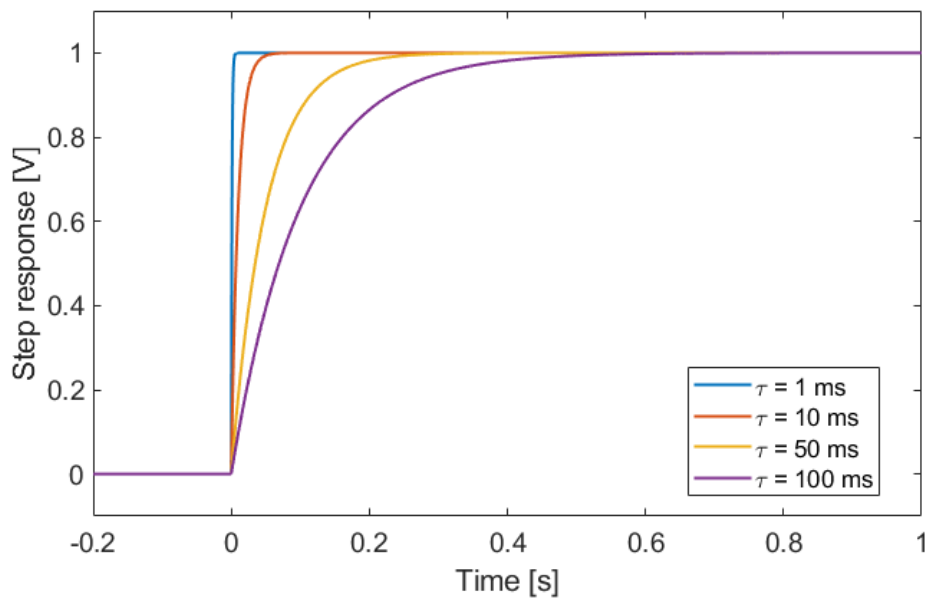


Figure 3.2 Step response of a first order low-pass filter to a step input signal with a 1 V amplitude.

Longer τ implies longer times for the signal to reach a steady-state value. Table 3.1 shows the main frequency and time domain parameters of a low-pass filter, up to the fourth order [68,74].

n	Filter roll-off		Bandwidth		
	dB/oct	dB/dec	f_{3dB} [1/ τ]	ENB [1/ τ]	$t_{settle,95\%}$ [s]
1	6	20	0.1592	0.2500	$4.6 \cdot \tau$

2	12	40	0.1024	0.1250	$6.6 \cdot \tau$
3	18	60	0.0811	0.0937	$8.4 \cdot \tau$
4	24	80	0.0692	0.0781	$10 \cdot \tau$

Table 3.1 Overview of the properties of a n^{th} order low-pass filter.

A longer time constant improves the noise suppression capabilities of the filter, but it negatively affects the acquisition time. As an example, at $\tau = 1$ ms for a second order filter ENB is equal to 125 Hz, and the corresponding settling time at 95% is 6.6 ms; at $\tau = 100$ ms, in a filter of the same order, the ENB is 100 times lower, but the settling time is 100 times higher. Accordingly, increasing the order n , the filter becomes sharper and more selective, but the settling time gets longer. In conclusion, a trade-off between accuracy and response time must be carefully chosen for setting a proper LIA time constant, especially if fast QEPAS measurements are required.

3.3 Influence of lock-in amplifier time constant in the three amplifier configurations

Synchronous detection techniques, based on laser modulation and LIA, are always used in QEPAS sensors to increase the SNR of the measurements. In chapter 2, the amplitude of the signal and its noise spectral density were retrieved in the frequency domain at the output of the three different preamplifiers. These expressions can be conveniently exploited to evaluate the SNR at the output of the LIA. Thanks to synchronous demodulation and narrow-band low-pass filtering, the LIA output signal is a DC level proportional to the amplitude of the preamplifier response, at the operation frequency. When the preamplifier response is acquired at the QTF resonance frequency, the SNR can be investigated in a small range around f_s . Thus, if the preamplifier response is acquired at a certain frequency f_{op} close to f_s , the output signal is proportional to $|H(f_{op})|$. Regarding noise components, because of the demodulation, the only the noise spectrum centered around the LIA reference frequency is transferred to LIA. This noise is then filtered by means of the LIA narrow low-pass filter. As a result,

the LIA operates as a narrow band-pass filter centered around its reference frequency. Hence, LIA was modelled as a biquadratic band-pass filter with a transfer function $H_{LIA}(\omega)$ given by:

$$H_{LIA}(\omega) = \frac{j \frac{\omega_{op}}{Q} \omega}{\omega_{op}^2 - \omega^2 + j \frac{\omega_{op}}{Q} \omega} \quad (3.10)$$

In the following sections, the influence of the LIA time constant on the output noise level in the three preamplifier configurations will be discussed. General guidelines for the choice of the amplifier parameters will be derived, aimed at maximizing the SNR and optimizing the acquisition time in QEPAS measurements.

3.3.1 Voltage amplifier

Considering the results obtained in section 2.3.1, the main noise contributions in the voltage preamplifier are associated to the QTF intrinsic resistance R and the bias resistor R_L . The QTF intrinsic resistance is also characterized by an amplitude flicker noise contribution, which does not provide any meaningful contribution to the overall amplitude noise in the bandwidth of interest [93]. The phase flicker noise contribution of R was not considered in this analysis. Therefore, the behavior of the SNR at the output of the LIA as a function of the chosen operating frequency $f_{op} = \omega_{op}/2\pi$ can be described by means of the following expression:

$$\begin{aligned} SNR_n(\omega_{op}) &= \frac{|H_v(\omega_{op})|}{\sqrt{\int_{-\infty}^{+\infty} S_{n,tot}(\omega) |H_{LIA}(j\omega)|^2 d\omega}} = \\ &\cong \frac{|H_v(\omega_{op})|}{\sqrt{\int_{-\infty}^{+\infty} S_{n,QTF}(\omega) |H_{LIA}(j\omega)|^2 d\omega + \int_{-\infty}^{+\infty} S_{n,L}(\omega) |H_{LIA}(j\omega)|^2 d\omega}} \end{aligned} \quad (3.11)$$

where the amplitude of the input signal V_{in} was normalized to 1 V.

By separating the noise contributions for R and R_L , two expressions can be defined:

$$SNR_{n,QTF}^2(\omega_{op}) = \frac{|H_v(\omega_{op})|^2}{\int_{-\infty}^{+\infty} S_{n,QTF}(\omega) |H_{LIA}(j\omega)|^2 d\omega} \quad (3.12)$$

and

$$SNR_{n,L}^2(\omega_{op}) = \frac{|H_v(\omega_{op})|^2}{\int_{-\infty}^{+\infty} S_{n,L}(\omega) |H_{LIA}(j\omega)|^2 d\omega} \quad (3.13)$$

Thus, the overall normalized squared-SNR can be rewritten as follows:

$$SNR_n^2 = \frac{1}{\sum_i \frac{1}{SNR_{n,i}^2}} = \frac{1}{\frac{1}{SNR_{n,QTF}^2} + \frac{1}{SNR_{n,L}^2}} \quad (3.14)$$

First, let us consider a very narrow-bandwidth $f_{3dB} = 0.5$ Hz, corresponding to a settling time of ~ 1.3 s for an equivalent first-order LIA low-pass filter. In this case, the behavior of the integrated noise as a function of f_{op} is expected to be very similar to the output noise spectral density. Since the R -noise and the signal have the same transfer function $H_v(f)$, the $SNR_{n,QTF}$ contribution is expected to be almost spectrally flat. Nonetheless, considering a representative value for $R_L = 100$ k Ω , $SNR_{n,QTF}$ peaks as $|H_v(f)|$, because of the effect of integration, as reported in Fig. 3.3. For a bandpass filter, the effect of the integration bandwidth on the input noise spectral density can be more intuitively represented by means of a simple brick-wall filter.

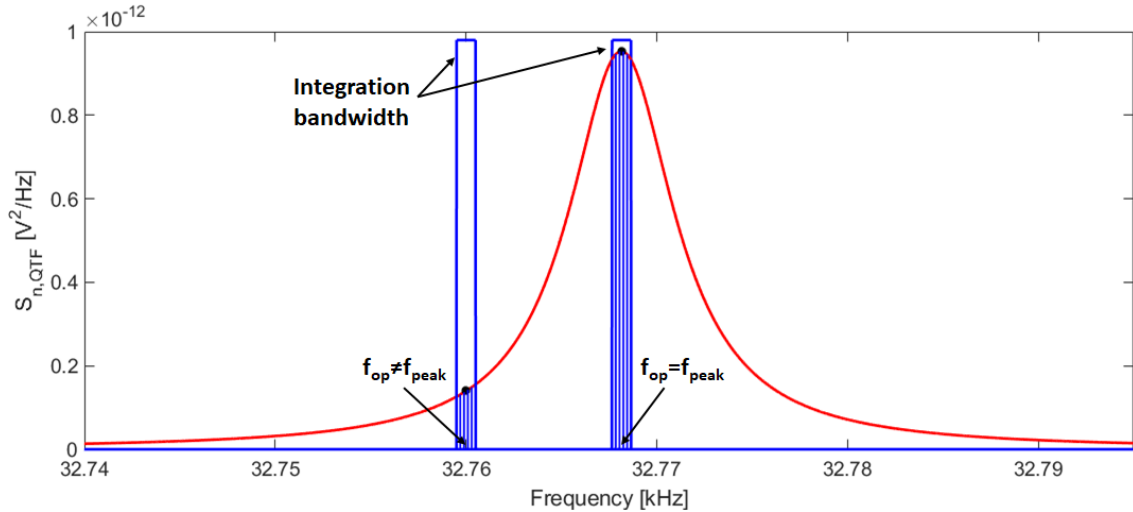


Figure 3.3 Integration of the contribution $S_{n,QTF}$ (red line), due to R , to the total output spectral noise density at a low-pass filter bandwidth of 0.5 Hz around the operating frequency f_{op} , for $f_{op} = f_{peak}$ and $f_{op} \neq f_{peak}$ ($R_L = 100 \text{ k}\Omega$).

Indeed, in the narrow integration bandwidth, the function $S_{n,QTF}(f)$ takes monotonically decreasing values on both sides of $f_{op}=f_{peak}$; whereas, for any other frequency values, $S_{n,QTF}(f)$ decreases in one direction and increases in the other one, as reported in Fig. 3.3. As a consequence, the value of the integrated noise normalized to the value of the signal reaches a minimum value at $f_{op}=f_{peak}$, generating a peak value in the function $SNR_{n,QTF}(f_{op})$.

The presence of a peak value for $SNR_{n,QTF}$ is also visible in Fig. 3.4, which reports $SNR_{n,QTF}$ as a function of the frequency f_{op} , for different values of R_L . Moreover, for increasing values of R_L , the peak moves from f_S to f_P ; for large values of R_L , it becomes slightly more pronounced, even if the overall behavior remains almost spectrally flat.

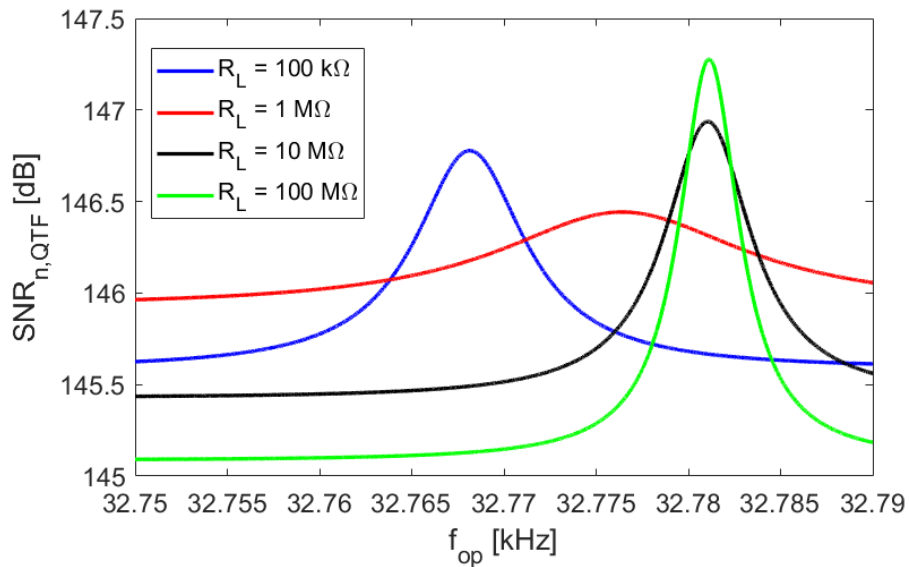


Figure 3.4 QTF noise contribution to the SNR_n at the LIA output as a function of the operating frequency, for different values of R_L and at a low-pass filter bandwidth of $f_{3dB} = 0.5 \text{ Hz}$.

As for the term $SNR_{n,L}$, its behavior as a function of f_{op} is strongly affected by the minimum of the noise spectral density $S_{n,L}$ at f_S . This effect prevails over the peak value

of the signal, which moves towards f_p for increasing values of R_L , resulting in a local maximum value on $SNR_{n,L}$ which appears at the series-resonant frequency f_s for any value of R_L . Figure 3.5 shows the behavior of $SNR_{n,L}$ as a function of the operation frequency, for different R_L values.

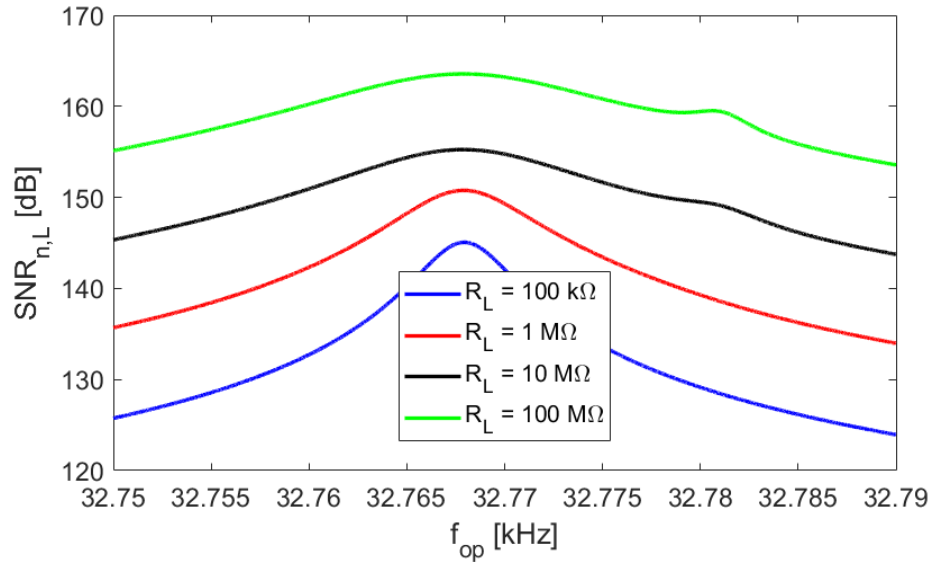


Figure 3.5 R_L noise contribution to the SNR_n at the LIA output as a function of the operating frequency, for different values of R_L and at a low-pass filter bandwidth $f_{3dB} = 0.5$ Hz.

Higher values of $SNR_{n,L}$ are obtained as R_L increases. Therefore, as reported in Eq. 3.14, $SNR_{n,QTF}$ becomes crucial in the calculation of the overall SNR for large values of R_L .

Let us consider the overall SNR at the LIA output given by Eq. 3.14 as a function of f_{op} . Figure 3.6 reports the SNR_n as a function of f_{op} for different values of R_L with $f_{3dB} = 0.5$ Hz.

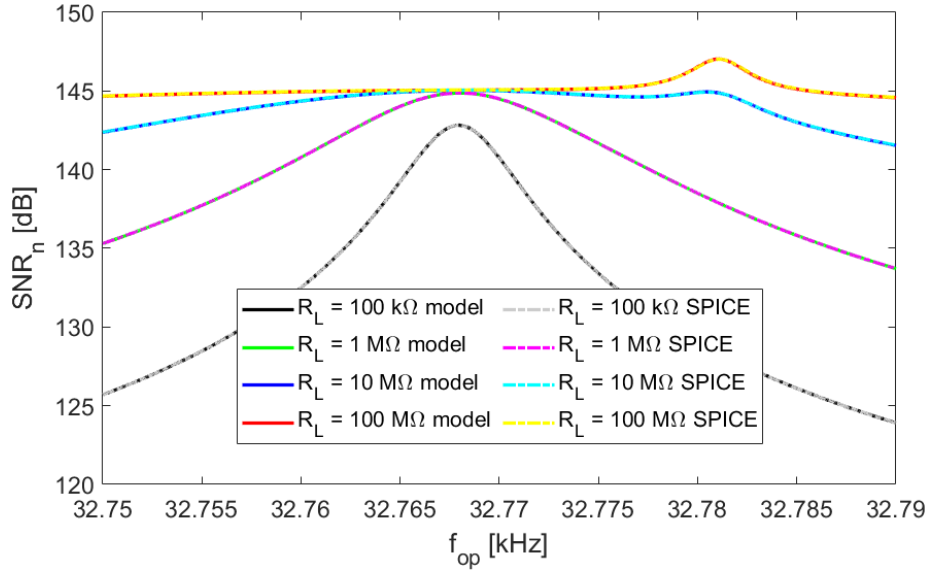


Figure 3.6 Total normalized signal-to-noise ratio SNR_n at the LIA output as a function of the operation frequency, for different values of R_L and at a low-pass filter bandwidth of $f_{3dB} = 0.5$ Hz (solid lines). The corresponding results of SPICE simulations are also reported as dotted lines.

A comparison between the results given by the analytical model and the corresponding SPICE simulation is also provided, showing an excellent agreement between the two methods of simulation. For low values of R_L , $SNR_{n,QTF}$ is almost flat (see Fig. 3.4) and the peak of the total SNR_n coincides with the peak of $SNR_{n,L}$. Hence, the best operation frequency for QEPAS is the series-resonant frequency f_S of the QTF. As R_L increases, as already pointed out, the contribution of $SNR_{n,L}$ becomes less relevant, thus a local peak in the SNR_n function appears, corresponding to the peak of $SNR_{n,QTF}$, which occurs at the parallel-resonant frequency f_P .

Figure 3.6 shows that the SNR_n peak feature at f_S becomes less sharp as R_L increases. For $R_L = 100$ M Ω , the SNR_n becomes quite flat around f_S and a sharp peak appears at f_P . In general, slightly better results in terms of SNR are obtained with large values of R_L . The study above was carried out for a LIA with a very narrow-band filter, which is useful when long acquisition time for a single measurement can be tolerated. With fast measurements [76,77], the bandwidth of the LIA filter must be increased, and the results of the previous analysis must be revised. Moreover, when fast measurements

are needed, the QTF response time is another parameter to be included in the discussion. Being an acoustic resonator, the QTF response time is given by:

$$\tau = \frac{Q}{\pi f_s} \quad (3.15)$$

For a standard 32.7 kHz-QTF having at atmospheric pressure $Q \sim 13000$, a long integration time (300 to 400 ms) is required for the acquisition of the LIA output signal. Nevertheless, specific QEPAS techniques such as Beat Frequency (BF) QEPAS exploit the fast transient response of an acoustically excited QTF to retrieve the gas concentration, the resonance frequency, and the quality factor of the QTF [78]. This approach overcomes the limitations imposed by the time response of the QTF, allowing shorter acquisition times and faster measurements.

Regarding the contribution to the total SNR at the LIA output due to the resistor R , since the integration bandwidth is larger, the effect of the integration around f_{peak} , (see Fig. 3.3) is more relevant. Consequently, the peak of $SNR_{n,QTF}$ as a function of the operation frequency centered at f_{peak} becomes sharper and more pronounced. Figure 3.7 shows the behavior of $SNR_{n,QTF}$ as a function of f_{op} when $f_{3dB} = 5$ Hz, corresponding to a settling time of about 130 ms for an equivalent first order LIA low-pass filter, for the same values of R_L considered in Fig. 3.4.

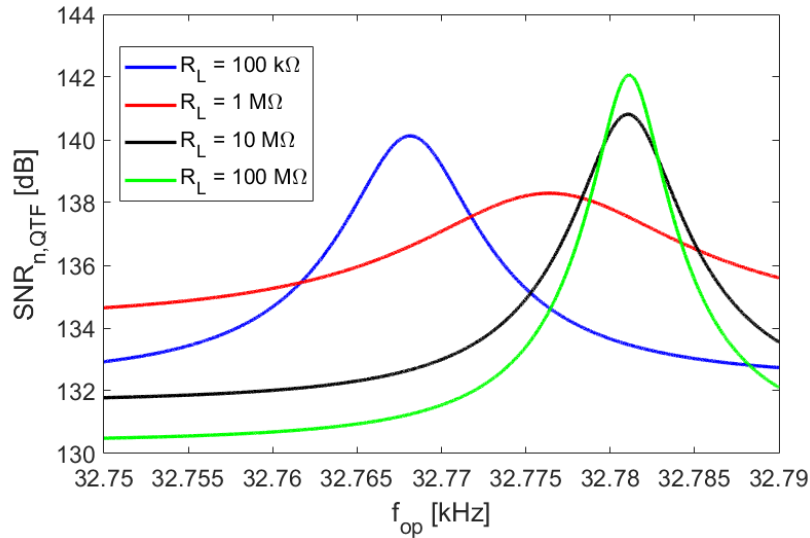


Figure 3.7 R_L noise contribution to the SNR_n at the LIA output as a function of the operation frequency, for different values of R_L and at a low-pass filter bandwidth of $f_{3dB} = 5$ Hz.

Let us analyze the R_L noise contribution to the SNR for increasing values of the LIA bandwidth. The effect of the minimum of $S_{n,L}$ at f_S tends to be less relevant, because of the increase of the integration bandwidth. Therefore, the function $SNR_{n,L}$ becomes flatter around the series-resonant frequency. Nonetheless, for small values of R_L , the peak of the signal is located at f_S and, consequently, the peak of $SNR_{n,L}$ is still at f_S . Increasing R_L , the peak value moves towards the parallel-resonant frequency f_P and the effect of the minimum of $S_{n,L}$ becomes less relevant, so $SNR_{n,L}$ tends to be flat. For large values of R_L , $S_{n,L}$ values decrease (see Fig. 2.13c,d), whereas the peak value at f_P increases; as a result, $SNR_{n,L}$ exhibits a peak at f_P , which becomes sharper as R_L increases. The behavior of $SNR_{n,L}$ as a function of the operation frequency f_{op} is shown in Fig. 3.8 for $f_{3dB} = 5$ Hz.

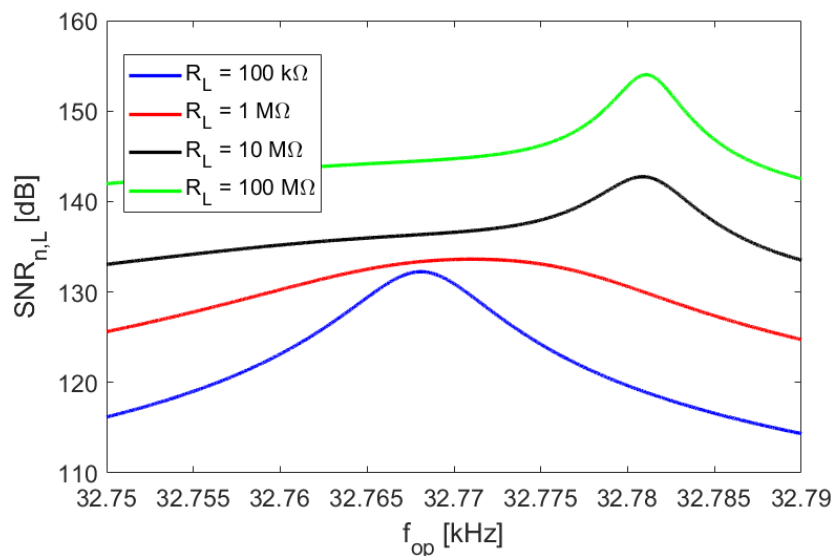


Figure 3.8 R_L noise contribution to the SNR_n at the LIA output as a function of the operation frequency, for different values of R_L and at a low-pass filter bandwidth of $f_{3dB} = 5$ Hz.

Finally, Figure 3.9 shows the SNR_n functions for low values of R_L .

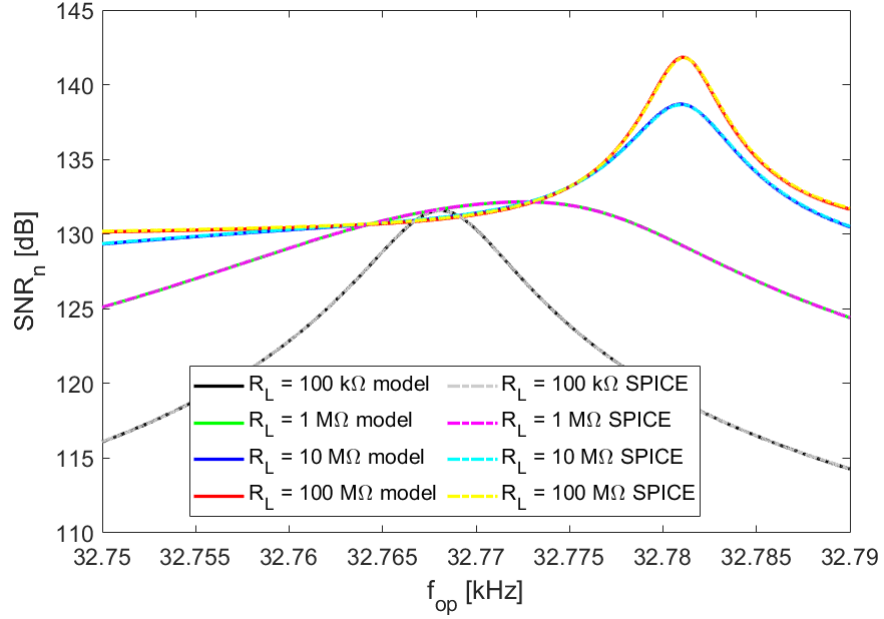


Figure 3.9 Total SNR_n at the LIA output as a function of the operation frequency, for different values of R_L and at a low-pass filter bandwidth of $f_{3dB} = 5$ Hz (solid lines). The corresponding results of SPICE simulations are also reported (dotted lines).

As R_L increases, the SNR_n peak at f_s becomes less pronounced: for R_L values larger than ~ 1 M Ω , a peak appears close to f_p , where both $SNR_{n,QTF}$ and $SNR_{n,L}$ have their maximum value. This peak is sharper as R_L increases, as shown in Fig. 3.9, which represents the trend of SNR as a function of f_{op} for $f_{3dB} = 5$ Hz. The SNR_n peak at 100 M Ω is more than two times higher than the values close to f_s . As before, SPICE simulations are in excellent agreement with the results provided by the analytical model.

Finally, the Normalized Noise Equivalent Absorption (NNEA), an important parameter to compare QEPAS sensors [19,63,71,78,79], can be calculated. NNEA is defined as:

$$NNEA = \frac{P \cdot \alpha}{SNR \cdot \sqrt{\Delta f}} \quad (3.16)$$

where P is the laser optical power, α is the absorption coefficient of the gas under investigation, SNR is the signal-to-noise ratio, and Δf is the integration bandwidth.

In [63], an NNEA of $5.0 \cdot 10^{-9}$ W \cdot cm $^{-1}/\sqrt{\text{Hz}}$ for the detection of CO $_2$ in an N $_2$

mixture, employing a transimpedance amplifier with a 10 M Ω feedback resistor and a narrow-bandwidth LIA filter, was demonstrated. Employing a voltage preamplifier with a 10 M Ω bias resistor and an integration bandwidth of 0.5 Hz, a 100 M Ω bias resistor and the same integration bandwidth would lead to a NNEA of $4.4 \cdot 10^{-9} \text{ W}\cdot\text{cm}^{-1}/\sqrt{\text{Hz}}$, with improvement of a factor of 1.1. Moreover, with a 5 Hz LIA filter bandwidth, a NNEA of $5.8 \cdot 10^{-9} \text{ W}\cdot\text{cm}^{-1}/\sqrt{\text{Hz}}$ can be estimated for a bias resistor of 10 M Ω . A further improvement of a 1.4 factor can be calculated when a bias resistor of 100 M Ω is employed, leading to a NNEA of $4.1 \cdot 10^{-9} \text{ W}\cdot\text{cm}^{-1}/\sqrt{\text{Hz}}$. Table 3.2 summarizes the NNEA values obtainable for different values of R_L and Δf .

R_L [M Ω]	Δf [Hz]	NNEA [$\text{W}\cdot\text{cm}^{-1}/\sqrt{\text{Hz}}$]
10	0.5	$5.0 \cdot 10^{-9}$ [63]
100	0.5	$4.4 \cdot 10^{-9}$
10	5	$5.8 \cdot 10^{-9}$
100	5	$4.1 \cdot 10^{-9}$

Table 3.2 NNEA for different values of R_L and Δf , calculated starting from the value reported in [63] for the detection of CO₂ in an N₂ mixture.

It is worth noticing that, at a fixed filter bandwidth, increasing R_L leads to an improvement of the NNEA, benefiting the performance of a QEPAS sensor.

3.3.2 Transimpedance amplifier

Let us now discuss the influence of the LIA filter on the output SNR in the transimpedance configuration. As already pointed out in section 2.3.2, the dominant noise contribution comes from R , while the contribution from R_F to the overall SNR tends to increase as R_F decreases.

Figure 3.10 shows the normalized SNR contribution from the intrinsic resistance of the QTF for different values of R_F , at a low-pass filter bandwidth of $f_{3dB} = 0.5$ Hz.

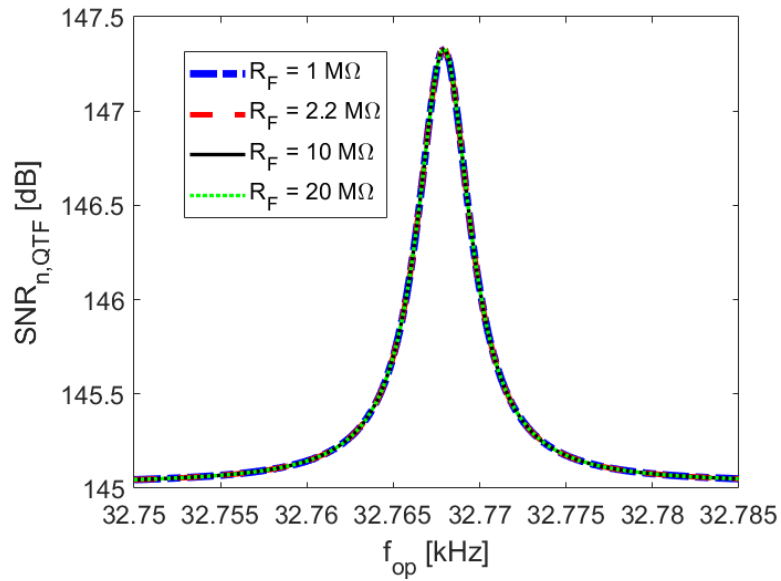


Figure 3.10 Contribution of R to the normalized signal-to-noise ratio for $R_F = 1 \text{ M}\Omega$, $2.2 \text{ M}\Omega$, $10 \text{ M}\Omega$ and $20 \text{ M}\Omega$, at a low-pass filter bandwidth $f_{3dB} = 0.5 \text{ Hz}$.

Since $S_{n,QTF}(j\omega)$ has the same transfer function as the signal, both signal and noise signal show the same dependence on the feedback resistance. As a result, $SNR_{n,QTF}(f_{op})$ is not affected by R_F variations, as shown in Fig. 3.10.

The contribution to the total SNR coming from R_F is displayed in Fig. 3.11.

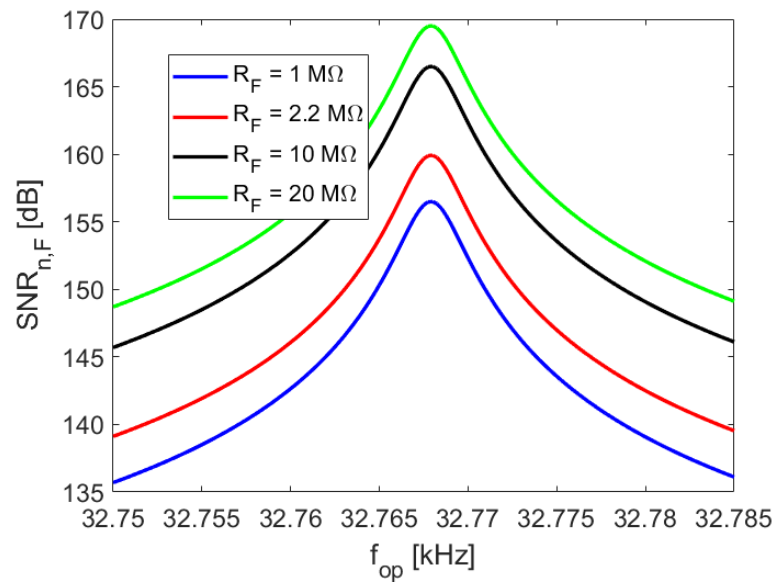


Figure 3.11 Contribution of R_F to the normalized signal-to-noise ratio for $R_F = 1 \text{ M}\Omega$, $2.2 \text{ M}\Omega$, $10 \text{ M}\Omega$ and $20 \text{ M}\Omega$, at a low-pass filter bandwidth $f_{3dB} = 0.5 \text{ Hz}$.

As already discussed in chapter 2, $SNR_{n,F}(f_{op})$ increases as R_F increases (see Eq. 2.35). As long as the stray capacitance C_F is sufficiently low, the feedback resistor can be treated as a white noise source; hence, the LIA output noise $N_{out,F}$ associated to R_F can be easily calculated as the product between $S_{n,F}$ and two times the ENB of the lock-in filter:

$$N_{out,F} = \int_{-\infty}^{+\infty} S_{n,F} \cdot |H_{LIA}(j\omega)|^2 d\omega = 2 \cdot S_{n,F} \cdot ENB \quad (3.17)$$

As a result, $N_{out,F}$ is frequency-independent, and the peak of $SNR_{n,F}(\omega)$ lies in correspondence of the signal peak, namely the series-resonant frequency f_s .

The normalized SNR as a function of the operation frequency at $f_{3dB} = 0.5 \text{ Hz}$ is shown in Fig. 3.12, for different values of R_F .

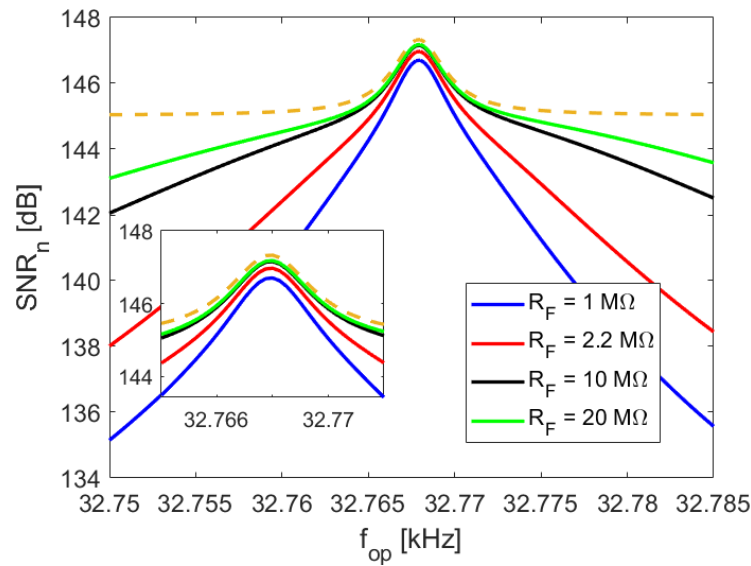


Figure 3.12 Normalized SNR as a function of the operative frequency for $R_F = 1 \text{ M}\Omega$, $2.2 \text{ M}\Omega$, $10 \text{ M}\Omega$, $20 \text{ M}\Omega$, at a low-pass filter bandwidth $f_{3dB} = 0.5 \text{ Hz}$. The dashed golden line represents the $SNR_{n,QTF}$ contribution from the intrinsic resistance of the QTF.

The integration of the total noise spectral density in a narrow-bandwidth results in a

smooth peak of the SNR around f_S . Furthermore, the curve sides become sharper as R_F decreases, as a consequence of the contribution of $SNR_{n,F}$ on the overall signal-to-noise ratio. On the other hand, if R_F increases, $SNR_{n,F}$ becomes less relevant and SNR_n can be approximated to $SNR_{n,QTF}$ in a close interval around f_S , as shown in the inset of Fig. 3.12. However, the peak of SNR_n always lies in correspondence of f_S , regardless of the value of the feedback resistance.

Let us now analyze the influence of a larger integration bandwidth on the output SNR of the LIA. Figures 3.13a and 3.13b plot the contributions of $S_{n,F}(\omega)$ and $S_{n,QTF}$ to the total SNR, respectively, at a low-pass filter bandwidth of $f_{3dB} = 5$ Hz.

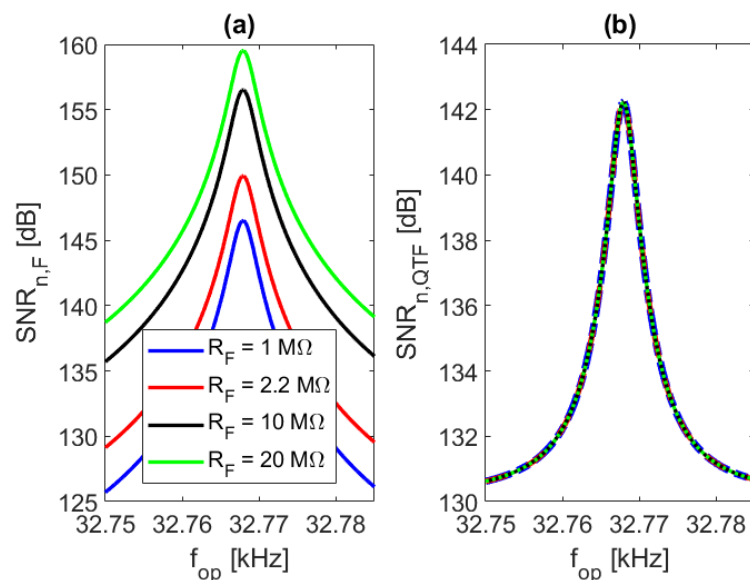


Figure 3.13 Contribution of the feedback resistor (a) and of the intrinsic resistance of the QTF (b) to the normalized SNR, for $R_F = 1 \text{ M}\Omega$, $2.2 \text{ M}\Omega$, $10 \text{ M}\Omega$ and $20 \text{ M}\Omega$, at a low-pass filter bandwidth of $f_{3dB} = 5$ Hz.

$SNR_{n,F}$ still increases as R_F increases, while $SNR_{n,QTF}$ is R_F -independent. The main difference with respect to the narrow-bandwidth configuration is that the peak values of the SNR contribution are slightly lower, as can be deduced comparing Figs. 3.13a and 3.13b with Figs. 3.10 and 3.11, respectively. The resulting normalized SNR is plotted in Fig. 3.14.

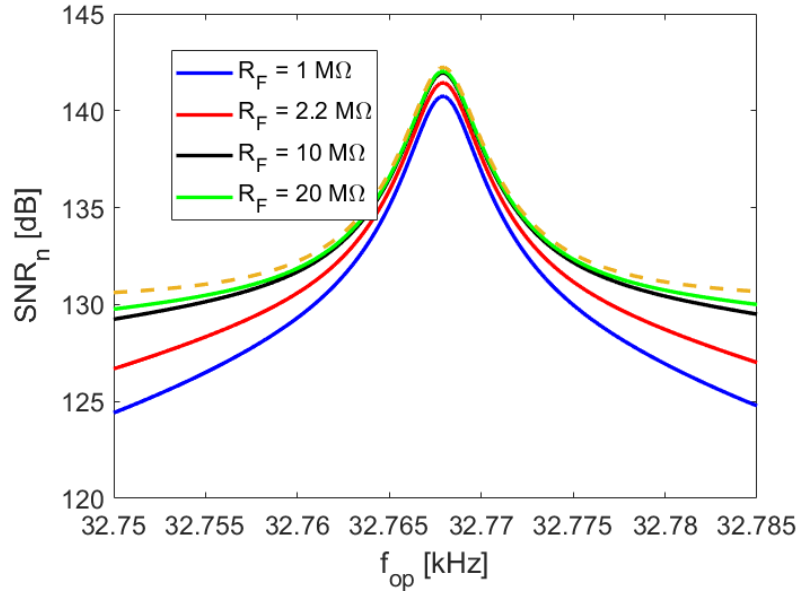


Figure 3.14 Normalized SNR as a function of the operative frequency for $R_F = 1 \text{ M}\Omega$, $2.2 \text{ M}\Omega$, $10 \text{ M}\Omega$, $20 \text{ M}\Omega$, at a low-pass filter bandwidth $f_{3dB} = 5 \text{ Hz}$. The dashed golden line represents the $SNR_{n,QTF}$ contribution from the intrinsic resistance of the QTF.

The peak of $SNR_{n,QTF}$ function is at f_S and its value is 142.2 dB, which is 5 dB lower than the value obtained with $f_{3dB} = 0.5 \text{ Hz}$. Moreover, as a consequence of the integration of the noise contributions in a wider bandwidth, the total SNR is sharper around f_S , and can be well approximated to $SNR_{n,QTF}$ in a wider range around f_S , for $R_F > 10 \text{ M}\Omega$.

Thus, the peak values of the SNR obtained in the TIA configuration correspond to the ones obtained in the voltage configuration, namely, 147.2 dB for $f_{3dB} = 0.5 \text{ Hz}$ and 142.2 dB for $f_{3dB} = 5 \text{ Hz}$. Nevertheless, unlike the voltage configuration, in the transimpedance amplifier neither the filter bandwidth nor the feedback resistor affects the position of the peak of the output signal-to-noise ratio. For this reason, it is always convenient to work at the series-resonant frequency of the QTF in order to optimize the performances of the AFE. In summary, with a fixed lock-in filter bandwidth, a proper choice of the feedback resistor is crucial to maximize the SNR. Conversely, if R_F is fixed, the low-pass filter bandwidth will affect both the output SNR and signal acquisition time.

To clarify, Figure 3.15 shows the trend of the main noise contributions in correspondence of f_S , as a function of the 3 dB bandwidth of the lock-in filter, for different values of R_F .

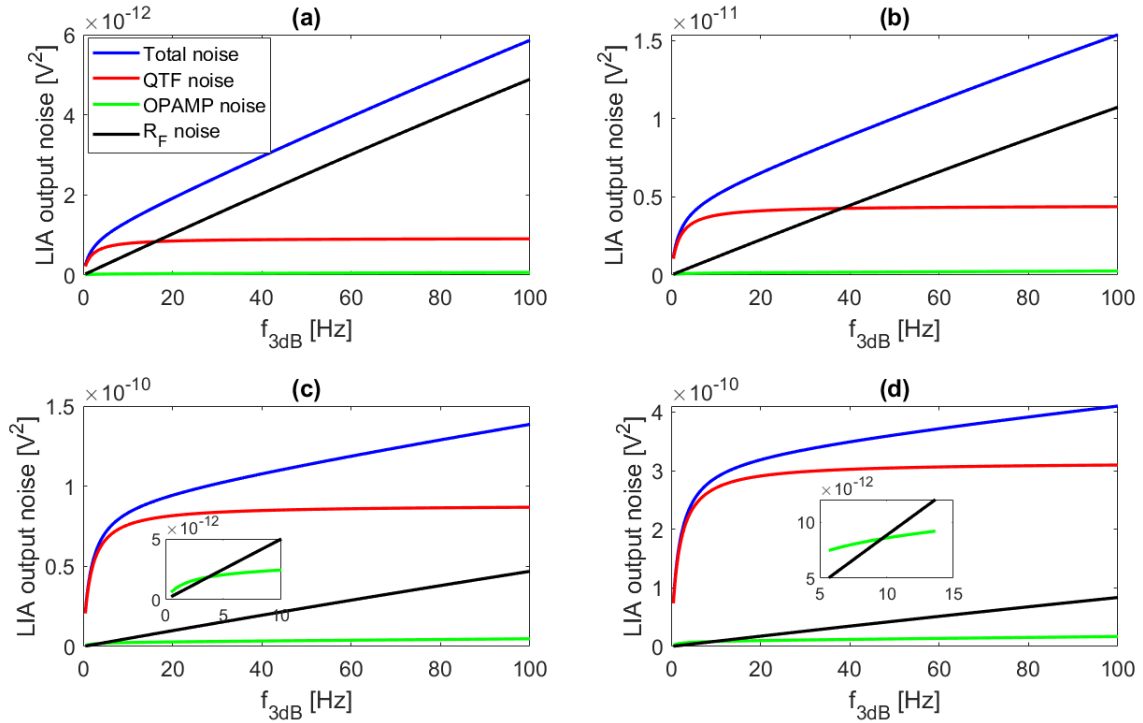


Figure 3.15 Main noise contributions at the series-resonant frequency, as a function of f_{3dB} , for (a) $R_F = 1 \text{ M}\Omega$, (b) $R_F = 2.2 \text{ M}\Omega$, (c) $R_F = 10 \text{ M}\Omega$, (d) $R_F = 20 \text{ M}\Omega$.

Being the C_F impedance negligible, $N_{out,F}$ increases linearly with f_{3dB} , whereas $N_{out,QTF}$ saturates to a constant value as long as f_{3dB} increases. Moreover, for low values of f_{3dB} , the QTF represents the main noise contribution. As f_{3dB} increases, depending on R_F value, the contribution from the feedback resistor becomes more relevant. As an example, $N_{out,F}$ becomes the highest noise contribution:

- (i) for $f_{3dB} > 16 \text{ Hz}$ when $R_F = 1 \text{ M}\Omega$ (Fig. 3.15a)
- (ii) for $f_{3dB} > 38 \text{ Hz}$ when $R_F = 2.2 \text{ M}\Omega$ (Fig. 3.15b)
- (iii) beyond 100 Hz when $R_F \geq 10 \text{ M}\Omega$ (Fig. 3.15c,d).

In addition, the noise contribution from the OPAMP becomes relevant for $R_F \geq 10 \text{ M}\Omega$ and low values of f_{3dB} , as shown in the insets of Fig. 3.15. However, both $N_{out,F}$ and

$N_{out,OP}$ are much lower than $N_{out,QTF}$ when R_F is sufficiently high, therefore it can be neglected [80].

The resulting SNRs as a function of f_{3dB} for different values of R_F are shown in Fig. 3.16.

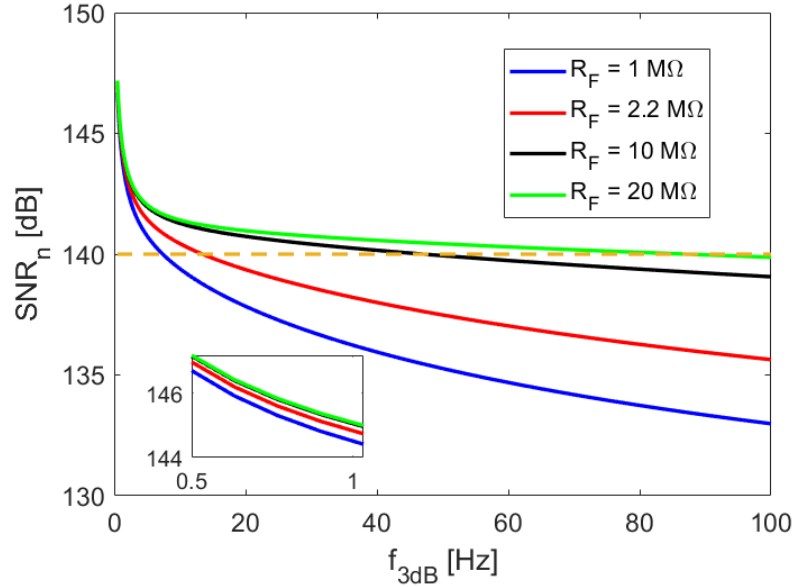


Figure 3.16 Normalized signal-to-noise ratio at f_S as a function of f_{3dB} , for $R_F = 1 \text{ M}\Omega$, $2.2 \text{ M}\Omega$, $10 \text{ M}\Omega$, $20 \text{ M}\Omega$. Dashed golden line identifies a representative value of $SNR_n = 140 \text{ dB}$.

For $f_{3dB} < 1 \text{ Hz}$, the total SNR is not significantly affected by R_F variations, as the dominant noise contribution is $N_{out,QTF}$, and $SNR_{n,QTF}$ is independent from the feedback resistance (see Fig. 3.10). For $f_{3dB} > 1 \text{ Hz}$, the curves start to deviate from the representative value of $SNR_n = 140 \text{ dB}$; in particular, the lower R_F , the more rapidly the SNR deviates (see the blue and red curves in Fig. 3.16). This is due to the noise contribution from R_F , which is more relevant when R_F is lower, as already discussed.

As R_F increases, the weight of $SNR_{n,F}$ on the total SNR is lower, therefore the SNR curves slightly deviate from the representative value of $SNR_n = 140 \text{ dB}$ (see the black and green curves in Fig. 3.16). This suggests that if R_F is sufficiently high, namely $R_F \geq 10 \text{ M}\Omega$, the SNR does not benefit from the reduction of the lock-in filter bandwidth. Consequently, a lower filter time constant (namely, a higher 3dB frequency)

can be employed to speed up the acquisition time, without impacting significantly on the total SNR.

Table 3.3 lists the values of a first order lock-in filter bandwidth to be used to achieve a reference SNR_n of 140 dB (the dashed golden line in Fig. 3.16), together with the corresponding values of time constant and 95% settling time, for different values of R_F .

SNR	R_F	f_{3dB}	τ	$t_{settle,95\%}$
140 dB	1 M Ω	7.4 Hz	21.5 ms	64.5 ms
	2.2 M Ω	13.4 Hz	11.9 ms	35.7 ms
	10 M Ω	47.1 Hz	3.4 ms	10.2 ms
	20 M Ω	87.1 Hz	1.8 ms	5.4 ms

Table 3.3 Values of 3dB lock-in filter bandwidth (f_{3dB}), time constant (τ), 95% settling time ($t_{settle,95\%}$) corresponding to a reference $SNR_n = 140$ dB, for different values of R_F .

Comparable SNR values can be achieved with a lower time constant by increasing the value of the feedback resistance. As an example, a 10 M Ω feedback resistor and a 3.4 ms time constant ensure the same SNR as a 1 M Ω feedback resistor and a 21.5 ms time constant, thus reducing the acquisition time by a factor of 6.3. Increasing R_F beyond 20 M Ω is not convenient: the amplifier gain would lead to saturation of the SNR, and the acquisition time would not benefit anymore from an increase of R_F .

3.3.3 Charge sensitive amplifier

The same method used to study the SNR in the TIA configuration can be used for CSA configuration as well. The main difference between the two configurations is that R_F and C_F are higher in CSA. Hence, since $SNR_{n,F}$ increases with R_F , the noise contribution coming from R_F is negligible. The dominant noise contribution comes from the intrinsic resistance of the QTF, as previously discussed.

Figures 3.17a and 3.17b shows $SNR_{n,QTF}$ and $SNR_{n,F}$ contributions in the CSA configuration, at a first order low-pass filter bandwidth of $f_{3dB} = 0.5$ Hz, for different values of C_F . $R_F = 100$ M Ω was considered in the following simulations to fulfill the

condition $1/\omega C_F \ll R_F$.

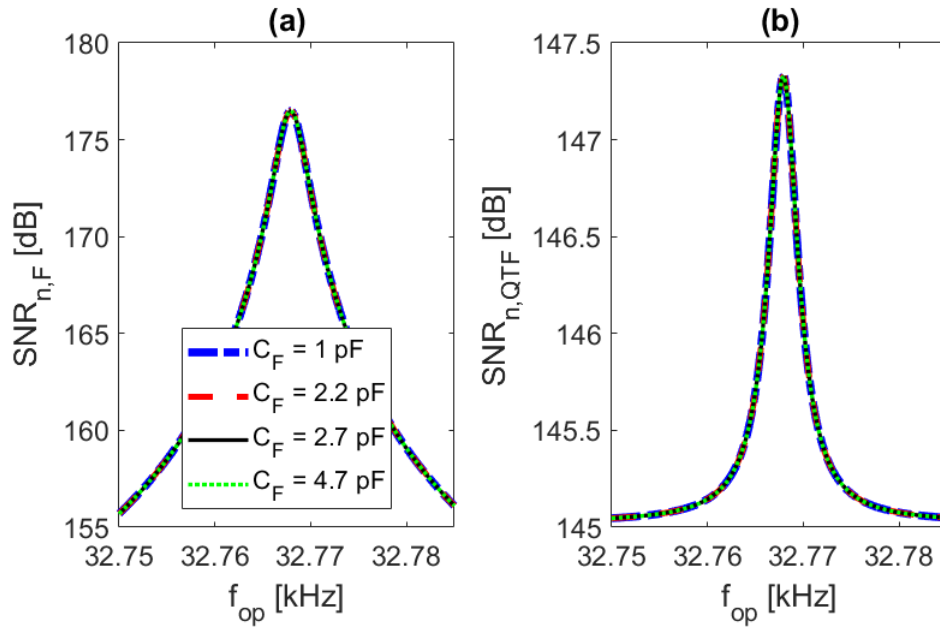


Figure 3.17 Contributions to the normalized SNR from (a) the feedback resistor R_F , and (b) the QTF intrinsic resistance R , for $C_F = 1$ pF, 2.2 pF, 2.7 pF, 4.7 pF, at a first order low-pass filter bandwidth of $f_{3dB} = 0.5$ Hz.

With a fixed value of R_F , $SNR_{n,F}$ is independent of C_F ; furthermore, as previously observed in the TIA configuration, $SNR_{n,QTF}$ does not show any dependency on the gain parameter, namely the feedback capacitance of the CSA.

Figure 3.18 shows the SNR contribution from the operational amplifier, at $f_{3dB} = 0.5$ Hz.

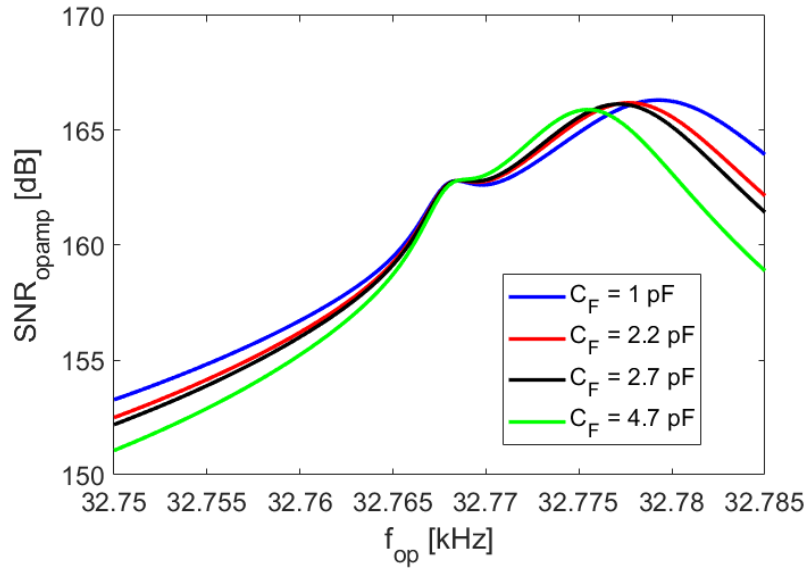


Figure 3.18 Signal-to-noise contribution from the OPAMP for $C_F = 1$ pF, 2.2 pF, 2.7 pF, 4.7 pF, at a first order low-pass filter bandwidth of $f_{3dB} = 0.5$ Hz.

SNR_{opamp} shows a small peak of about 162.7 dB at f_s , and a higher peak around f_p , which slightly increases and moves towards higher frequency values as C_F decreases. This because the output spectral noise density associated to the OPAMP noise is characterized by a local minimum around the parallel resonance frequency, as shown in Fig. 3.19.

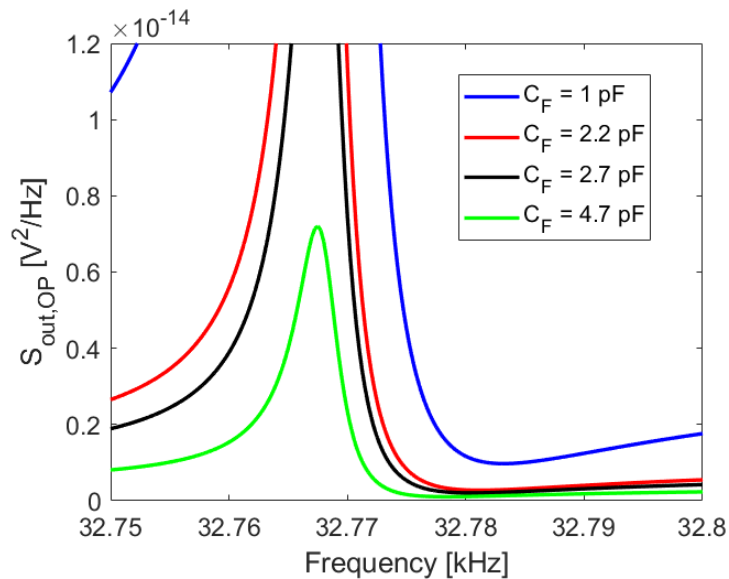


Figure 3.19 OPAMP output noise spectral density as a function of the frequency, for $C_F = 1$ pF, 2.2 pF, 2.7 pF, 4.7 pF.

When the integration bandwidth is as narrow as 0.5 Hz, the second peak of SNR_{opamp} is clearly distinguishable. However, since its value is much higher with respect to $SNR_{n,QTF}$, it can be neglected (see Eq. 3.14).

The total output SNR for $f_{3dB} = 0.5$ Hz is showed in Fig. 3.20.

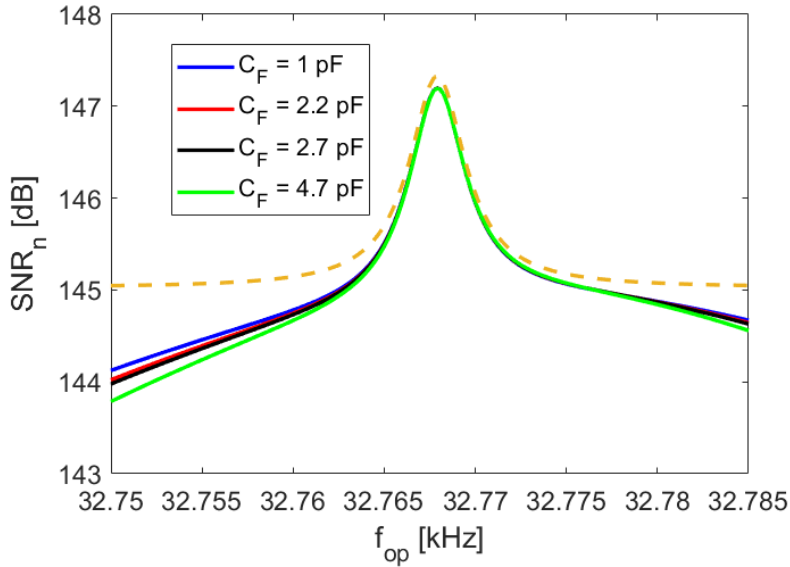


Figure 3.20 Normalized SNR as a function of the operative frequency for $C_F = 1$ pF, 2.2 pF, 2.7 pF, 4.7 pF, at a low-pass filter bandwidth $f_{3dB} = 0.5$ Hz. The dashed golden line represents the $SNR_{n,QTF}$ contribution from the intrinsic resistance of the QTF.

The slight asymmetry in the curves is due to the asymmetric OPAMP output noise spectral density (see Fig. 3.19). In addition, the peak of SNR_n falls at f_s , and its value is about 147.2 dB, which corresponds to the value already found in the voltage and TIA configurations. Moreover, this value is not influenced by the feedback capacitance C_F , as all curves are strongly overlapped in correspondence of $f_{op} = f_s$.

This analysis can be also extended for a LPF bandwidth of $f_{3dB} = 5$ Hz, in order to investigate the effect of a wider integration bandwidth on the output SNR. The integration bandwidth affects $SNR_{n,QTF}$ and $SNR_{n,F}$ only for a decreased value of the

peak: the peak of $SNR_{n,QTF}$ is about 142.2 dB, while the peak of $SNR_{n,F}$ is about 166.5 dB. Figure 3.21 depicts the $SNR_{n,OPAMP}$ contribution to the total SNR, for different values of C_F .

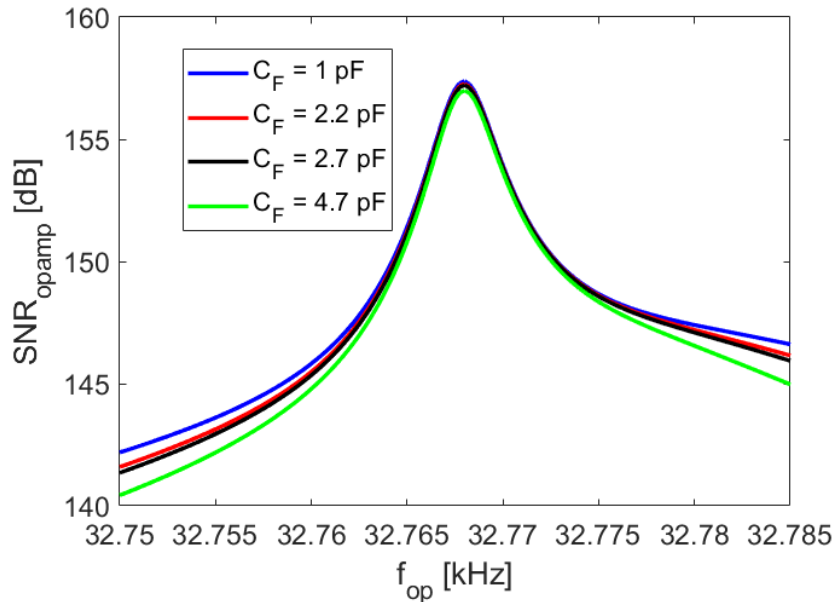


Figure 3.21 Signal-to-noise ratio contribution from the OPAMP for $C_F = 1$ pF, 2.2 pF, 2.7 pF, 4.7 pF, at a first order low-pass filter bandwidth of $BW = 5$ Hz.

The effect of a wider integration bandwidth leads to the disappearance of the peak feature around f_p , observed in Fig. 3.18: the peak feature at f_s is the only one still present. As a result, the total output SNR at $f_{3dB} = 5$ Hz is shown in Fig. 3.22.

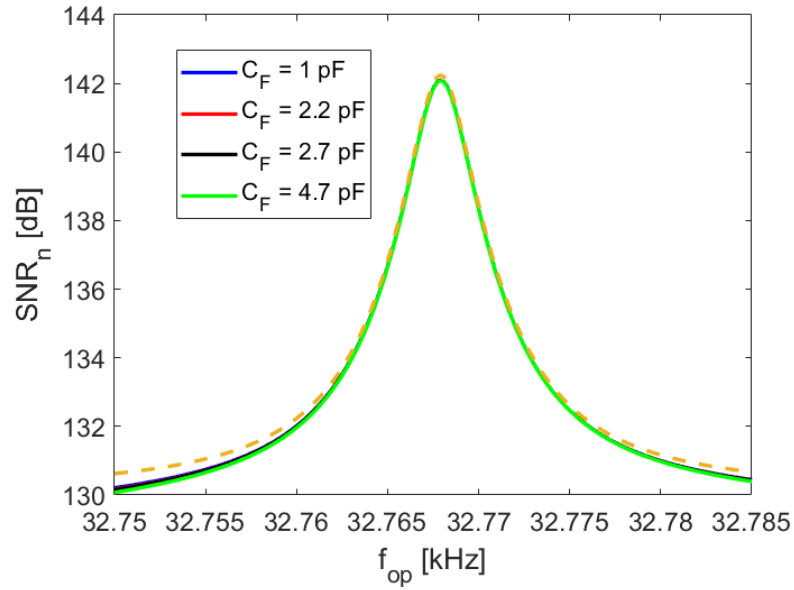


Figure 3.22 Total SNR as a function of the operative frequency for $C_F = 1$ pF, 2.2 pF, 2.7 pF, 4.7 pF, at a low-pass filter bandwidth $f_{3dB} = 5$ Hz. The dashed golden line represents the $SNR_{n,QTF}$ contribution from the intrinsic resistance of the QTF.

The asymmetry observed for a 0.5 Hz bandwidth is strongly reduced, and the SNR can be more accurately approximated to the $SNR_{n,QTF}$ contribution (the dashed golden line in Fig. 3.22), regardless of the value of C_F . Moreover, the SNR peak lies at f_S and its value is about 142.2 dB, as the one already observed in the voltage and TIA configurations.

Let us now examine the trend of the main noise contributions as a function of the integration bandwidth, in correspondence of the series-resonant frequency f_S , for different values of C_F (Fig. 3.23).

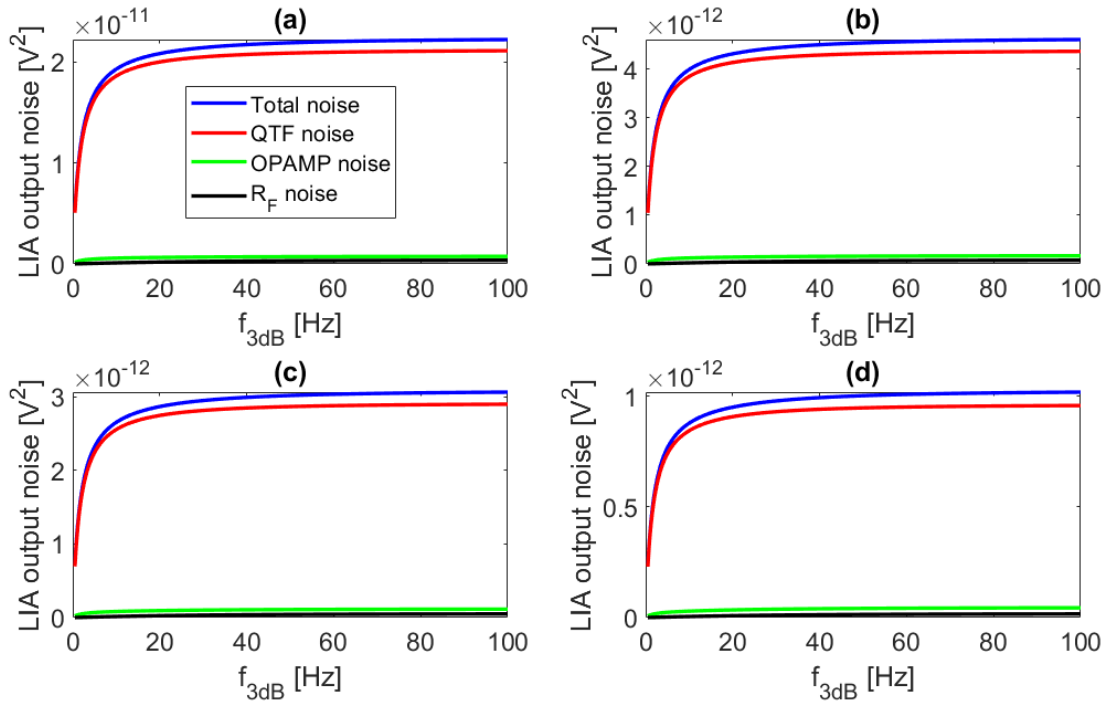


Figure 3.23 Noise contributions at the output of the LIA as a function of the integration bandwidth, at the series-resonant frequency f_S , for (a) $C_F = 1$ pF, (b) $C_F = 2.2$ pF, (c) $C_F = 2.7$ pF, (d) $C_F = 4.7$ pF.

Unlike the TIA configuration, the contribution from R_F is always negligible with respect to the QTF intrinsic noise. Consequently, the total output noise voltage is almost constant as f_{3dB} increases. The normalized SNR at f_S as a function of f_{3dB} is displayed in Fig. 3.24.

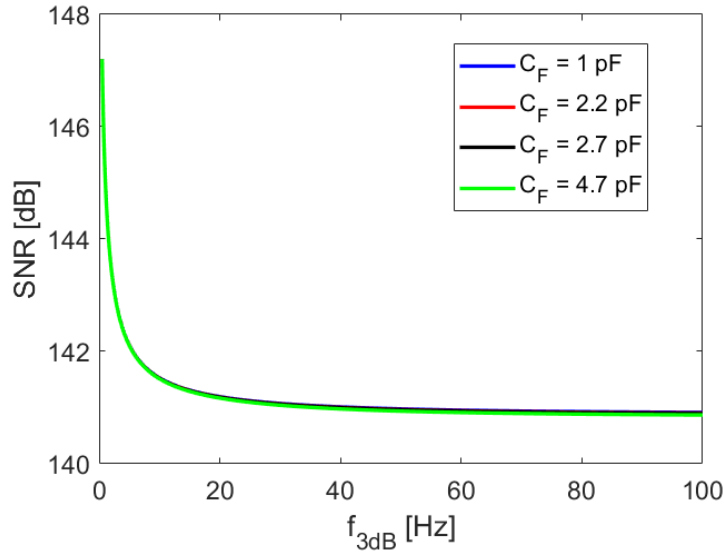


Figure 3.24 Normalized signal-to-noise ratio at f_S as a function of f_{3dB} , for $C_F = 1$ pF, 2.2 pF, 2.7 pF, 4.7 pF.

Because of the trends of the noise contributions, the SNR tends to sharply decrease as f_{3dB} increases up to 5 Hz. Then, for higher values of f_{3dB} , the total output noise is almost constant, and the SNR curves become flat. The value of C_F does not influence the SNR trend; therefore the signal acquisition time is expected not to be affected by the choice of the feedback capacitor.

3.3.4 Comparison among different configurations

In conclusion, in this chapter the influence of the LIA time constant on the output signal-to-noise ratio in the three preamplifier configurations has been investigated. In the voltage configuration, the output SNR is strongly dependent both on the operating frequency and on the bias resistor R_L . The peak value of the SNR tends to increase along with the bias resistor R_L . When a narrowband low-pass filter of the LIA is employed (e.g., bandwidth of 0.5 Hz), the analysis suggests that only a slight increase of the SNR can be obtained by either increasing the value of the resistor R_L or varying the operation frequency. For $R_L < 10$ M Ω , the best operation frequency for the QEPAS technique is the series-resonant frequency of the QTF f_S , where SNR function exhibits a peak value.

This peak becomes less pronounced when R_L increases. A 10 M Ω bias resistor leads to a 1.3 times higher SNR at the series-resonant frequency f_S , with respect to a 100 k Ω bias resistor.

For large values of R_L , SNR tends to be flat around f_S and a small peak emerges at the parallel-resonant frequency f_P . Increasing the value of R_L up to 100 M Ω leads to a further increase of the SNR peak by a factor of 1.4. Thus, for large values of R_L , the choice of the optimal operation frequency is not critical, in case of a narrow-band LIA filter. When a wider LPF bandwidth of the LIA is employed (e.g., bandwidth of 5 Hz), the SNR peak as a function of the operating frequency is still placed at f_S for small values of R_L , as in the case of narrow-band filter (see Fig. 3.9). For large values of R_L , the SNR peak at f_P tends to be sharper as compared to the case of narrow-band LIA filter, thus the operating frequency for the QEPAS technique must be chosen as close as possible to f_P to maximize SNR. As an example, for $R_L = 100$ M Ω , the SNR peak is 1.4 times higher with respect to $R_L = 10$ M Ω .

In the TIA configuration, the peak of the SNR lies at the series-resonant frequency f_S , regardless of the value of the feedback resistance R_F . In addition, when the integration bandwidth is sufficiently low, the dominant noise contribution to the total SNR comes from R . As an example, for $R_F = 1$ M Ω , $SNR_{n,QTF}$ is the most relevant contribution for $f_{3dB} < 16$ Hz. On the other hand, when faster measurements are needed, and a wider integration bandwidth is employed, the noise contribution from R_F becomes dominant, and the total output noise increases linearly with the integration bandwidth (see Fig. 3.15). However, with $R_F \geq 10$ M Ω , the influence of the feedback resistor noise on the LIA output noise voltage drastically reduces, thus allowing lower time constants without affecting the SNR. For instance, a normalized SNR of 140 dB can be obtained by increasing the feedback resistance from 1 M Ω to 10 M Ω and lowering the time constant from 21.5 ms to 3.4 ms, thus shortening the settling time of the output signal by a 6.3 factor.

Finally, in the CSA configuration, the SNR peak falls at f_S , and it is not influenced by the gain parameter of the amplifier, namely, the feedback capacitance C_F . Therefore, when $f_{op} = f_S$, for an integration bandwidth of $f_{3dB} > 30$ Hz (see Fig. 3.24),

the SNR remains almost constant.

It is worth noticing that the peak value of the SNR is identical in the three configurations, namely, 147.2 dB for $f_{3dB} = 0.5$ Hz and 142.2 dB for $f_{3dB} = 5$ Hz. However, in the voltage configuration, for large values of R_L , the SNR peak is close to the parallel-resonant frequency f_P , which depends on the input capacitance of the OPAMP, so it is not an intrinsic property of the sensitive element. Thus, suitable techniques must be used to measure f_P in presence of C_{in} to exploit large values of R_L , increase SNR, especially when short acquisition times are needed. Moreover, the value of R_L cannot be made too large, since the input bias current of the OPAMP would cause undesirable input offset levels. When a lower integration time is needed, the SNR in the TIA configuration is less sensitive to variations of the feedback resistance when $R_F \geq 10$ M Ω , whereas, in the CSA, the SNR does not depend on the value of the feedback capacitance C_F .

For these reasons, employing a TIA or a CSA as QTF front-end amplifier allows a higher reliability with respect to a voltage amplifier, ensuring the comparable performances in terms of SNR and acquisition time.

Chapter 4: Results

4.1 QEPAS sensor

The influence of air pressure on the resonance properties of a bare T-shaped QTF and of the same QTF acoustically coupled with two resonator tubes was analyzed. A theoretical model was developed to predict the influence of air pressure both on the frequency and quality factor of the fundamental resonance mode of the QTF. The model was validated with experimental results. Furthermore, the QTF was assembled in a spectrophone with two resonator tubes. The influence of resonator tubes on the spectrophone resonance properties was investigated and compared with those of the bare QTF. The same analysis was performed considering two different distances of the tubes from the QTF.

4.1.1 Experimental setup

The electrical characterization of the QTF is useful to retrieve its resonance frequency and quality factor, as an alternative to the use of an impedance analyzer, that will be discussed in section 4.2. The experimental apparatus used to electrically excite the QTF is sketched in Fig. 4.1a. The analog output of a data acquisition (DAQ) card (NI USB-6008) was used as a waveform generator to provide a sinusoidal electrical excitation for the QTF. The QTF was excited at its fundamental in-plane flexural mode. A LabVIEW-based software was used to vary the excitation frequency step-by-step around resonance, with a peak-to-peak amplitude fixed to 0.5 mV. The piezoelectric current was converted into a voltage signal by a transimpedance amplifier and acquired via DAQ card through LabVIEW-based software, which allowed retrieval of the QTF signal at the excitation frequency. The QTF was placed in a stainless-housing (SSH) with an inlet and outlet to pump ambient air. Air passed through a needle valve (NV1 in Fig. 4.1a), the SSH, a second needle valve (NV2) and a vacuum pump. The valves were used to regulate the pressure inside the SSH.

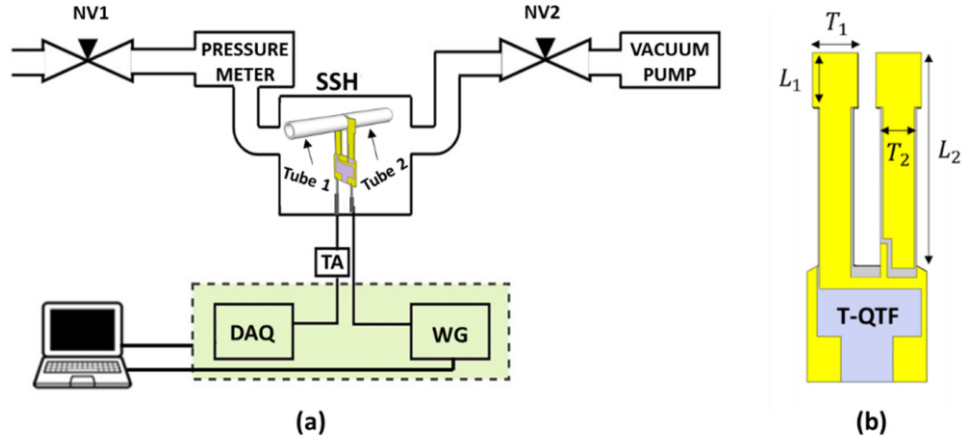


Figure 4.1 (a) Experimental apparatus: SSH—stainless-steel housing; NV1—needle valve 1; NV2—needle valve 2; TA—transimpedance amplifier; DAQ—data acquisition card; WG—waveform generator. (b) Sketch of T-shaped QTF.

The pressure value was measured using a digital pressure meter (DIGITRON 2025P). A pressure range from 10 Torr to 760 Torr was investigated. These measurements were repeated in three different configurations. Firstly, a bare T-shaped QTF was used. Then, a cylindrical V-groove (not shown in Fig. 4.1a) was placed around the QTF to hold and fix two resonator tubes. The two tubes were mounted on both sides of the QTF (see Fig. 4.1a) at a distance of $d = 200 \mu\text{m}$, perpendicular to the QTF plane with the tube center 2 mm below the QTF top [81]. Lastly, the distance of $200 \mu\text{m}$ was halved. A sketch of the T-QTF is reported in Fig. 4.1b. The geometrical parameters of the T-QTF and the tubes are summarized in Tab. 4.1.

	L_1	L_2	T_1	T_2	w
T-QTF	2.4	9.4	2.0	1.4	0.25
	L	OD	ID		
Tubes	12	1.83	1.59		

Table 4.1 Geometrical parameters of the T-QTF and of resonator tubes. L_1 and T_1 are the length and thickness of the T-shaped part of the QTF, L_2 is the total prong length,

T_2 is the prong thickness, and w is the crystal width. OD and ID are the outer and internal tube diameters, respectively, and L is the tube length. All sizes are in millimeter units.

4.1.2 Measurements of resonance frequency and quality factor

As an example, resonance curves (black datapoints) for the bare T-QTF at two representative pressures, 10 Torr and 760 Torr, are shown in Fig. 4.2a and 4.2b. The QTF signal is normalized and plotted as function of $1 - f^2/f_0^2$.

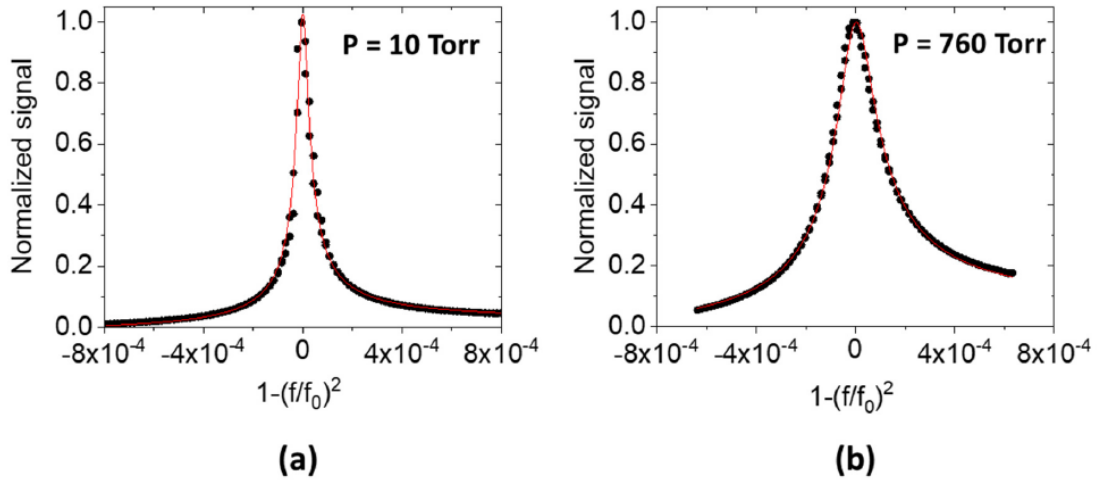


Figure 4.2 Resonance curve (black datapoints) for T-QTF at (a) 10 Torr, and (b) 760 Torr. The solid red line is the best fit of experimental data obtained by using Eq. 4.1.

Taking into account the results obtained in section 1.3, Equation 1.14 is used as fitting function in the form of:

$$V_{out} = A \sqrt{\frac{(1-x)B(C'^2B(1-x) + (C'x + 1)^2)}{x^2 + (1-x)B}} \quad (4.1)$$

where $B = 1/Q^2$ and $x = 1 - f^2/f_0^2$.

The f_0 value corresponding to the peak values is needed for the fitting procedure. Since its value is not modified by the stray capacitance thanks to the virtual ground imposed by the transimpedance amplifier, firstly f_0 can be determined by considering a Lorentzian fit of the measured results. Then, Equation 4.1 can be used for a second iteration fit to estimate the Q -factor. The best fit obtained by using Eq. 4.1, for the

highest (760 Torr) and lowest (10 Torr) pressures at which the bare QTF was investigated, is also shown in Fig. 4.2a and 4.2b (solid red lines). From the preliminary Lorentzian fitting procedures, the resonance frequency f_0 is extracted and plotted as a function of the air pressure, as shown in Fig. 4.3 (datapoints) for the all the three investigated configurations.

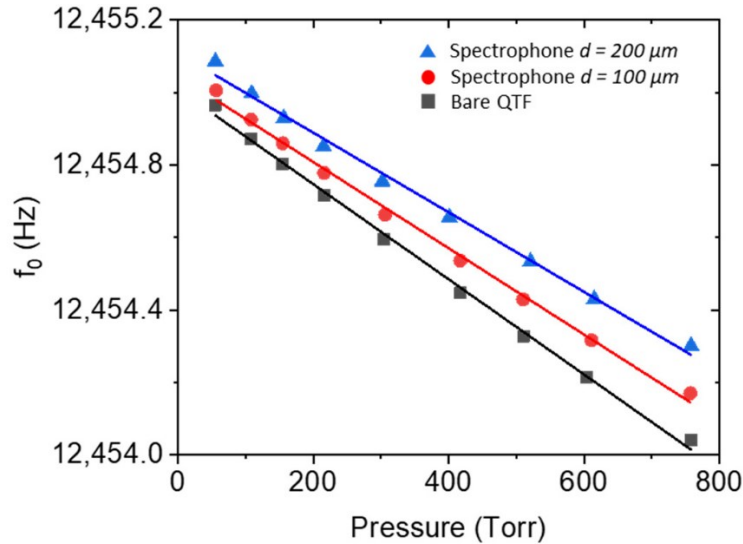


Figure 4.3. Resonance frequency (datapoints) as a function of the pressure in the three configurations. The solid lines are the best linear fits.

As expected from Eq. 1.16, f_0 decreases linearly as pressure increases. The intercept values of linear fits, i.e., the resonance frequencies in vacuum, are different for three configurations. At first glance, this seems not to be in agreement with Eq. 1.16. It is worth noticing that the Euler–Bernoulli equation with viscous drag force term in Eq. 1.15 is valid only when the gas is supposed to be in the viscous regime. Lowering the pressure, the gas can enter the molecular region, where damping mechanisms are caused by independent collisions of non-interacting molecules with the vibrating QTF prong. As a result, at pressures <10 Torr, the additive mass cannot be supposed proportional to the air density and a deviation from the linearity can also be supposed for the QTF resonance frequency. With respect to the bare QTF, the coupling with a pair of resonator tubes causes a shift of spectrophone resonance frequency. Moreover, the frequency shift increases with the pressure, although it is almost constant at

pressures lower than 200 Torr. This can be explained by considering that the tubes and the QTF interact with each other through the medium in SSH at higher pressures. Thus, at low pressure, the QTF–tubes coupling is reduced and the QTF can be considered almost isolated from the tubes. For any pressure values, the frequency shift is larger when $d = 100 \mu\text{m}$ with respect to $d = 200 \mu\text{m}$. This can be explained observing that the QTF–tube distance also affects the resonator’s acoustic interaction, thus leading to a greater frequency shift for a shorter QTF–tube distance. From the linear fits, the intercept value represents the fundamental vibrational mode f'_0 in vacuum whereas the slope is related to additive mass, as described in Eq. 1.16. Indeed, as discussed in section 1.3, the additive mass per unit of length $u = u_0 \cdot P$ is proportional to the gas pressure, where $u_0 = kM/R\theta$ with k in m^2 units. U_0 represents the additive mass per unit of length and pressure, and can be retrieved from the slope m of the linear fit as $m = u_0 f'_0 / (2\rho A)$ where $\rho = 2650 \text{ kg/m}^3$ and the prong section $A = T_2 \cdot w$. The results are listed in Tab. 4.2.

	Bare QTF	Spectrophone $d = 100 \mu\text{m}$	Spectrophone $d = 200 \mu\text{m}$
f'_0 (Hz)	12455.01	12455.05	12455.11
m (Hz/Torr)	$1.31 \cdot 10^{-3}$	$1.19 \cdot 10^{-3}$	$1.10 \cdot 10^{-3}$
u_0 (kg/(m·Torr))	$1.95 \cdot 10^{-10}$	$1.77 \cdot 10^{-10}$	$1.64 \cdot 10^{-10}$

Table 4.2 Parameters retrieved from the linear fits shown in Fig. 4.3. f'_0 is the intercept of the linear fit and represents the fundamental vibrational mode in vacuum; m is the slope of the linear fit; u_0 is the additive mass per unit of length and pressure extracted by the slope.

The bare T-QTF shows a slightly higher value of u_0 with respect to the one obtained when it is coupled with tubes. This could be related to the fact that the presence of the tubes reduces the number of molecules surrounding the QTF which results in a decreasing of the inertia to the prong oscillation. The additional inertia of the vibrating

prong due to the effect of the surrounding medium was modelled as an additive mass. Indeed, with respect to the bare QTF, the reductions in the additive mass results were 8% and 16% for QTF–tube distance $d = 100 \mu\text{m}$ and $d = 200 \mu\text{m}$, respectively.

The quality factor values are extracted by fitting the resonance curves with Eq. 4.1. The Q -factor values (datapoints) are plotted as a function of the air pressure in Fig. 4.4, for the three investigated configurations.

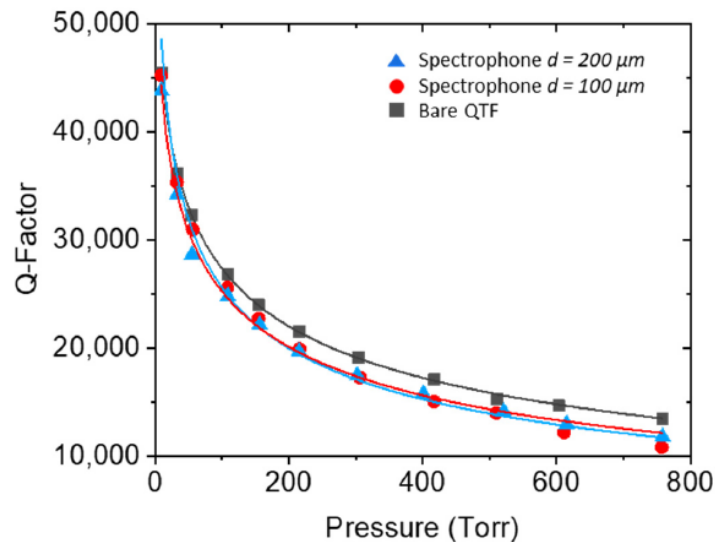


Figure 4.4 Q -factor values as a function of the air pressure (datapoints) for the three investigated configurations. Solid lines are best fits of experimental data by using Eq. 4.3.

The trends show a strong dependence on air pressure, especially at pressures lower than 20 Torr, suggesting that the dominant loss mechanism is air damping. Moreover, working at pressures lower than 100 Torr, the Q -factor dramatically increases as pressure decreases, meaning that air pressure requires a higher efficient stabilization with respect to operating at pressures close to the atmospheric one. Negligible differences are observed when the QTF–tube distance is reduced from 200 μm to 100 μm : if the tube–QTF distance is reduced from 200 μm to 100 μm , the spectrophone Q -factor is almost not affected. This “relaxes” the assembling procedure of the spectrophone, avoiding the requirement of a superfine placement of tubes. This can be explained by noting that the prong spacing (800 μm) is comparable with the tube ID

(see Tab. 4.1); thus, the effective interacting surface can be neglected. Indeed, while prongs are vibrating, they could lose energy via interaction with the tube walls (squeeze damping). If this additional loss mechanism is present, it should be influenced by: (i) the tube–QTF distance: the lower the distance, the higher the contribution; (ii) the air pressure: the higher the pressure, the higher the squeeze damping. Thus, in Fig. 4.4, a squeeze damping effect should result in a deviation at higher pressures of red circles (spectrophone with $d = 100 \mu\text{m}$) towards lower values, with respect to blue triangles (spectrophone with $d = 200 \mu\text{m}$). Conversely, red circles and blue triangles should overlap at lower pressures. Instead, both datasets are quite overlapped in the whole of the investigated pressure range, demonstrating that squeeze damping is negligible. In the whole pressure range, the coupling with tubes leads to a reduction in the spectrophone Q-factor with respect to the bare QTF. This reduction increases as pressure increases and is almost zero at pressures lower than 100 Torr. This behavior can be explained by considering that the effect of the acoustic coupling of the high Q -factor QTF with the low Q -factor tubes, which leads to a QTF loss of energy, is reduced at low pressures, because of the reduced number of surrounding molecules. Indeed, at 10 Torr, the Q -factor of the spectrophone (45454) is comparable with the one measured for the bare QTF (45221). As a result, the surrounding air strongly affects the acoustic coupling of both resonators, namely, the tube and the QTF. It is worth noticing that datapoints in Fig. 4.4 close to atmospheric pressure deviate from fitting with Eq. 4.3. This is expected because Hosaka’s model in Eq. 1.17 was rewritten with the assumption that air density is proportional to pressure. This is valid only if the ideal gas law is assumed. Approaching atmospheric pressure, the ideal gas law is no longer valid, requiring a replacement with the van der Waals equation (real gas law).

As the dissipation mechanisms described in section 1.3 are independent of each other, the overall quality factor can be written as:

$$\frac{1}{Q(P)} = \frac{1}{Q_0} + \frac{1}{Q_{air}(P)} \quad (4.2)$$

where $1/Q_0 = 1/Q_{TED} + 1/Q_{sup}$. Using Eq. 1.17 for Q_{air} , $Q(P)$ can be rewritten as:

$$Q(P) = \frac{1}{C + D\sqrt{P}} \quad (4.3)$$

where:

$$\begin{cases} C = \frac{1}{Q_0} + \frac{3\mu}{4\rho T w f_0} \\ D = \frac{3}{4} \sqrt{\frac{4\pi\mu M}{R\Theta}} \end{cases} \quad (4.4)$$

With this formulation, parameter C takes into account all the pressure-independent loss mechanisms. Equation 4.3 was used to fit the experimental data and the results are shown as solid lines in Fig. 4.4. The obtained fit curves were used to evaluate the difference ΔQ between the Q -factors of the bare QTF and the spectrophone with $d = 200 \mu\text{m}$, as a function of the air pressure. The result is shown in Fig. 4.5.

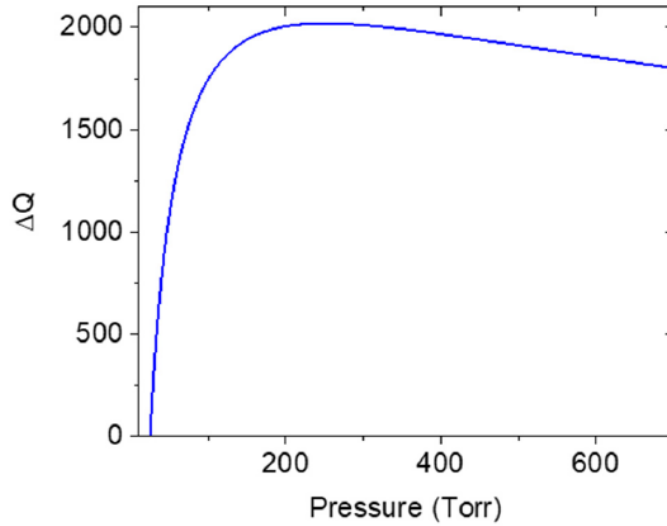


Figure 4.5 ΔQ as a function of the air pressure, where ΔQ is the Q -factor decrease when the QTF is coupled with a pair of resonator tubes at a distance of $200 \mu\text{m}$.

Starting from low pressures, ΔQ quickly increases until it reaches a maximum at around 200 Torr. At $p > 200$ Torr, we can assume that the influence of air on the interaction between tubes and QTF is saturated, leading to an almost flat trend with a slight decrease towards the atmospheric pressure. A reduction of 24% in the Q -factor

of the spectrophone with respect to the bare QTF is observed at atmospheric pressure.

4.2 Extraction of the electrical parameters of a QTF

The Butterworth – Van Dyke model, introduced in section 1.2.2, allows to describe the electrical behavior of a QTF [17,50,82-84] through the intrinsic resistance R , the series capacitance C_s , the inductance L and the parallel capacitance C_p . The estimation of these parameters is very useful to retrieve the resonance frequency and the quality factor of a QTF without employing a preamplifier. The electrical parameters of a QTF can be extracted by measuring the module of the QTF impedance, and then fitting the acquired data.

An impedance analyzer (MFIA from Zurich Instruments) was employed to measure the module and phase of the impedance of a standard 32.7 kHz-QTF at different pressures. To minimize the parasitic effects of the cables, the impedance analyzer was used with a test fixture and the probe was calibrated before starting the measurements. For each pressure, 10 characterization waveforms were acquired. Then, a fitting algorithm (see section A.1) was applied to each waveform in order to extract the parameters of the QTF. Finally, the obtained parameters were averaged. Figures 4.6a and 4.6b show two representative acquisitions obtained at 50 and 700 Torr and the related best fits of the experimental data.

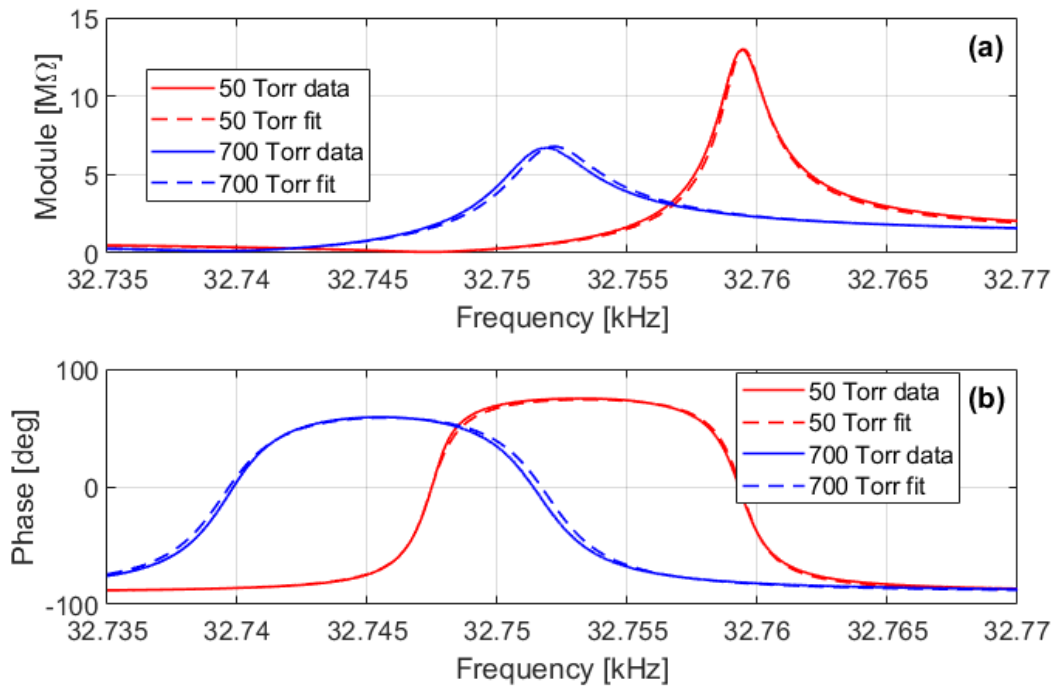


Figure 4.6 Module (4.6a) and phase (4.6b) of the impedance of a standard QTF at 50 and 700 Torr.

Table 4.3 lists the values of the QTF parameters in the investigated pressure range.

Pressure [Torr]	L [H]	C_s [fF]	C_p [pF]	R [kΩ]
50	6021.578	3.923	5.372	63.197
100	6041.807	3.910	5.322	72.356
150	6087.885	3.881	5.653	79.047
250	6065.168	3.895	5.235	91.043
400	6068.501	3.894	5.197	105.842

600	6050.332	3.906	5.170	123.402
700	6039.973	3.913	5.160	130.920

Table 4.3. Values of QTF parameters measured with MFIA in a pressure range between 50 and 700 Torr.

Figure 4.7 depicts the values of quality factor and intrinsic resistance of the 32.7 kHz-QTF as a function of the air pressure.

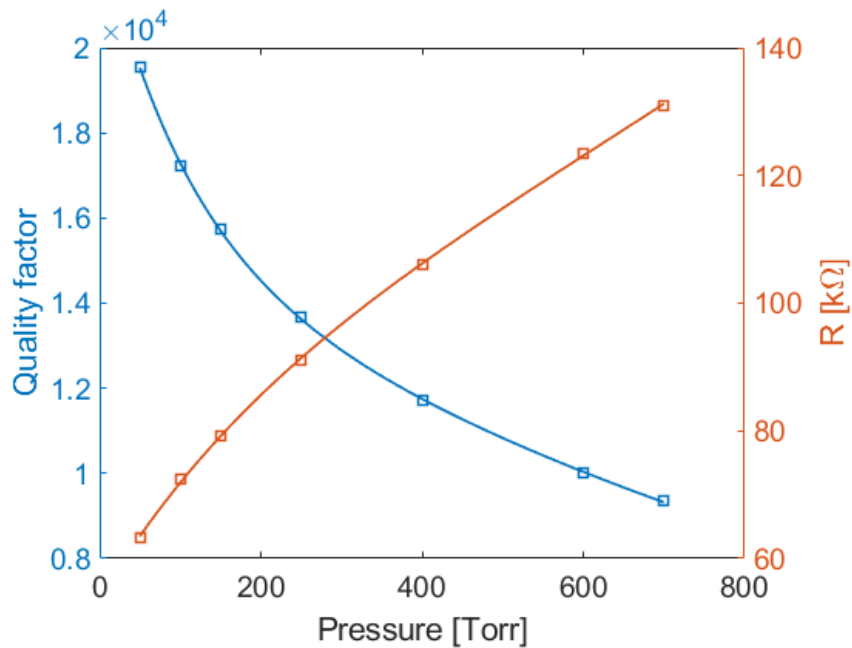


Figure 4.7 Quality factor and intrinsic resistance of a standard QTF (datapoints) versus pressure; solid lines are best fits.

As previously observed, the quality factor decreases exponentially as the pressure increases, while the QTF intrinsic resistance shows the opposite trend, being inversely proportional to the quality factor.

4.3 QEPAS sensor with TIA for QTF readout

4.3.1 Experimental setup

Experimental measurements for measuring the signal to noise ratio (SNR) at the output of the lock – in amplifier employing both a TIA and a CSA were performed. A Printed Circuit Board (PCB) implementing both TIA and CSA configurations was realized (see Fig. 4.8a and 4.8b). Since the two configurations differ only in the feedback network components, it is possible to switch between TIA and CSA by means of a jumper. In the TIA configuration, a 10 M Ω feedback resistor was employed to set the gain of the amplifier. Another jumper can be employed to select the mode of operation, namely QEPAS mode or QTF characterization mode; when the jumper is set on QEPAS mode, the loose end of the QTF is grounded, while during QTF characterization it is connected to the waveform generator. A 6-ways connector was used to connect the PCB to the laboratory instrumentation (power supply, waveform generator and lock-in amplifier). A ± 12 V dual power supply was employed to power on the board, and an RC network was implemented to filter out the high frequency noise components. The operational amplifier mounted on the board is the AD8067, from Analog Devices [70].

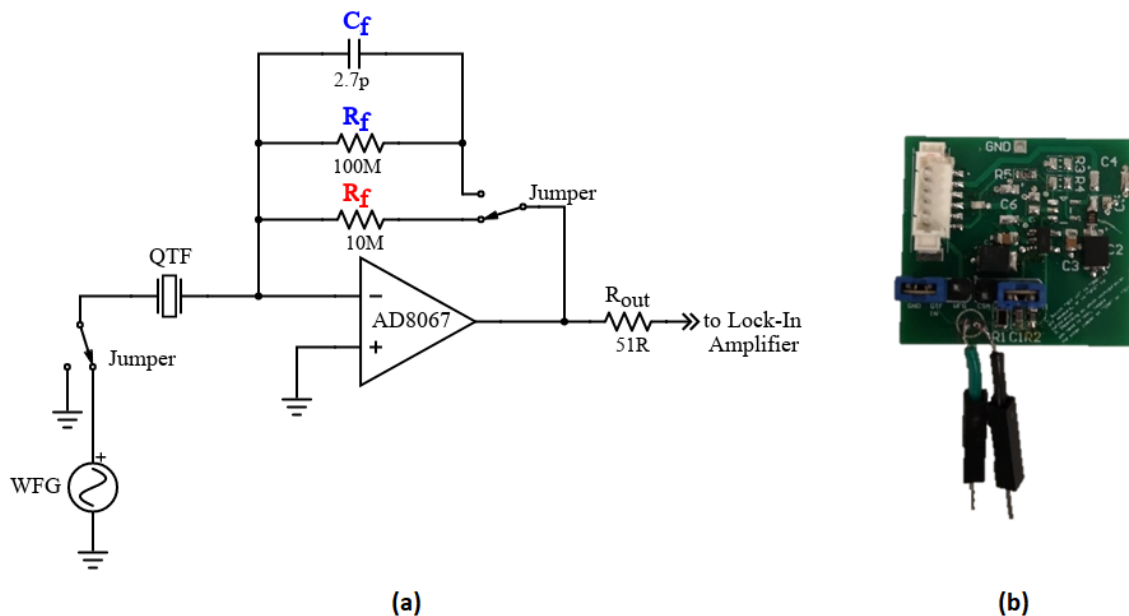


Figure 4.8 (a) Circuit schematic of the preamplifier for QTF readout. The red label refers to the TIA configuration, the blue labels refer to the CSA configuration. WFG – Waveform Generator, QTF – Quartz Tuning Fork. (b) Top view of the Printed Circuit

Board implementing TIA and CSA. Components are placed on the top layer, as the bottom layer is entirely devoted to the ground plane.

The experimental setup employed to perform QEPAS measurements is sketched in Fig. 4.9. A single-mode laser diode (EP1392-5-DM-B01-FM) specifically designed for the detection of H₂O at 1392 nm was employed as light source for the detection of the water vapor in laboratory air. The emission wavelength of laser diode was modulated by means of a current driver with a built-in thermo-electric cooler (Thorlabs CLD1010). A waveform generator (AFG3102 by Tektronix) was employed to dither the laser diode current driver with a sinusoidal modulation signal. The working temperature of the laser was set to 25°C. The laser beam was collimated by a fiber coupled collimator, and then an aspheric lens was employed to focus the laser beam between the prongs of the QTF.

The QTF was encapsulated in an Acoustic Detection Module (ADM). A pressure controller (Alicat Scientific) and a vacuum pump were used to set the working pressure, and an external valve was employed to fix the flow to 30 sccm (Standard Cubic Centimeters per Minute).

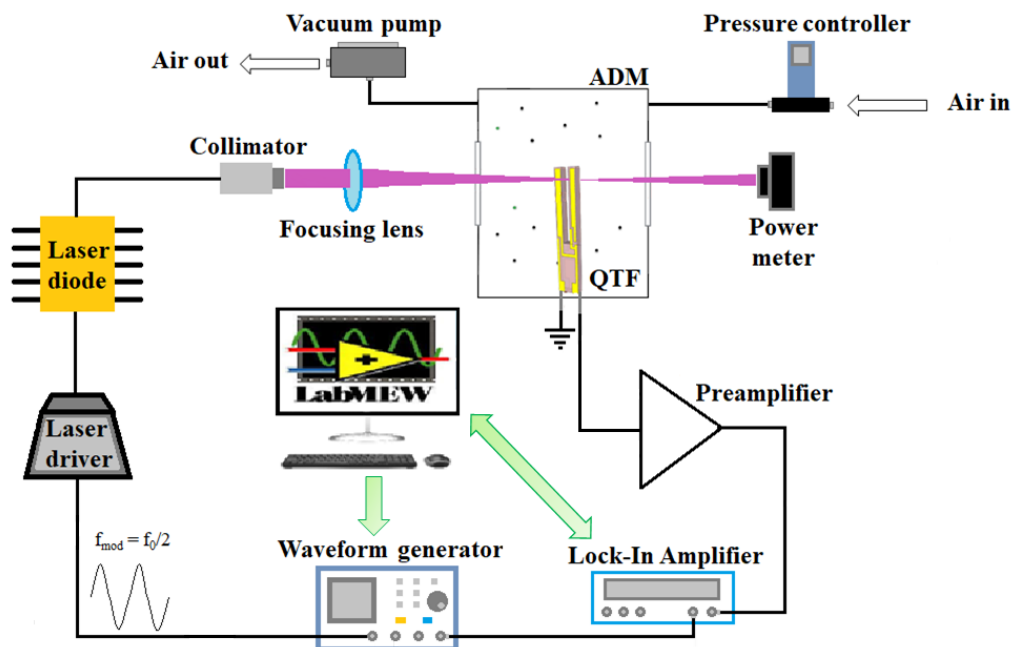


Figure 4.9 Experimental apparatus for QEPAS measurement with a transimpedance amplifier for QTF readout. ADM – Acoustic Detection Module, QTF – Quartz Tuning Fork, f_{mod} – modulation frequency, f_0 – resonance frequency of the quartz tuning fork.

The preamplifier was externally connected to the QTF, and its output pin was connected to a lock-in amplifier (MFIA by Zurich Instruments), whose reference signal input was connected to the TTL output of the waveform generator. The MFIA is a digital LCR meter, which can work either as impedance meter or as lock-in amplifier, therefore it can be directly connected to a personal computer (PC) to collect data. A second order low-pass filter with a 100 ms time constant was used as LIA filter [54], and the signal acquisition time was set to 700 ms. A custom LabVIEW program was realized to easily interface the PC both to the MFIA and the AFG3102. A picture of the experimental setup employed for QEPAS measurements is reported in Fig. 4.10.

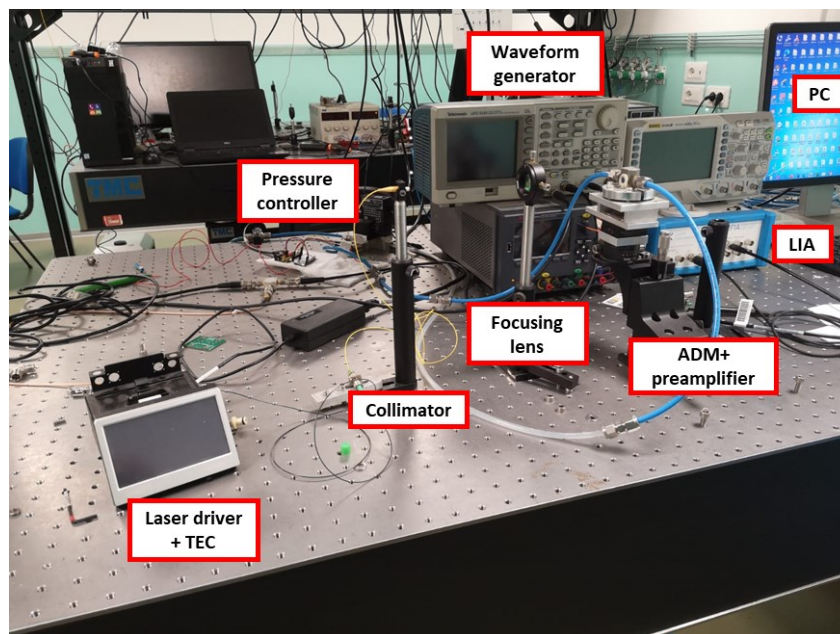


Fig 4.10 Experimental setup for QEPAS measurements employing both a TIA and a CSA as QTF readout electronics.

The environmental water concentration was constantly monitored with the HYT271 sensor by Innovative Sensor Technology (see Fig. 4.11). This sensor allows a reliable measurement of the environmental temperature and humidity, with a ± 0.2 °C

temperature accuracy and a $\pm 1.8\%$ relative humidity accuracy at room temperature.



Figure 4.11 HYT271 sensor. Pinout (from left to right): SDA (serial data), GND (ground), VDD (positive power supply), SCL (serial clock).

The HYT271 is a digital sensor implementing the I²C protocol, hence it can be easily interfaced with any microcontroller supporting this communication protocol.

4.3.2 Signal measurements

The LIV characteristic of the EP1392-5 laser diode (Fig. 4.12) shows that the H₂O absorption occurs at a DC driving current of 101 mA; therefore, this value of current was set on the current driver for the QEPAS measurements.

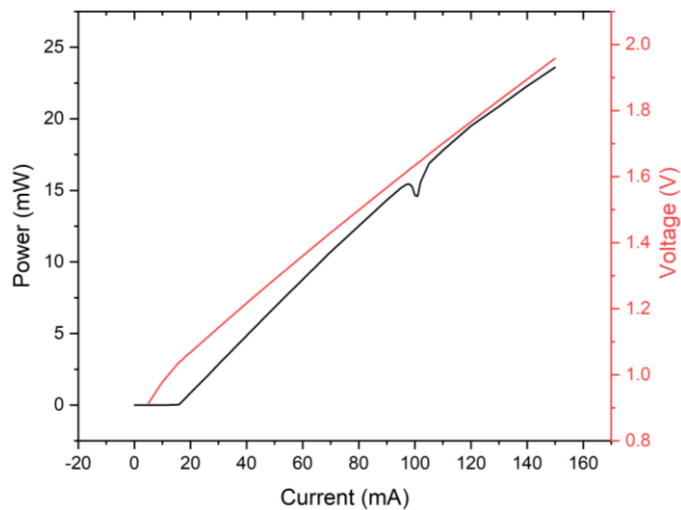


Figure 4.12 LIV characteristic of the EP1392-5 laser diode. The water absorption peak occurs at 101 mA.

The QEPAS sensor operates in wavelength modulation and second harmonic detection ($2f$ - WM): the laser current was modulated half the QTF resonance frequency, while the QTF signal is demodulated at the QTF resonance frequency by the lock – in amplifier. The amplitude of the sinusoidal modulation was optimized to maximize the LIA output signal, for each working pressure. A 10 dB attenuator was connected at the output channel of the waveform generator to provide a modulation amplitude lower than the minimum value allowed by the AFG3102, which is 20 mV peak-to-peak.

Table 4.4 summarizes the values of the modulation frequency and amplitude that maximize the QEPAS signal, for each investigated pressure.

Pressure [Torr]	Modulation amplitude [mVpp]	$f_{mod,peak}$ [Hz]	$f_0/2$ [Hz]
50	9.5	16373.62	16373.71
100	14.2	16373.34	16373.42
150	17.4	16373.10	16373.02
250	25.3	16372.53	16372.53
400	50.6	16371.66	16371.63
600	79.1	16370.50	16370.40
700	85.4	16369.88	16369.72

Table 4.4 Parameters of the modulation signal that maximize the amplitude of the LIA output signal in TIA configuration. $f_{mod,peak}$ is the modulation frequency corresponding to the peak of the output signal, f_0 is the QTF resonance frequency.

As expected, the peak of the QEPAS signal lies nearby the QTF resonance frequency. Figure 4.13 shows LIA output signal as a function of the frequency, at different pressures. The highest output voltage measured at the QTF resonance frequency is 410 μ V at 50 Torr, while the lowest output voltage is 186 μ V at 700 Torr. Indeed, the higher the pressure, the higher the intrinsic resistance of the QTF (as shown

in Table 4.3) and the lower the amplitude of the preamplifier output signal at the resonance frequency.

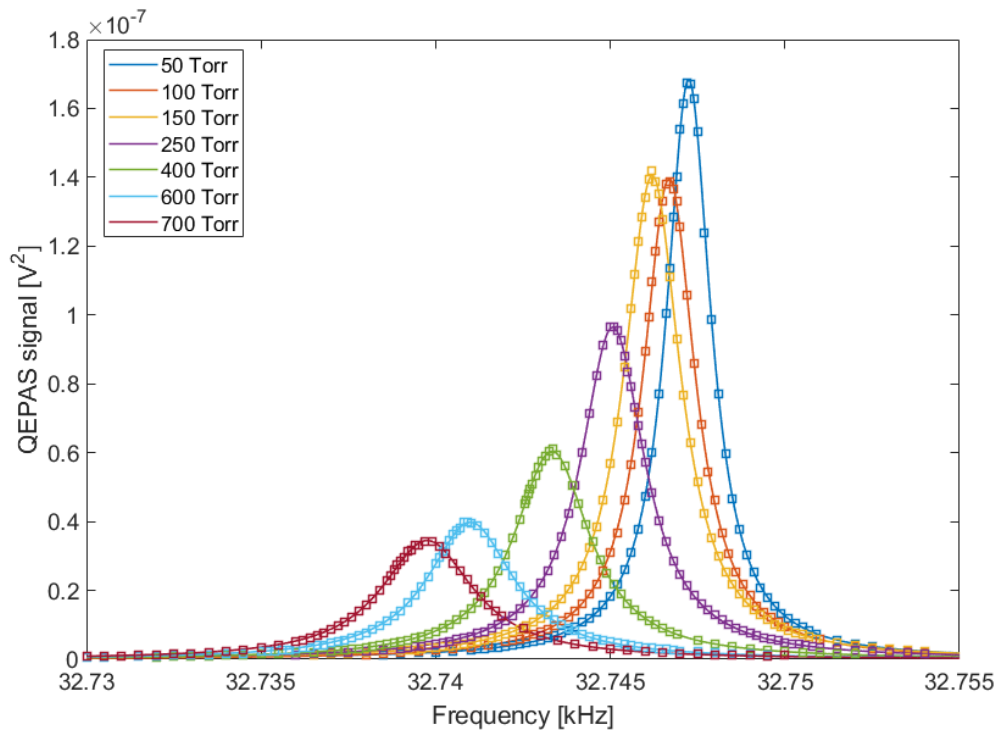


Figure 4.13 QEPAS signal (datapoints) as a function of the demodulation frequency at different pressures (TIA configuration); solid lines represent the Lorentzian fit of the experimental data.

Since the QEPAS signal is proportional to the concentration of the detected gas [43,85], it is possible to relate the LIA output signal to the measured water concentration. Figure 4.14 shows the trend of the QEPAS signal normalized to absolute humidity (AH) as a function of the air pressure.

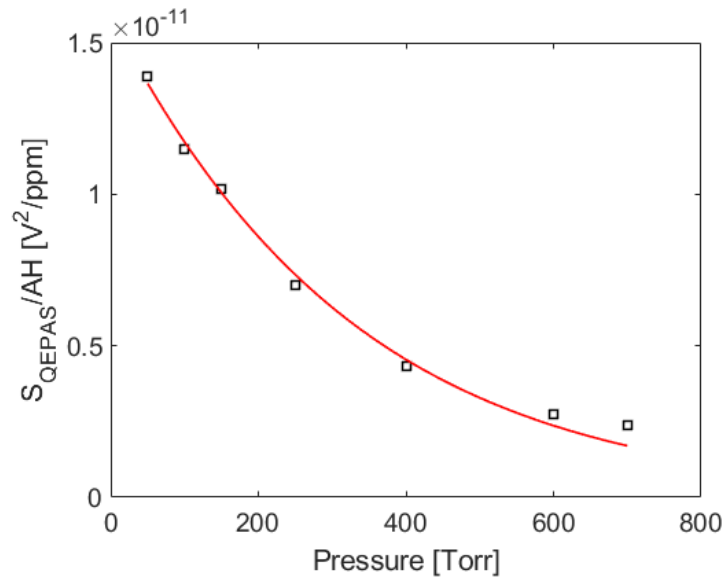


Figure 4.14 Normalized QEPAS signal peaks in TIA versus pressure (datapoints) and exponential fit of experimental data (solid red line). S_{QEPAS} – QEPAS signal, AH – absolute humidity.

The normalized signal follows the same exponential-like decay of the QTF quality factor depicted in Fig. 4.7.

4.3.3 Noise measurements

The same procedure employed to measure the QEPAS signal was applied for the noise analysis, with the laser source turned off [59]. Figure 4.15 shows the noise level nearby the QTF resonance frequency at 100 Torr, as representative.

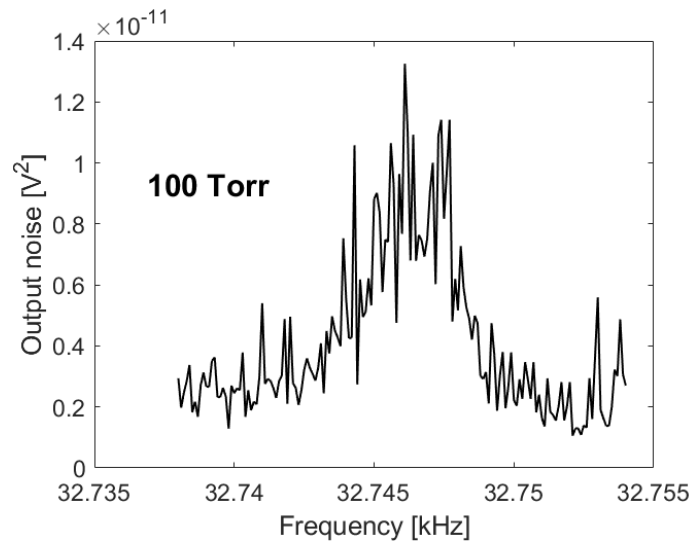


Figure 4.15 LIA output noise voltage as a function of the demodulation frequency in TIA configuration.

For each pressure, the peak value of the noise is extracted and plotted as a function of the pressure in Fig. 4.16.

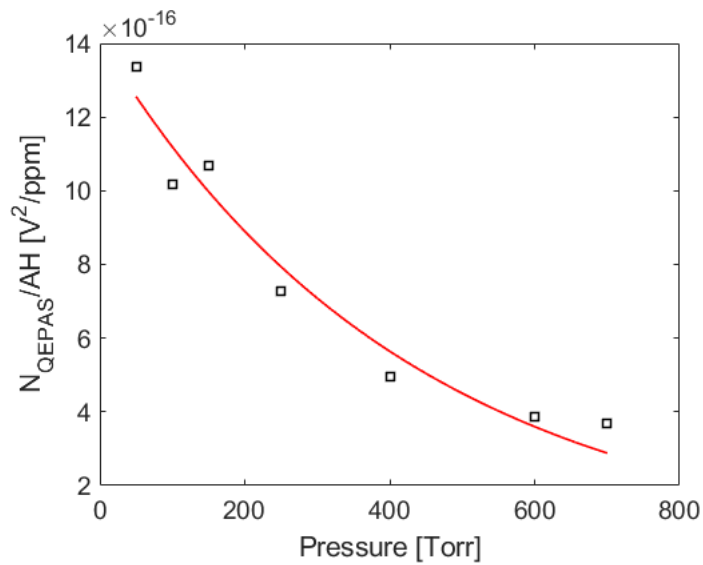


Figure 4.16 Noise peaks in TIA normalized to water concentration (datapoints), as a function of the working pressure, and exponential fit of experimental data (solid red line). N_{QEPAS} – QEPAS noise, AH – Absolute Humidity.

The experimental data follows the same exponential-like trend observed for the

QEPAS peak signals (Fig. 4.14). As expected, since the dominant noise contribution is due by the QTF thermal noise, the transfer function of the total output noise coincides with the signal transfer function.

The SNR at the output of the lock-in amplifier in the investigated pressure range can now be estimated. Figure 4.17 shows the SNR as a function of the pressure (datapoints).

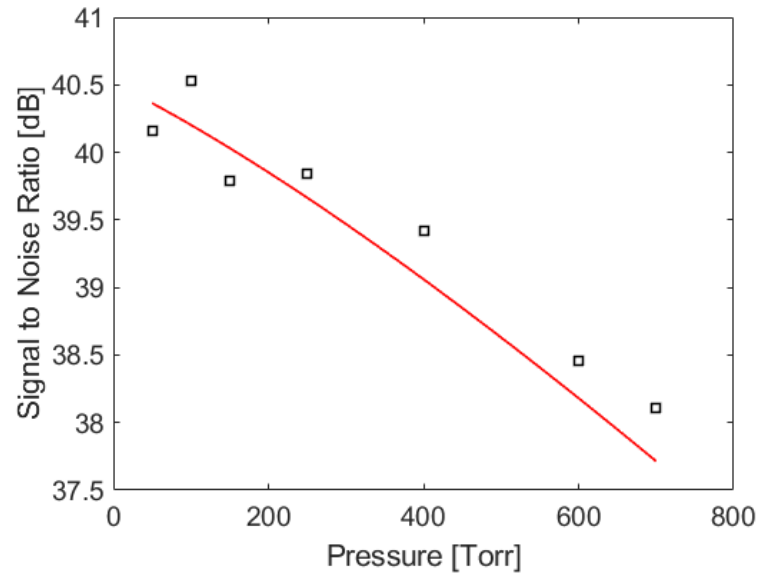


Figure 4.17 Signal to Noise Ratio peak (datapoints) versus pressure at the output of the lock – in amplifier. Solid red line is the ratio between the fit function of the normalized QEPAS signal peaks (solid line in Fig. 4.14) and the fit function of the noise peaks (solid line in Fig. 4.16).

The red solid line is the ratio between the fit function of the normalized QEPAS signal peaks (red solid line in Fig. 4.14) and the fit function of the noise peaks (red solid line in Fig. 4.16). The red solid line in Fig. 4.17 shows that the SNR decreases almost linearly with the pressure; however, the highest SNR occurs at 100 Torr, and its value is approximately 40.5 dB.

Recently [59], a SNR of 32.46 dB was demonstrated for a QEPAS-based water vapor detection system at atmospheric pressure, employing a TIA as QTF readout electronics. Therefore, the presented result shows a 6 dB increase of the total SNR with

the analyzed TIA configuration (see Fig. 4.16).

Figure 4.18 shows the demodulation frequencies at which the SNR peak values occur.

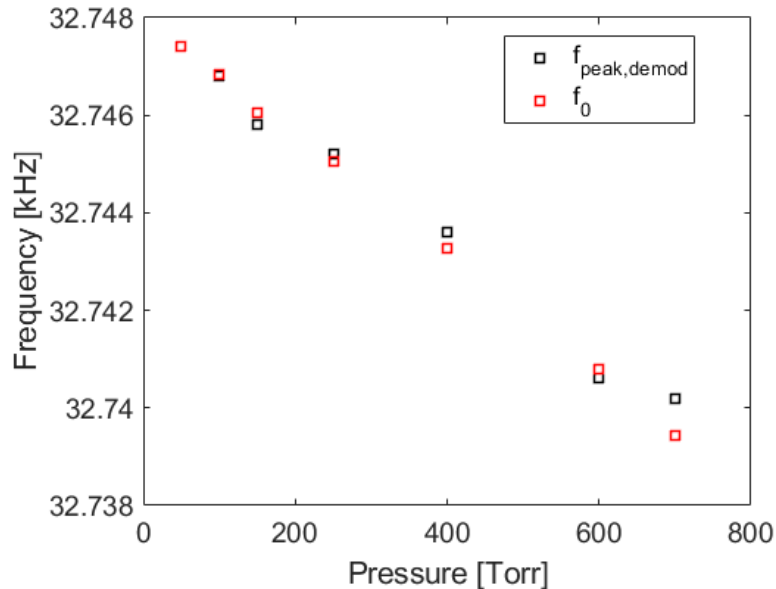


Figure 4.18 Demodulation frequencies corresponding to the SNR peak (black squares) and QTF resonance frequencies (red squares) versus pressure (TIA configuration).

Apart from the measurement at the atmospheric pressure, the demodulation frequency corresponding to the peak value of the SNR is coincident with the QTF resonance frequency within 0.02%, as already proved by the theoretical model described in section 3.3. As a result, it is convenient to work at lower pressures to maximize the SNR at the output of the LIA, thus enhancing the detection capabilities of the QEPAS sensor.

4.4 QEPAS sensor with CSA for QTF readout

The same measurements described in section 4.3 were also performed employing a CSA as QTF analog preamplifier, with the aim of comparing the SNR at the output of the lock – in amplifier to that measured with the transimpedance amplifier. In the CSA, the feedback network consists of a 2.2 pF capacitor connected in parallel to a 100

M Ω resistor, to provide a discharge path to the feedback capacitor.

4.4.1 Signal measurements

The same procedure used to measure the QEPAS signal with the transimpedance preamplifier configuration was employed to investigate the trend of the QEPAS signal as a function of the pressure in the CSA configuration. As in section 4.3, the QEPAS sensor operates in wavelength modulation and second harmonic detection. The modulation amplitudes and frequencies which maximize the output signal are reported in Table 4.5.

Pressure [Torr]	Modulation amplitude [mVpp]	$f_{\text{mod,peak}}$ [Hz]	$f_0/2$ [Hz]
50	12.6	16373.61	16373.71
100	14.2	16373.31	16373.42
150	19.0	16373.02	16373.02
250	28.5	16372.45	16372.53
400	44.3	16371.59	16371.63
600	66.4	16370.33	16370.40
700	79.1	16369.43	16369.72

Table 4.5 Parameters of the modulation signal that maximize the amplitude of the LIA output signal in CSA configuration. $f_{\text{mod,peak}}$ is the modulation frequency corresponding to the peak of the output signal, f_0 is the QTF resonance frequency.

The trend of the QEPAS signal as a function of the demodulation frequency at different pressures is plotted in Fig. 4.19.

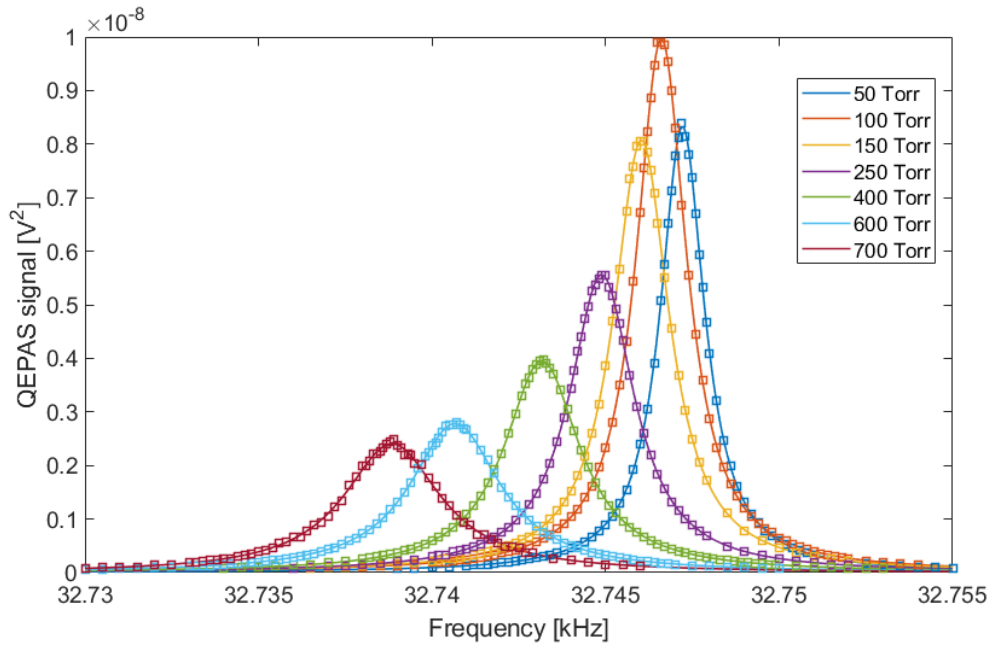


Figure 4.19 QEPAS signal (datapoints) as a function of the demodulation frequency at different pressures (CSA configuration); solid lines represent the Lorentzian fit of the experimental data.

Conversely to what was observed in the TIA configuration, the peak voltage at f_0 is 100 μV , at 100 Torr. This value is slightly higher with respect to the one measured at 50 Torr, which is 94 μV . This result is not consistent with the theoretical model, since at the resonance frequency the output signal is expected to increase as the pressure decreases. For this reason, this datapoint will be not considered in the following analysis.

The peaks values of the QEPAS signal were extracted and normalized with respect to the water concentration, as shown in Fig. 4.20 as a function of the pressure.

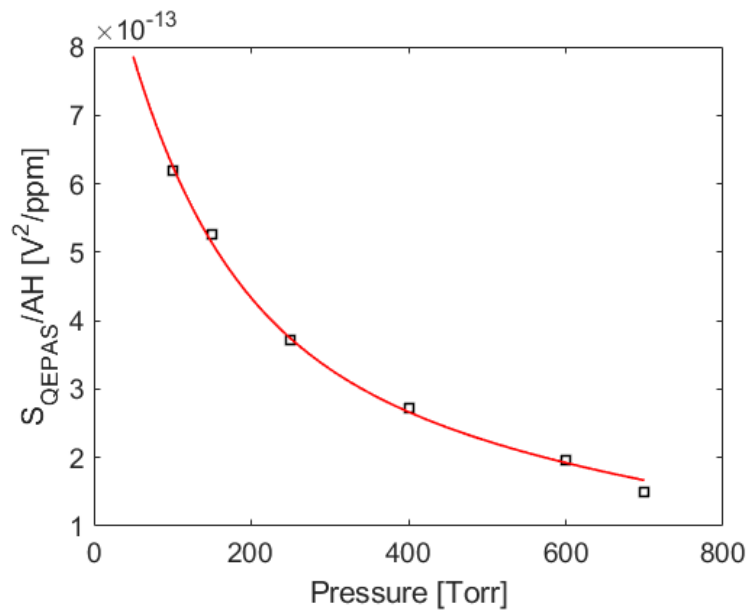


Figure 4.20 Normalized QEPAS signal peaks in CSA versus pressure (datapoints) and exponential fit of experimental data (solid red line). S_{QEPAS} – QEPAS signal, AH – absolute humidity.

It is worth noticing that the experimental data follow the same exponential-like trend observed for the TIA configuration.

4.4.2 Noise measurements

With the same procedure described in section 4.3.3, the output noise was measured and then normalized to the environmental water concentration. Figure 4.21 shows experimental data (black squares) and their best fit.

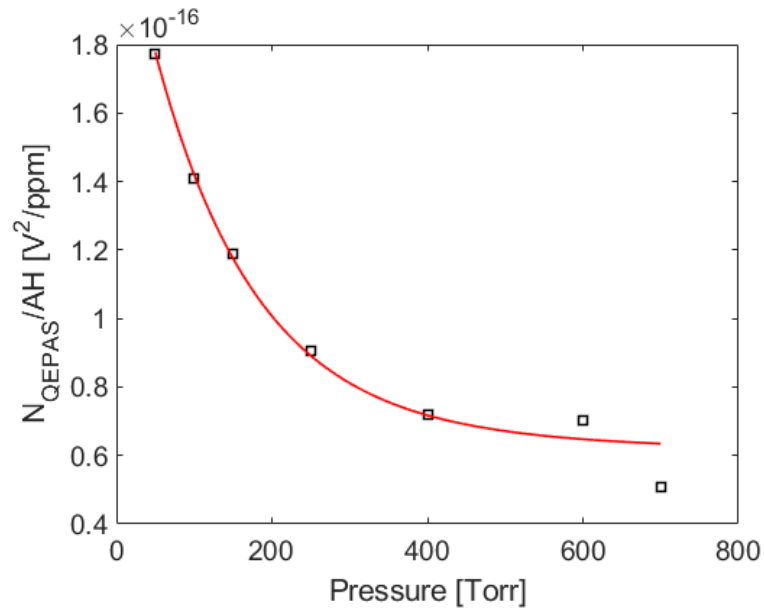


Figure 4.21 Noise voltage peaks in CSA normalized to water concentration (datapoints), as a function of the working pressure, and exponential fit of experimental data (solid red line). N_{QEPAS} – QEPAS noise, AH – Absolute Humidity.

Again, the normalized output noise follows the same exponential-like trend already discussed in the other configurations. The SNR as a function of the pressure is plotted in Fig. 4.22 for the CSA configuration (datapoints). Also, the ratio between the fit function of the normalized QEPAS signal peaks (red solid line in Fig. 4.20) and the fit function of the noise peaks (red solid line in Fig. 4.21) is reported as a red solid line.

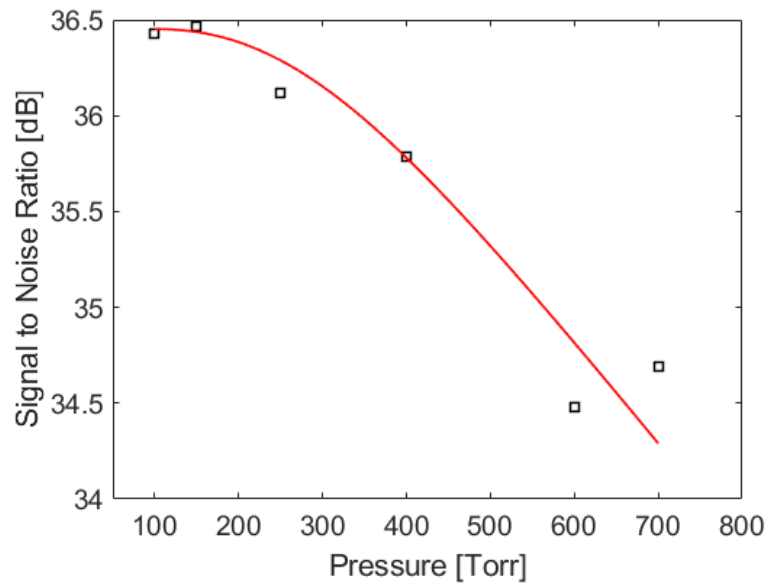


Figure 4.21 Signal to Noise Ratio peak (datapoints) versus pressure at the output of the lock – in amplifier. Solid red line is the ratio between the fit function of the normalized QEPAS signal peaks (solid line in Fig. 4.20) and the fit function of the noise peaks (solid line in Fig. 4.21).

As for the TIA configuration, the SNR decreases almost linearly with the pressure. Similarly, the frequency at which the peak of the output SNR occurs is almost coincident with the QTF resonance frequency, as shown in Fig. 4.23.

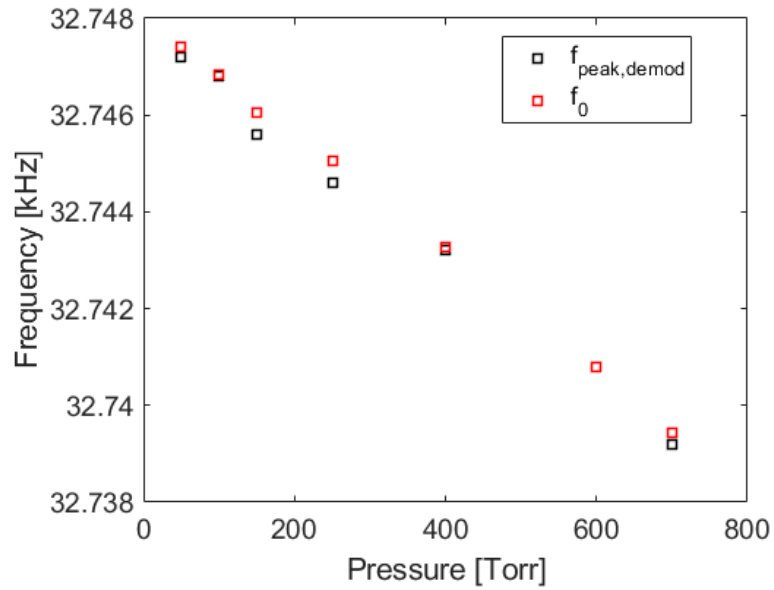


Figure 4.23 Demodulation frequencies corresponding to the SNR peak (black datapoints) and QTF resonance frequencies (red datapoints) versus pressure (CSA configuration).

In conclusion, in both TIA and CSA configurations, the SNR can be maximized by lowering the working pressure and modulating the laser at half the resonance frequency of the QTF; indeed with a lock-in amplifier time constant of 100 ms, the intrinsic resistance of the QTF generates the dominant noise contribution, and the SNR is inversely proportional to R , in both configurations.

Chapter 5: Fully differential front-end, a further improvement

The theoretical study presented so far, along with the experimental results, proves that the TIA and CSA configurations for the readout of a QTF yield similar results in terms of SNR, hence they can be both effectively employed in the design of the AFE of a QTF.

In order to further improve the performance of the front-end electronics and enhance the detectivity of a QEPAS sensor, the use of a different topology of preamplifier can be investigated.

In particular, many works proved that differential amplifiers can achieve a higher total SNR with respect to single-ended amplifiers [54,56,59], thanks to their immunity to the common mode noise and wider output dynamic range.

In this chapter, the working principle of a fully differential amplifier is briefly presented, and a comparison with the previously analyzed preamplifier configurations is provided.

5.1 Architecture of a fully differential amplifier

A fully differential amplifier (FDA) is very similar to a standard voltage-feedback OPAMP (see Fig. 5.1). The main difference between the two topologies is that FDAs have differential output, whereas standard operational amplifiers have single-ended outputs. Hence, while in standard OPAMPs the output voltage is referenced to ground, in FDAs the output signal is given by the difference between the voltages at the output pins.

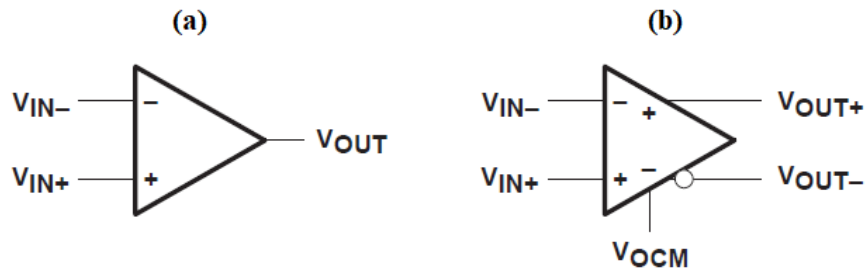


Figure 5.1 Diagram symbols of (a) a single-ended output amplifier and (b) a fully differential amplifier [86].

The output common mode voltage [87] is usually set by means of a dedicated pin (V_{ocm} in Fig. 5.1b), so that its level can be controlled independently of the differential voltage. Moreover, while in standard operational amplifiers there is just one feedback path from the output to the inverting input, in FDAs two feedback paths can be implemented.

If symmetric feedback paths are employed, the outputs of an FDA have the same amplitude and are shifted by 180 degrees; this implies that the output voltage swing increases by a factor of 2 over a single-ended output with the same voltage swing [86].

One of the main advantages of the differential configuration is that both input and output voltages are not referenced to ground, hence they are not sensitive to variations of the ground potential in the circuit. On top of that, FDAs can easily reject common mode noise at the input, thus amplifying only the differential signal.

To provide a better understanding of an FDA operation, let us consider a classic bipolar fully differential amplifier, as depicted in Fig. 5.2.

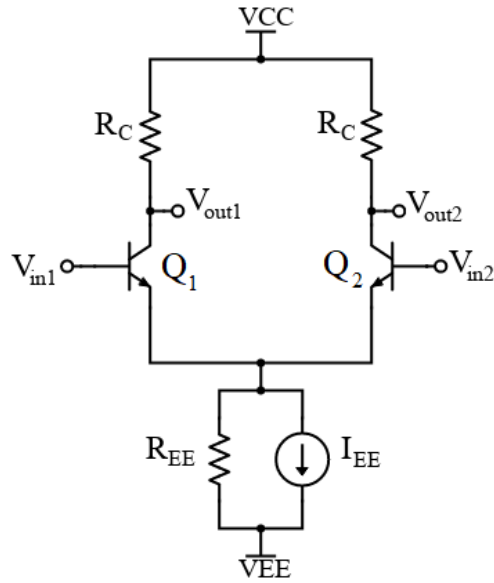


Figure 5.2 Schematic of a classic bipolar fully differential amplifier. The stage is biased by the non-ideal current source composed by I_{EE} and the resistor R_{EE} in parallel.

The input signals V_{in1} and V_{in2} are applied to the base of two matched bipolar junction transistors (BJTs), and the same collector resistance R_C is employed in both branches of the circuit. The output voltages V_{out1} and V_{out2} are probed on the collector of Q_1 and Q_2 . A current generator is connected between the emitters of Q_1 and Q_2 and the negative voltage supply, to bias the circuit.

The differential mode input signal can be defined as the difference between the input voltages:

$$V_{id} = V_{in1} - V_{in2} \quad (5.1)$$

The input voltages, in turn, can be expressed as a function of the differential mode input voltage V_{id} and the common mode input voltage V_{ic} :

$$V_{in1} = V_{ic} + \frac{V_{id}}{2} \quad (5.2)$$

$$V_{in2} = V_{ic} - \frac{V_{id}}{2} \quad (5.3)$$

$$V_{ic} = \frac{V_{in1} + V_{in2}}{2} \quad (5.4)$$

Similarly, the differential mode output signal is:

$$V_{od} = V_{out1} - V_{out2} \quad (5.5)$$

and the output voltages can be defined as a function of a differential and a common mode component, as well:

$$V_{out1} = V_{oc} + \frac{V_{od}}{2} \quad (5.6)$$

$$V_{out2} = V_{oc} - \frac{V_{od}}{2} \quad (5.7)$$

$$V_{oc} = \frac{V_{out1} + V_{out2}}{2} \quad (5.8)$$

In an FDA it is possible to define the small-signal differential mode gain A_{dm} as the ratio between the differential output voltage and the differential input voltage with input common mode set to zero:

$$\begin{aligned} A_{dm} &= \left. \frac{V_{od}}{V_{id}} \right|_{V_{ic}=0} \\ &= \left. \frac{V_{out1} - V_{out2}}{V_{in1} - V_{in2}} \right|_{V_{ic}=0} \end{aligned} \quad (5.9)$$

This gain can be easily calculated using the superposition principle, after imposing $V_{ic} = 0$. As a consequence, from Eqs. 5.2 and 5.3:

$$V_{in1} = +\frac{V_{id}}{2} \quad (5.10)$$

$$V_{in2} = -\frac{V_{id}}{2} \quad (5.11)$$

Since the bases of Q_1 and Q_2 have opposite polarities, the variations of the emitter currents of Q_1 and Q_2 with respect to the bias point are equal but opposite. As a consequence, no signal current flows through the bias resistor R_{EE} , thus the emitters of the BJTs behave as a virtual ground for the voltage signals (see Fig. 5.3).

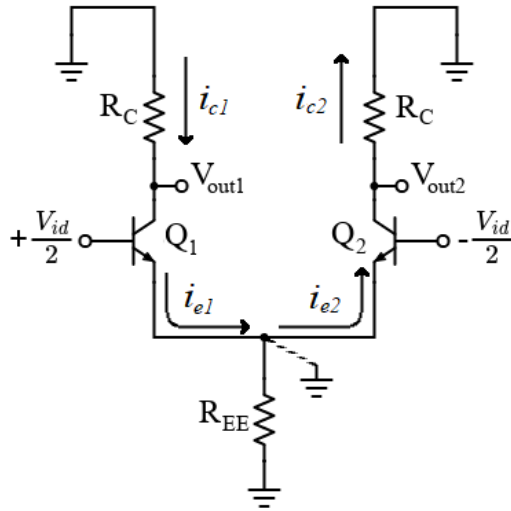


Figure 5.3 Equivalent circuit for the calculation of the small-signal differential mode gain: the common emitter of Q_1 and Q_2 is a signal ground.

The current signal in the collector of Q_1 is:

$$\begin{aligned} i_{c1} = i_{c2} &= g_m \cdot v_{be1} \\ &= g_m \cdot \frac{V_{id}}{2} \end{aligned} \quad (5.12)$$

where g_m is the transconductance of Q_1 and Q_2 . The output voltages v_{out1} and v_{out2} can then be calculated as follows:

$$v_{out1} = -v_{out2} = -g_m R_C \frac{V_{id}}{2} \quad (5.13)$$

The differential voltage at the output of the amplifier (see Eqs. 5.5 and 5.9) is:

$$\begin{aligned} V_{od} &= v_{od} \\ &= -g_m R_C V_{id} \Rightarrow \\ A_{dm} &= -g_m R_C \end{aligned} \quad (5.14)$$

Therefore, the differential mode gain of a bipolar FDA corresponds to the gain of a BJT in common emitter configuration.

The common mode gain A_{cm} is calculated imposing $V_{id} = 0$, i.e. $V_{i1} = V_{i2} = V_{ic}$, according to the following definition:

$$A_{cm} = \left. \frac{V_{oc}}{V_{ic}} \right|_{V_{id}=0}$$

The equivalent circuit for the calculation of A_{cm} is depicted in Fig. 5.4.

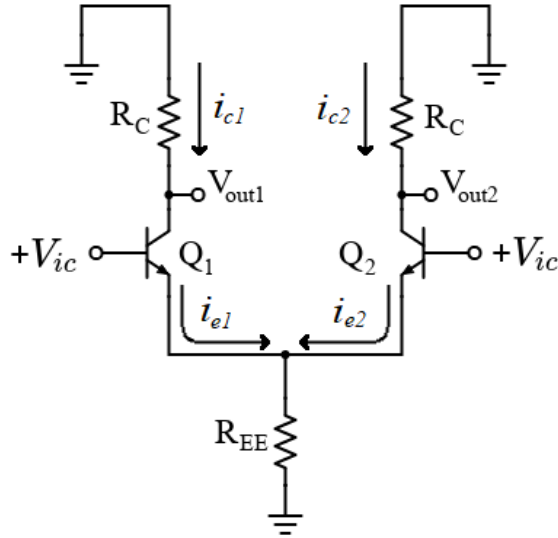


Figure 5.4 Equivalent circuit for the calculation of the small-signal common mode gain.

In the common mode equivalent circuit, the current signals in the emitters of the BJTs i_{e1} and i_{e2} flow in the same direction, therefore the resistance R_{EE} cannot be neglected. The common mode gain is:

$$A_{cm} = -\frac{g_m R_C}{1 + 2g_m R_{EE}} \quad (5.15)$$

which corresponds to the gain of a BJT in common emitter configuration, but with a large $2R_{EE}$ degeneration resistance.

The capability of rejecting the common mode noise is defined by the ratio between A_{dm} and A_{cm} . This parameter is known as Common Mode Rejection Ratio (CMRR). In the described example, the CMRR is:

$$\begin{aligned}
 CMRR &= \frac{A_{dm}}{A_{cm}} = \frac{g_m R_C}{\frac{g_m R_C}{1 + 2g_m R_{EE}}} \cong 2g_m R_{EE} \\
 &= 2 \frac{I_C}{v_T} R_{EE} = \frac{I_{EE} R_{EE}}{v_T}
 \end{aligned}
 \tag{5.16}$$

where $I_C = I_{EE}/2$ is the bias collector current of Q_1 and Q_2 , and $v_T = kT/q$ is the thermal voltage.

Typically, CMRR can reach up to 120 dB, but tends to decrease when the operative frequency increases. Hence, when working at high frequencies, additional circuitry should be implemented in the circuit layout, in order to ensure an effective common mode rejection [88].

5.2 Fully differential amplifiers for QTF readout

5.2.1 Fully differential transimpedance amplifier

FDAs can be effectively employed to implement the AFE electronics of a QTF in a QEPAS sensor. In particular, fully differential transimpedance amplifiers can be used in place of their single-ended counterpart, already described in chapters 2 and 3, in order to further improve the total SNR.

The schematic circuit of a fully differential TIA is displayed in Fig. 5.5.

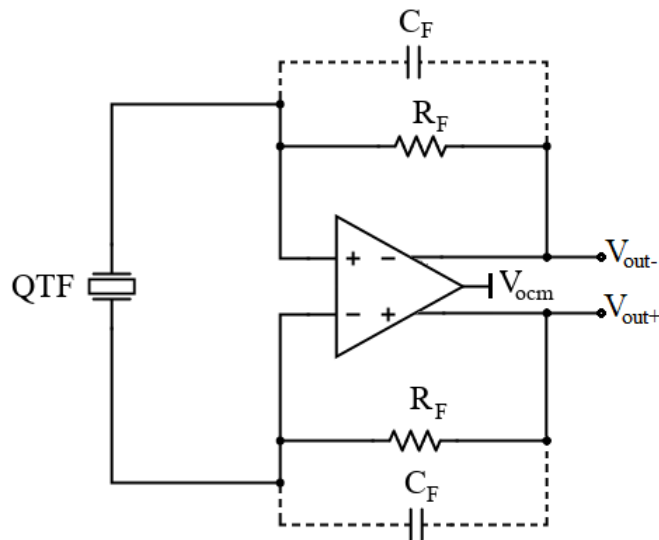


Figure 5.5 Schematic circuit of a fully differential transimpedance amplifier. The dashed capacitor C_F models the stray capacitance of the feedback network.

The QTF is connected across the inputs of the amplifier, and two feedback resistors connect each input to the differential output pins. The output common mode pin V_{ocm} is used to set the output common-mode voltage [89].

The analysis of the SNR in a TIA configuration presented in chapters 2 and 3 applies with the same results and equations also for a fully differential transimpedance amplifier [86,90]. The main difference is that in the differential configuration the output signal at the resonance frequency f_s is two times the output signal in the single-ended configuration.

Figure 5.6 reports a SPICE simulation of the output signal of the circuit shown in Fig. 5.5, compared to a single-ended TIA output signal. The parameters listed in table 2.1 were employed to model the QTF. Furthermore, the model of the THS4567 fully differential amplifier, produced by Texas Instruments, was chosen to simulate the behavior of the fully differential TIA configuration.

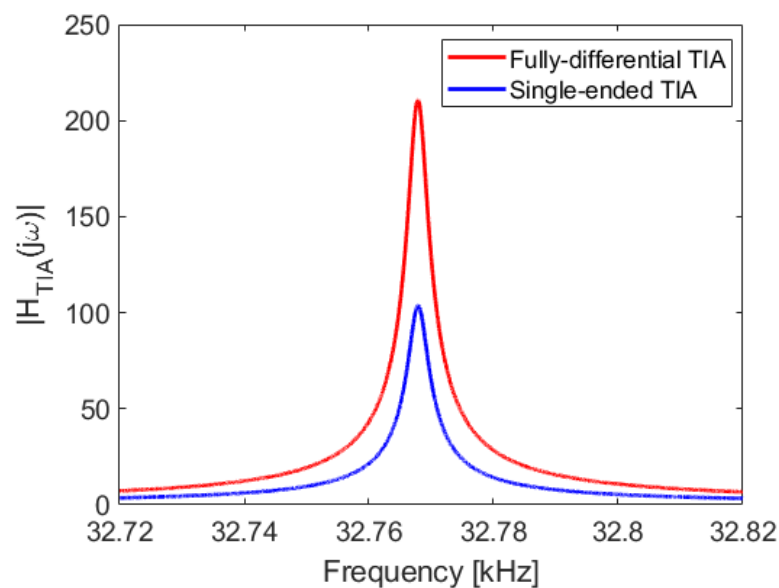


Figure 5.6 SPICE simulation response of a fully differential TIA (red solid line) and a single-ended TIA (blue solid line), normalized to a 1 V input signal amplitude. The gain of the stage is set by a 10 M Ω feedback resistor.

As for the noise analysis, fully differential and single-ended configurations are characterized by the same output noise spectral density, as shown in Fig. 5.7.

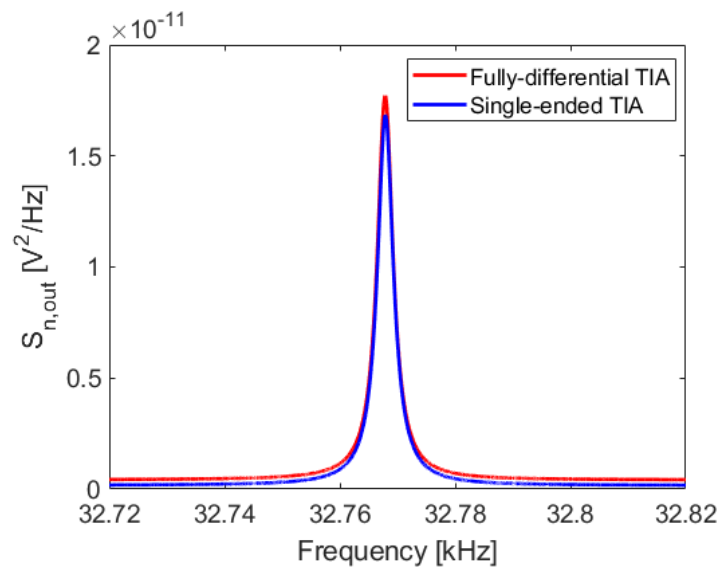


Figure 5.7 SPICE simulation of output noise spectral density in a fully differential TIA (red solid line) and a single-ended TIA (blue solid line).

As a result, the total SNR at the output of the fully differential TIA is 6 dB higher than the one obtained with the single-ended configuration, as shown in Fig. 5.8.

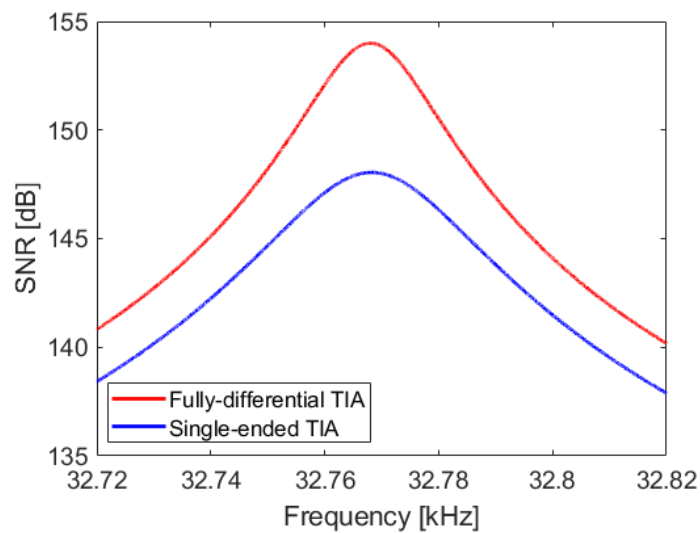


Figure 5.8 SPICE simulation of the output SNR normalized to a 1 Hz equivalent noise bandwidth, in a fully differential TIA (red solid line) and a single-ended TIA (blue solid line).

Therefore, employing a fully differential TIA improves the performance of the QEPAS sensor, raising the SNR by a factor of two, thus enhancing the detection capabilities of the whole detection system.

5.2.2 Fully differential charge sensitive amplifier

Similarly, it is possible to configure an FDA in charge-sensitive mode of operation, according to the schematic shown in Fig. 5.9.

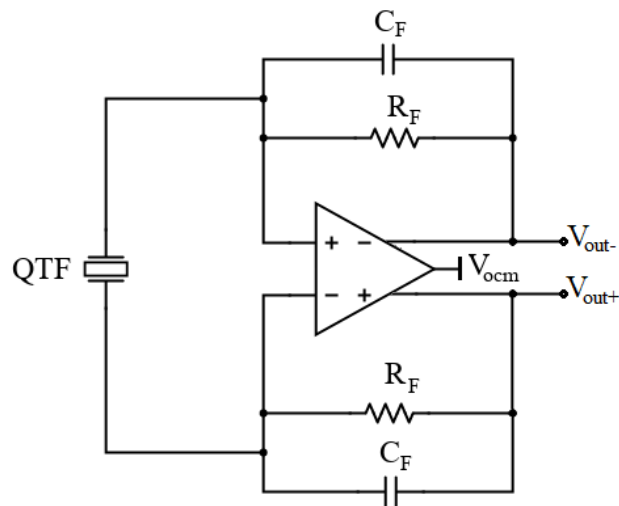


Figure 5.9 Schematic circuit of a fully differential charge-sensitive amplifier.

As already observed in the previous section, the gain of the fully differential configuration is two times the one obtained with the single-ended configuration (see Fig. 5.10).

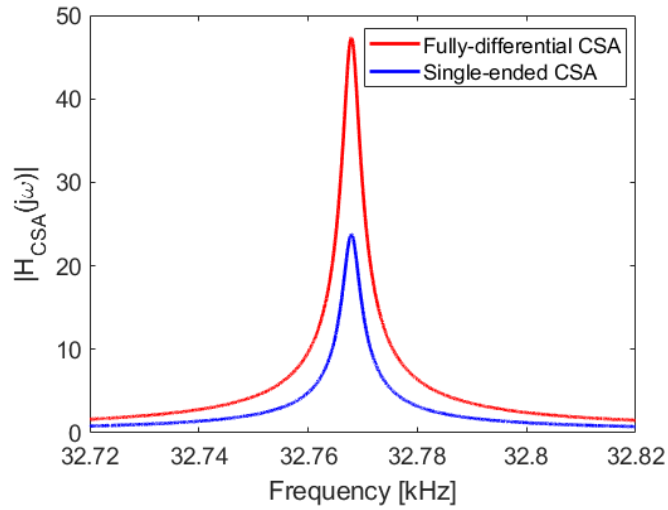


Figure 5.10 SPICE simulation of the response of a fully differential CSA (red solid line) and a single-ended CSA (blue solid line), normalized to a 1 V input signal amplitude. The gain of the stage is set by a 2.2 pF feedback capacitor and a 100 MΩ feedback resistor.

Moreover, the output noise spectral density is the same in both configurations, as reported in the SPICE simulation shown in Fig. 5.11.

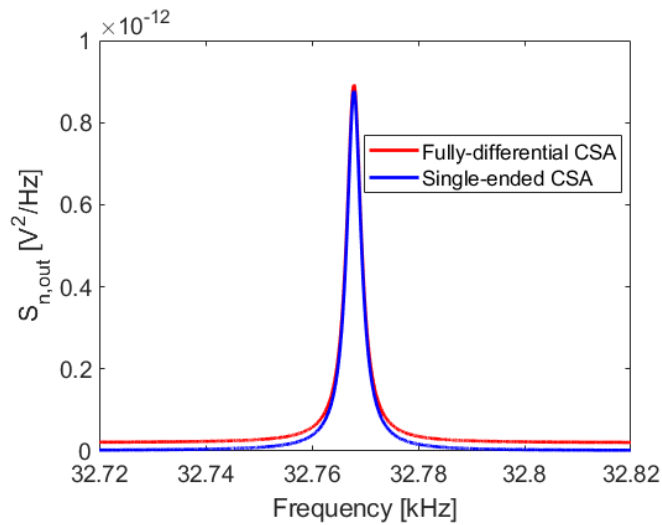


Figure 5.11 SPICE simulation of output noise spectral density in a fully differential CSA (red solid line) and a single-ended TIA (blue solid line).

Therefore, the output SNR at the QTF series-resonant frequency with a fully

differential configuration is twice the SNR obtained with a single-ended configuration, as reported in Fig. 5.12.

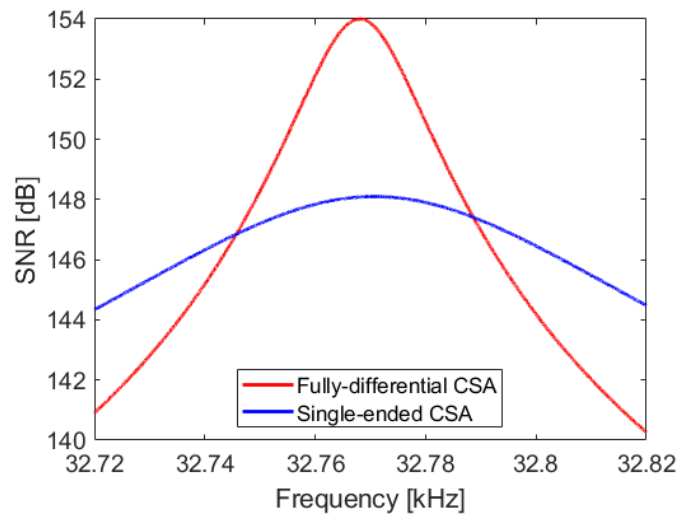


Figure 5.12 SPICE simulation of the output SNR normalized to a 1 Hz equivalent noise bandwidth, in a fully differential CSA (red solid line) and a single-ended CSA (blue solid line).

It is worth noticing that the value of the normalized SNR at f_s in the fully differential CSA configuration coincides with the one obtained with the fully differential TIA. Hence, the same conclusions of chapters 2 and 3 apply to the FDA architecture.

5.2.3 Signal-to-noise measurement with a fully differential CSA

Experimental measurements aimed at evaluating the SNR achievable with a fully differential CSA were performed, employing a 15.8 kHz bare QTF with a quality factor of 15000 at atmospheric pressure. A DFB laser emitting at 1392 nm was used as light source, in order to match the water absorption spectrum.

A PCB implementing the fully differential CSA configuration was realized, with a 100 M Ω feedback resistor and a 2.2 pF feedback capacitor. THS4567 amplifier was mounted on board, and its differential output was connected to the input of a variable-gain amplifier (AD8338 by Analog Devices), which provides a further programmable

gain, ranging from 0 to 80 dB. A 14 bits analog to digital converter (ADC141S626 by Texas Instruments) was mounted on the board, in order to digitize the output signal of the preamplifier.

An FPGA development board (DE0-NANO by Terasic) and a custom D/A board were employed to implement a digital lock-in amplifier, and to generate:

- (i) the modulation signal of the laser (i.e., the sum of a current ramp and an $f_s/2$ sinewave).
- (ii) the control signal of the VGA.
- (iii) the calibration signal of the QTF.

The control voltage of the VGA was set to 0.3 V, in order to provide a further 16 dB gain. The $2f$ -QEPAS signal was then retrieved by sweeping the laser modulation current between 75 and 110 mA, as shown in Fig. 5.13.

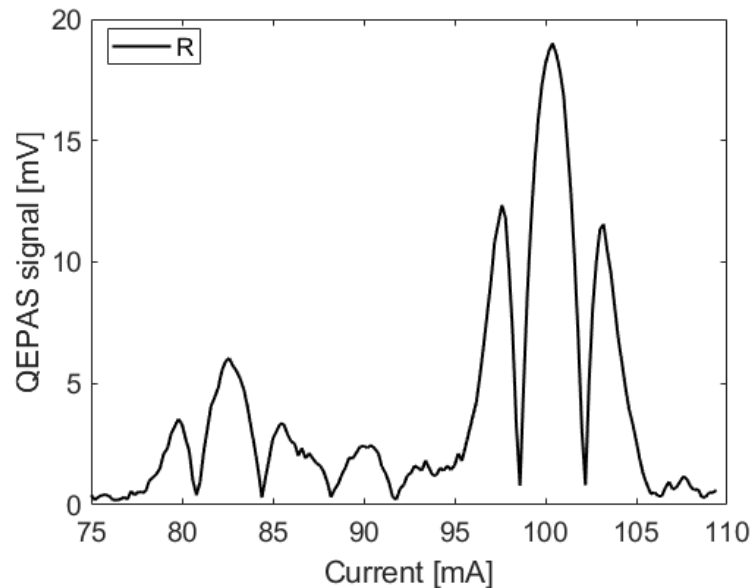


Figure 5.13 $2f$ -QEPAS signal of water vapor in laboratory environment, acquired with a fully differential CSA. The gain of the VGA was set to 16 dB.

Two peaks of the water absorption spectrum can be clearly resolved; the highest one occurs with a driving current of about 100.4 mA. The amplitude of the average QEPAS signal measured on the water absorption peak is 19 mV.

Then, an Allan deviation plot was acquired, keeping the laser on, far from the

absorption peak of the water vapor. The result is displayed in Fig. 5.14.

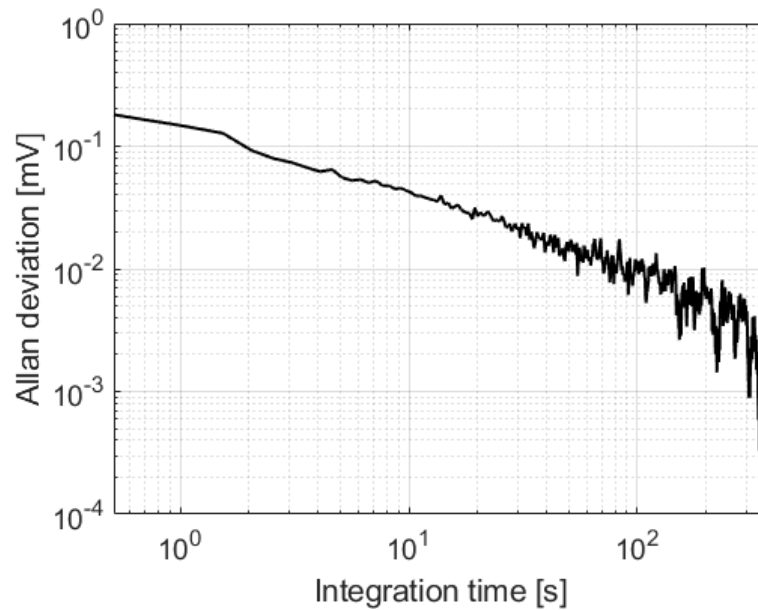


Figure 5.14 Allan deviation plot of the QEPAS sensor noise with laser on.

The output noise obtained with a 500 ms integration time is about 181 μV , resulting in an overall SNR of 40.4 dB, leading to a remarkable improvement of the results obtained with the single-ended configuration, where the SNR obtained at atmospheric pressure is 34.7 dB (see Fig. 4.21).

Therefore, we can conclude that employing a fully-differential preamplifier for the readout of a QTF remarkably enhances the performance of a QEPAS sensor, by increasing the dynamic range of the output signal and strongly improving the signal integrity.

These measurements pave the way for designing an application-specific integrated circuit (ASIC), which would allow for a better signal path matching and thus, a further enhancement of the QEPAS SNR.

Conclusions and future perspectives

The aim of this thesis work was the investigation of the pressure dependence of the main parameters of a QEPAS sensor, and the improvement of the state-of-art analog front-end electronics for the readout of a QTF.

QEPAS sensors are well suitable for industry 4.0 applications; thanks to their compactness, robustness, wide detection range, real-time and in-situ operations, they perform instantaneous and accurate measurements of trace gas concentrations, ranging from ppm to percentage levels.

A study of the influence of air pressure on QTF resonance properties is fundamental to define the best working pressure, and to further enhance the performance of a QEPAS sensor. The analysis proposed, together with the experimental results, showed that when the QTF vibrates in air, the effect of the surrounding medium affects the resonance frequency, whereas energy dissipation in air reduces the Q -factor. The shielding effect of tubes in a spectrophone causes a reduction of the additive mass; therefore, the effect of air on vibrating prongs is attenuated. Moreover, at low pressures the quality factor of a spectrophone weakly deviates from that of the bare QTF. At higher pressures, the acoustic coupling is stronger, leading to an increase in resonance frequency and a decrease in quality factor.

Analytical models of three different configurations of the QTF front-end preamplifier were developed and validated. The comparison of these models allowed to define the performances of the analyzed configurations in terms of SNR. In the voltage amplifier configuration, the value of the bias resistor strongly affects the SNR and its peak frequency: for $R_L < 10 \text{ M}\Omega$ the peak of SNR is located at the series-resonant frequency of the QTF, whereas for higher R_L values it shifts towards the parallel-resonant frequency. When the lock-in filter time constant is sufficiently high, the frequency trend of the SNR is quite flat around the peak frequency, therefore the choice of the operating frequency is not critical. If faster measurements are needed, and a lower time constant is employed, the SNR becomes sharper for large R_L values.

In the TIA configuration the peak of the SNR always lies in correspondence of

the series resonant frequency. For high time constants, the SNR rapidly drops as the lock-in integration bandwidth increases, since the noise contribution from the QTF intrinsic resistance is the dominant one. For low values of τ , R_F noise contribution prevails, and the SNR tends to increase together with the feedback resistance.

In the CSA configuration, as the integration bandwidth increases, the SNR becomes flat. Therefore, a lower time constant can be employed to shorten the acquisition time, without significantly reducing the total SNR.

The reported study suggests that TIA and CSA configurations show similar performances in terms of SNR, while the voltage amplifier can achieve the same peak SNR at f_P with an R_L value as large as 100 M Ω . Therefore, an accurate estimation of the OPAMP input parasitic capacitance would be mandatory to maximize the SNR; moreover, such a large bias resistance might lead to undesirable offset levels.

Experimental measurements on a QEPAS setup for water vapor detection with varying pressure proved that the SNR increases as the pressure decreases, as the noise associated to the QTF intrinsic resistance is lower. Results show that the transimpedance configuration is the most promising architecture for the QTF readout; the obtained results show a remarkable improvement of the SNR with respect to the state-of-the-art configurations. The performance of the front-end electronics can be significantly enhanced by employing a fully differential amplifier as QTF readout preamplifier, thus leading to a 6 dB increase of the SNR with respect to single ended configurations.

Furthermore, an FDA can be easily interfaced with a differential ADC, thus allowing the digital control of the whole QEPAS front-end system. In this way, bench instrumentation can be replaced by an FPGA and/or a microcontroller, which can be directly connected to a personal computer, to control the measurement and retrieve in real-time the acquired data. Finally, by getting rid of bulky instruments, it would be possible to implement the whole QEPAS setup on drones or unmanned aerial vehicles (UAVs), to perform in-situ measurements of trace gas concentration.

Appendix

A.1 Fitting algorithm for the extraction of the electrical parameters of a QTF

A MATLAB function for determining the electrical parameters of a QTF (L , C_s , C_p and R) was written. The inputs of the algorithm are the frequency vector and the module of the QTF impedance. Then, a system of 4 equations is solved, and the four unknown parameters are retrieved in double-precision format.

```
function [L,Cs,Cp,R] = QTFparams(freq,modZ)
```

A.1.1 Series and parallel resonant frequency of the QTF

```
N = size(modZ,2); % number of acquisitions

for i=1:N
    [min_Z(i,1), i_fs(i,1)] = min(modZ(:,i));
    fs(i,1) = freq(i_fs(i,1)); % series resonance frequency

    [max_Z(i,1), i_fp(i,1)] = max(modZ(:,i));
    fp(i,1) = freq(i_fp(i,1)); % parallel resonance frequency
end
```

A.1.2 Solving the system

```
for i=1:N

    syms ind c_s c_p rp positive % symbolic variables; only positive solutions are
    taken into account

    eq1(i,1) = 1/sqrt(ind*c_s) == 2*pi*fs(i,1); % series resonance frequency
    equation
    eq2(i,1) = 1/sqrt(ind*c_p*c_s/(c_p+c_s)) == 2*pi*fp(i,1); % parallel resonance
    frequency equation
    eq3(i,1) = rp^2*ind*c_s/(rp^2*c_p^2+ind*c_s) == min_Z(i,1)^2; % minimum value
    of squared module of impedance at f_s
```

```

eq4(i,1) = (ind^2*(c_s/c_p)^2 + rp^2*ind*c_s/c_p*(c_s+c_p))/(rp^2*(c_s+c_p)^2)
== max_z(i,1)^2; % peak value of squared module of impedance at f_p

sol(i,1) = solve([eq1(i,1), eq2(i,1), eq3(i,1), eq4(i,1)], [ind c_s c_p
rp], 'real', true); % solving the system

```

A.1.3 Converting the parameters in double format

```

L(i,1) = double(sol(i,1).ind);
Cs(i,1) = double(sol(i,1).c_s);
Cp(i,1) = double(sol(i,1).c_p);
R(i,1) = double(sol(i,1).rp);

clear ind c_s c_p rp

```

end

end

A.2 Measurement of the absolute humidity

The absolute humidity was measured with the HYT271 sensor, produced by Innovative Sensor Technology (see section 4.3.1). An ESP32 board was used to read sensor data, and transmit them on a wireless network, where they can be accessed by any authenticated user. ESP32 is a microcontroller unit (MCU), with integrated Wi-Fi connectivity, supporting a wide range of IoT applications.

Another ESP32 board was used to receive transmitted data, according to the scheme depicted in Fig. A.2.1.

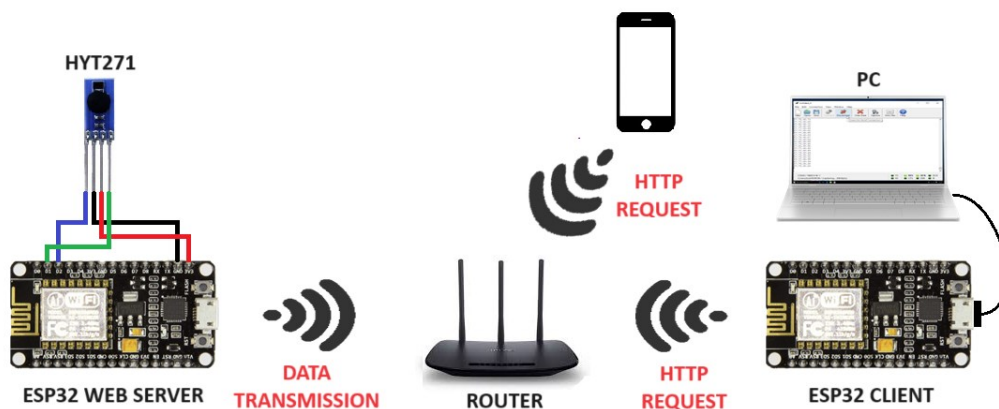


Figure A.2.1 Connection of ESP32 boards for the measurement of the absolute humidity.

The server connects to a local network and builds an asynchronous web server, transmitting data read by the sensor to a specific IP address. In this way, multiple connections can be handled at the same time. The client queries the same IP address every 5 seconds with an HTTP get request, and prints received data on a serial monitor. Data are accessible by any other device authenticated to the wireless network, such as a smartphone (see Fig. A.2.2).

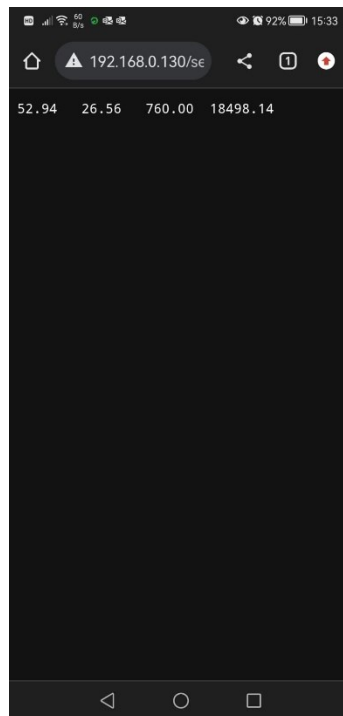


Figure A.2.2 Data transmitted by the SERVER board and displayed on a CLIENT device (i.e., a smartphone). Displayed data are relative humidity (%), temperature (°C), pressure (Torr) and absolute humidity (ppm), respectively.

In the following sections, the codes running on server and client boards are shown and commented.

A.2.1 Code running on the SERVER board

```

#include <ESP8266WiFi.h>
#include <Wire.h>
#include <ESPAsyncWebServer.h>

//declaring variables

int address1 = 0x28; // address of HYT 271 sensor

byte h1,h2,t3,t4; // i2c bytes

float temperature;
float humidity;
float pressure;
float pressure_torr;
float conv_factor = 0.13332236842105; // kPa to Torr conversion
// factor

float Tc = 647.096; // critical temperature in K
float Pc = 220640.0; // critical pressure in hPa

float c1 = -7.85951783;
float c2 = 1.84408259;
float c3 = -11.7866497;
float c4 = 22.6807411;
float c5 = -15.9618719;
float c6 = 1.80122502;
float teta; // coefficients and variables to compute absolute
// humidity in ppm

unsigned int tt;
unsigned int hh;
unsigned int hh2; // auxiliar variables

const char* ssid = "PolySense"; //ssid of WiFi network
const char* password = "*****"; // password of WiFi network
// (not shown)

AsyncWebServer server(80);

void setup(){
  Wire.begin(); // initializing i2c bus
  Serial.begin(115200); // initializing serial port
  WiFi.mode(WIFI_STA); // setting WiFi in station mode

  IPAddress staticIP(192,168,0,130); // static IP address of the
// board
  IPAddress gateway(192, 168, 0, 1); // gateway IP address of the
// client
  IPAddress subnet(255, 255, 255, 0); // subnet mask

  WiFi.config(staticIP,gateway,subnet); // configuring WiFi
// communication

  WiFi.begin(ssid,password); // connecting to the network
  while(WiFi.status() != WL_CONNECTED){

```

```

        delay(500);
        Serial.print(".");
    }
    Serial.println("Connection established");
    Serial.print("IP address: ");
    Serial.println(WiFi.localIP()); // displaying the IP address of
    // the board (should be the one set previously)

    Serial.println();

    delay(500);

    Serial.println(ESP.getFreeHeap()); // display free bytes of
// memory

    server.on("/sensor1", HTTP_GET, [] (AsyncWebServerRequest *request) {
        request->send(200,
"text/plain", ReadHum(address1)+"\t"+ReadTemp()+"\t"+press_torr()+"\t"
+ppmComput());
    }); // transmitting string data to 192.168.0.130/sensor1

    delay(5000);

    server.begin(); // starting asynchronous server
} // end setup

void ReadData(int address) {

    Wire.beginTransaction(address); // beginning i2c transmission
// with "address"
    Wire.requestFrom(address, 4); // polling 4 bytes to "address" on
// the i2c bus
    while(Wire.available() == 4) { // reading 4 bytes whilst any data
// is available on the bus
        h1 = Wire.read();
        h2 = Wire.read();
        t3 = Wire.read();
        t4 = Wire.read();
    }
    int error = Wire.endTransmission();
    if(error != 0) { // if there isn't any device connected to
// "address", set to zero each byte
        h1 = 0; // the program will retrieve humidity = 0% and
// temperature = -40°C
        h2 = 0;
        t3 = 0;
        t4 = 0;
    }
}

String ReadHum(int address) {
    ReadData(address); // reading i2c data on "address"
    CalcHum(); // Call to CalcHum() method
    return (String)humidity; // float to string conversion of

```

```

// humidity data
  delay(50);
}

  void CalcHum(){
    hh = h1 & 0x3F;
    hh2 = hh<<8 | h2; // shifting and masking humidity bytes (see
// HYT271 datasheet)
    humidity = (100*hh2)/pow(2,14); // computing percentual relative
// humidity
  }

  String ReadTemp(){
    CalcTemp(); // Call to CalcTemp() method
    return (String)temperature; // float to string conversion of
// temperature data
    delay(50);
  }

  void CalcTemp(){
    tt = t3 << 8 | t4 & 0xFC; // shifting and masking temperature
// bytes (see HYT271 datasheet)
    temperature = ((tt / pow(2,16)) * 165.0) - 40.0; // computing
// temperature in Celsius degrees
  }

  String ReadPress(){

    pressure = 101.325; // atmospheric pressure in kPa
    return(String)pressure; // float to string conversion of pressure
// data

  }

  String press_torr(){
    pressure_torr = pressure/conv_factor; // converting the pressure
// from kPa to Torr
    return(String)pressure_torr; // converting the pressure from
// float to string format
  }

  String ppmComput(){
    teta = 1-(temperature+273.15)/Tc;
    float pws = Pc*exp((Tc/(temperature+273.15))*(c1*teta +
c2*pow(teta,1.5) + c3*pow(teta,3.0) + c4*pow(teta,3.5) +
c5*pow(teta,4.0) + c6*pow(teta,7.5)));
    float pw = pws*humidity/100;
    float ah = pw*pow(10.0,6.0)/(pressure*10.0 - pw); // computing
// absolute humidity in ppm
    return(String)ah; // float to string conversion of absolute
// humidity data
  }

  void loop() { // display data

```

```

Serial.print(ReadHum(address1));
Serial.print("\t");
Serial.print(ReadTemp());
Serial.print("\t");
Serial.print(ReadPress());
Serial.print("\t");
Serial.print(press_torr());
Serial.print("\t");
Serial.println(ppmComput());

delay(5000);

} // end loop

```

A.2.2 Code running in the CLIENT board

```

#include <WiFiClient.h>
#include <ESP8266WiFi.h>
#include <ESP8266HTTPClient.h>

const char* ssid = "PolySense"; // name of the network
const char* pass = "*****"; // password of the network (not
// shown)

const char* sensor11Data = "http://192.168.0.130/sensor1"; // URL
// path of the HYT271 sensor

void setup() {

    Serial.begin(115200); // initializing serial port

    IPAddress staticIP(192, 168, 0, 133); // static IP address of the
// board
    IPAddress gateway(192, 168, 0, 1); // gateway IP address of the
// client
    IPAddress subnet(255, 255, 255, 0); // subnet mask

    WiFi.config(staticIP, gateway, subnet); // configuring WiFi
// communication
    WiFi.mode(WIFI_STA);
    WiFi.begin(ssid, pass);
    while (WiFi.status() != WL_CONNECTED) {
        delay(500);
        Serial.print(".");
    }
    Serial.println("Connection established");
    Serial.print("IP address: ");

    Serial.println(WiFi.localIP()); // IP address

    delay(500);

}

```

```
void loop() {  
  
    String data11 = httpGETRequest(sensor11Data);  
  
    Serial.print("Sensor1: ");  
    Serial.print(data11);  
    Serial.println("\t");  
  
    delay(5000);  
}  
  
String httpGETRequest(const char* serverName) {  
    WiFiClient client;  
    HTTPClient http;  
  
    // IP address with path or Domain name with URL path  
    http.begin(client, serverName);  
  
    // Send HTTP POST request  
    int httpResponseCode = http.GET();  
  
    String payload = "--";  
  
    if (httpResponseCode > 0) {  
        payload = http.getString();  
    }  
  
    http.end();  
  
    return payload;  
}
```


Bibliography

- [1] Javaid, M.; Haleem, A.; Singh, R. P.; Rab, S.; Suman, R. *Sensors Internationals* 2021, 2, 100110.
- [2] Ali, S.; Singh, R.P.; Javaid, M.; Haleem, A.; Pasricha, H.; Suman, R.; Karloopia, J. *Journal of Industrial Integration and Management*, 2020, 5 (4), 413-425.
- [3] Schmidt, D.; Villalba Diez, J.; Ordieres-Meré, J.; Gevers, R.; Schwiep, J.; Molina, M. *Sensors* 2020, 20 (10), 2860.
- [4] Wang, S., Fang, Y., He, H., Zhang, L., Li, C., Ouyang, J. *Adv. Funct. Mater.* 2021, 31 (5), 2007495.
- [5] Song, Y.; Wang, N.; Hu, C.; Wang, Z. L.; Yang, Y. *Nano Energy* 2021, 84, 105919.
- [6] Yoon, S.; Kim, Y.J.; Lee, Y.R.; Lee, N.E.; Won, Y.; Gandla, S.; Kim, S.; Kim, H.K. *NPG Asia Mater* 2021, 13 (1), 1–4.
- [7] Sampaolo, A.; Menduni, G.; Patimisco, P.; Giglio, M.; Passaro, V.M.N.; Dong, L.; Wu, H.; Tittel, F.K.; Spagnolo, V. *Fuel* 2020, 227, 118118.
- [8] Zhang, L.; Tian, G.; Li, J.; Yu, B. *Appl. Spectrosc.* 2014, 68, 1095–1107.
- [9] Fehér, M.; Martin, P.A. *Spectrochim. Acta A* 1995, 51, 1579–1599.
- [10] Elijah, O.; Ling, P. A.; Rahim, S. K. A.; Geok, T. K.; Arsad, A.; Kadir, E. A.; Abdurrahman, M.; Junin, R.; Agi, A.; Abdulfatah, M. Y. *IEEE Access* 2021, 9, 144438-144468.
- [11] Aali, J.; Rahimpour-Bonab, H.; Reza Kamali, M. *J. Petrol. Sci. Eng.* 2006, 50 (3–4), 161-175.
- [12] Department of Health and Human Services, NIOSH *Pocket Guide to Chemical Hazards*, National Institute for Occupational Safety and Health, 2007.
- [13] Toxicological Review of Hydrogen Sulfide, US Environmental Protection Agency, *Support of Summary Information on the Integrated Risk Information System (IRIS)*, 2003.
- [14] Patimisco, P.; Scamaricio, G.; Tittel, F.K.; Spagnolo, V. *Sensors* 2014, 14, 6165-6206.

- [15] Hodgkinson, J.; Tatam, R. P. *Meas. Sci. Technol.* 2013, 24, 012004.
- [16] Patimisco, P.; Sampaolo, A.; Dong, L.; Tittel, F. K.; Spagnolo, V. *Applied Physics Reviews* 2018, 5, 011106.
- [17] Kosterev, A.A.; Tittel, F.K.; Serebryakov, D.; Malinovsky, A.; Morozov, A. *Rev. Sci. Instrum.* 2005, 76, 043105.
- [18] Kosterev, A.A.; Bakhirkin, Y.A.; Curl, R.F.; Tittel, F.K. *Opt. Lett.* 2002, 27, 1902–1904.
- [19] Ma, Y.; Lewicki, R.; Razeghi, M.; Tittel, F.K. *Opt. Express.* 2013, 21, 1008–1019.
- [20] Dong, L.; Kosterev, A. A.; Thomazy, D.; Tittel, F. K. *Appl. Phys. B* 2010, 100, 627–635.
- [21] Jahjah, M.; Belahsene, S.; Nahle, L.; Fischer, M.; Koeth, J.; Rouillard, Y.; Vicet, A. *Opt. Lett.* 2012, 37, 2502–2504.
- [22] Spagnolo, V.; Patimisco, P.; Borri, S.; Scamarcio, G.; Bernacki, B. E.; Kriesel, J. *Opt. Lett.* 2012, 37, 4461–4463.
- [23] Ba, T. N.; Triki, M.; Desbrosses, G.; Vicet, A. *Rev. Sci. Instrum.* 2015, 86, 023111.
- [24] Waclawek, J. P.; Moser, H.; Lendl, B. *Opt. Express.* 2016, 24, 6559–6571.
- [25] Liu, K.; Guo, X.; Yi, H.; Chen, W.; Zhang, W.; Gao, X. *Opt. Lett.* 2009, 34, 1594–1596.
- [26] Böttger, S.; Köhring, M.; Willer, U.; Schade, W. *Appl. Phys. B* 2013, 113, 227–232.
- [27] Lassen, M.; Lamard, L.; Feng, Y.; Peremans, A.; Petersen, J. C. *Opt. Lett.* 2016, 41, 4118–4121.
- [28] Yi, H.; Liu, K.; Chen, W.; Tan, T.; Wang, L.; Gao, X. *Opt. Lett.* 2011, 36, 481–483.
- [29] Liu, K.; Yi, H.; Kosterev, A. A.; Chen, W.; Dong, L.; Wang, L.; Tan, T.; Zhang, W.; Tittel, F. K.; Gao, X. *Rev. Sci. Instrum.* 2010, 81, 103103.
- [30] Wang, Z.; Wang, Q.; Ching, J. Y. L.; Wu, J. C. Y.; Zhang, G.; Ren, W. *Sens. Actuators, B* 2017, 246, 710–715.

- [31] Spagnolo, V.; Kosterev, A. A.; Dong, L.; Lewicki, R.; Tittel, F. K. *Appl. Phys. B* 2010, 100, 125–130.
- [32] Dong, L.; Spagnolo, V.; Lewicki, R.; Tittel, F. K. *Opt. Express*. 2011, 19, 24037–24045.
- [33] Lewicki, R.; Wysocki, G.; Kosterev, A. A.; Tittel, F. K. *Opt. Express*. 2007, 15, 7357–7366.
- [34] Kosterev, A. A.; Buerki, P. R.; Dong, L.; Reed, M.; Day, T.; Tittel, F. K. *Appl. Phys. B* 2010, 100, 173–180.
- [35] Patimisco, P.; Sampaolo, A.; Bidaux, Y.; Bismuto, A.; Schott, M.; Jiang, J.; Muller, A.; Faist, J.; Tittel, F. K.; Spagnolo, V. *Opt. Express*. 2016, 24, 25943–25954.
- [36] Lewicki, R.; Wysocki, G.; Kosterev, A.A.; Tittel, F.K. *Opt. Expr.* 2007, 15, 7357–7366.
- [37] Wojcik, M.D.; Phillips, M.C.; Cannon, B.D.; Taubman, M.S. *Appl. Phys. B* 2006, 85, 307–313.
- [38] Griffith, W. *J. Appl. Phys.* 1950, 21, 1319.
- [39] Kosterev, A. A.; Bakhirkin, Y. A.; Curl, R. F.; Tittel, F. K. *Appl. Phys. B* 2005, 80, 133.
- [40] Elia, A.; Lugarà, P. M.; di Franco, C.; Spagnolo, V. *Sensors* 2009, 9, 9616–9628.
- [41] Li, J.; Chen, W.; Yu, B. *Appl. Spectrosc. Rev.* 2011, 46, 440–471.
- [42] Blom, F. R.; Bouwstra, S.; Elwenspoek, M.; Fluitman, J. H. J. *J. Vac. Sci. Technol. B* 1992, 10, 19.
- [43] Patimisco, P.; Sampaolo, A.; Dong, L.; Giglio, M.; Scamarcio, G.; Tittel, F.K.; Spagnolo, V. *Sensors and Actuators B* 2016, 227, 539-546.
- [44] Christen, M. *Sens. Actuators* 1983, 4, 554–555.
- [45] Spagnolo, V.; Patimisco, P.; Tittel, F.K. *Mid-infrared Optoelectronics Materials, Devices, and Applications 1st Edition– Chapter 15, Pages 597-659.*
- [46] Lee, M.; Kim, B.; An, S.; Jhe, W. *Sensors* 2019, 19, 2686.
- [47] Sader, J.E. *J. Appl. Phys.* 1998, 84, 64–76.
- [48] Hao, Z.; Erbil, A.; Ayazi, F. *Sens. Actuat. A Phys.* 2003, 109, 156–164.

- [49] Zener, C. *Phys. Rev.* 1938, 53, 90–99.
- [50] Di Gioia, M.; Lombardi, L.; Marzocca, C.; Matarrese, G.; Menduni, G.; Patimisco, P.; Spagnolo, V. *Micromachines* 2023, 14, 619.
- [51] Olivieri, M.; Menduni, G.; Giglio, M.; Sampaolo, A.; Patimisco, P.; Wu, H.; Dong, L.; Spagnolo, V. *Photoacoustics* 2023, 29, 100438.
- [52] Menduni, G.; Zifarelli, A.; Sampaolo, A.; Patimisco, P.; Giglio, M.; Amoroso, N.; Wu, H.; Dong, L.; Bellotti, R.; Spagnolo, V. *Photoacoustics* 2022, 26, 100349.
- [53] Ma, Y. *Appl. Sci.* 2018, 8, 1822.
- [54] Menduni, G.; Sampaolo, A.; Patimisco, P.; Giglio, M.; Dello Russo, S.; Zifarelli, A.; Elefante, A.; Wieczorek, P.Z.; Starecki, T.; Passaro, V.M.N.; Tittel, F.K.; Spagnolo, V. *Appl. Sci.* 2020, 10, 2947.
- [55] Olivieri, M.; Zifarelli, A.; Menduni, G.; Di Gioia, M.; Marzocca, C.; Passaro, V.M.N.; Sampaolo, A.; Giglio, M.; Spagnolo, V.; Patimisco, P. *Appl. Sci.* 2021, 11, 7974.
- [56] Starecki, T.; Wieczorek, P.Z. *Sensors* 2017, 17, 2528.
- [57] J. Karki. Texas Instruments Application Report SLOA033A, September 2020. Available online: <https://www.ti.com/lit/an/sloa033a/sloa033a.pdf>
- [58] Starecki, T. *Int J Thermophys* 2014, 35, 2124–2139.
- [59] Winkovski, M.; Stacewicz, T. *Sci Rep*, 2019, 9, 1838.
- [60] Wieczorek, P.Z.; Starecki, T.; Tittel, F.K. *Appl. Sci.* 2020, 10, 4105.
- [61] Liu, Y.; Lin, H.; Montano, B.A.Z.; Zhu, W.; Zhong, Y.; Kan, R.; Yuan, B.; Yu, J.; Shao, M.; Zheng, H. *Photoacoustics* 2022, 25, 100332.
- [62] Menduni, G.; Zifarelli, A.; Kniazeva, E.; Dello Russo, S.; Ranieri, A.C.; Ranieri, E.; Patimisco, P.; Sampaolo, A.; Giglio, M.; Manassero, F.; Dinuccio, E.; Provolo, G.; Wu, H.; Dong, L.; Spagnolo, V. *Sens. Actuators B Chem.* 2023, 375, 132953.
- [63] Zifarelli, A.; De Palo, R.; Patimisco, P.; Giglio, M.; Sampaolo, A.; Blaser, S.; Butet, J.; Landry, O.; Müller, A.; Spagnolo, V. *Photoacoustics* 2022, 28, 100401.
- [64] Liberatore, N.; Viola, R.; Mengali, S.; Masini, L.; Zardi, F.; Elmi, I.; Zampolli,

- S. *Sensors* 2023, 23, 270.
- [65] Zifarelli, A.; Menduni, G.; Giglio, M.; Elefante, A.; Sukhinets, A.; Sampaolo, A.; Patimisco, P.; Fangyuan, S.; Chongwu, W.; Wang, Q.J.; et al. *Front. Environ. Chem.* 2022, 3, 926233.
- [66] Li, B.; Feng, C.; Wu, H.; Jia, S.; Dong, L. *Sens. Actuators B Chem.* 2022, 358, 131510.
- [67] Shang, Z.; Li, S.; Li, B.; Wu, H.; Sampaolo, A.; Patimisco, P.; Spagnolo, V.; Dong, L. *Photoacoustics* 2022, 26, 100363.
- [68] Zurich Instruments – White Paper. Available online: https://www.zhinst.com/sites/default/files/li_primer/zi_whitepaper_principles_of_lock-in_detection.pdf
- [69] Stanford Research Systems - Application Note. Available online: <https://www.thinksrs.com/downloads/pdfs/applicationnotes/AboutLIAs.pdf>
- [70] AD8067, High Gain Bandwidth Product, Precision Fast FET™ Op Amp. Analog Devices Inc. Available online: <https://www.analog.com/en/products/ad8067.html>
- [71] Lin, H.; Liu, Y.; Lin, L.; Zhu, W.; Zhou, X.; Zhong, Y.; Giglio, M.; Sampaolo, A.; Patimisco, P.; Tittel, F.K.; et al. *Appl. Spectrosc. Rev.* 2022, 57, 1–23.
- [72] Levy, R.; Duquesnoy, M.; Melkonian, J.-M.; Raybaut, M.; Aoust, G. *IEEE Trans. Ultrason. Ferroelectr. Freq. Control* 2020, 67, 1230–1235.
- [73] Mehdi Alem. Frequency – Domain Response of Lock-In Filters. Available online: <https://www.zhinst.com/europe/en/blogs/frequency-domain-response-lock-filters>
- [74] Zurich Instruments; MFLI User Manual. Available online: https://docs.zhinst.com/pdf/ziMFLI_UserManual.pdf
- [75] Current Noise in FET Input Amps. Analog Devices Inc. Available online: <https://www.analog.com/en/analog-dialogue/raqs/raq-issue-174.html>
- [76] Villa, T.F.; Salimi, F.; Morton, K.; Morawska, L.; Gonzalez, F. *Sensors* 2016, 16, 2202.
- [77] Aasen, H.; Honkavaara, E.; Lucieer, A.; Zarco-Tejada, P.J. *Remote Sens.* 2018, 10, 1091.

- [78] Wu, H.; Dong, L.; Zheng, H.; Yu, Y.; Ma, W.; Zhang, L.; Yin, W.; Xiao, L.; Jia, S.; Tittel, F.K. *Nat. Commun.* 2017, 8, 15331.
- [79] Yin, X.; Gao, M.; Miao, R.; Zhang, L.; Zhang, X.; Liu, L.; Shao, X.; Tittel, F.K. *Opt. Express.* 2021, 29, 34258.
- [80] Di Gioia, M.; Menduni, G.; Zifarelli, A.; Sampaolo, A.; Patimisco, P.; Giglio, M.; Marzocca, C.; Spagnolo, V. *Proc. SPIE*, 12430, 124300V (2023).
- [81] Aoust, G.; Levy, R.; Bourgeteau, B.; Le Traon, O. *Sens. Actuat. A Phys.* 2016, 238, 158–166.
- [82] Serebryakov, D.V.; Cherkun, A.P.; Loginov, B.A.; Letokhov, V.S. *Rev. Sci. Instrum.* 2002, 73, 1795.
- [83] Friedt, J.-M.; Carry, É. *Am. J. Phys.* 2007, 75, 415–422.
- [84] The Quartz Crystal Model and Its Frequencies. Technical Note 32, Rev. A. *Statek*. Available online: <https://statek.com/wpcontent/uploads/2018/03/tn32.pdf>
- [85] Elefante, A.; Menduni, G.; Rossmadl, H.; Mackowiak, V.; Giglio, M.; Sampaolo, A.; Patimisco, P.; Passaro, V.M.N.; Spagnolo, V. *Sensors* 2020, 20, 2935.
- [86] Karki, J. Texas Instruments Application Report SLOA054E. Available online: https://www.ti.com/lit/an/sloa054e/sloa054e.pdf?ts=1695628370127&ref_url=https%253A%252F%252Fwww.google.it%252F
- [87] Carter, B. Texas Instruments Application Note SLOA072. Available online: <https://www.ti.com/lit/an/sloa072/sloa072.pdf?ts=1695576308499>
- [88] ST Microelectronics Application Note AN5798. Available online: https://www.st.com/resource/en/application_note/an5798-how-to-improve-the-robustness-of-operational-amplifiers-against-electromagnetic-interferences-emi-stmicroelectronics.pdf
- [89] Carter, B. Texas Instruments Application Note SLOA099. Available online: <https://www.ti.com/lit/an/sloa099/sloa099.pdf>
- [90] THS4567 Texas Instruments Datasheet. Available online: https://www.ti.com/lit/ds/symlink/th4567.pdf?ts=1695629008904&ref_url=https%253A%252F%252Fwww.google.it%252F
- [91] Scandurra, G.; Cannatà, G.; Giusi, G.; Ciofi, C. *IEEE International*

Instrumentation and Measurement Technology Conference (I2MTC) Proceedings, Pisa, Italy, 2015, pp. 1871-1876.

- [92] Peng, P.; Hao, L.; Ding, N.; Jiao, W.; Wang, Q.; Zhang, J.; Wang, R. *Rev. Sci. Instrum.* 2015, 86, 116105.
- [93] Shmaliy, Y. S.; Marienko, A.V.; Ibarra-Manzano, O. G.; Rojas-Laguna, R. 2002, *Frequency Control Symposium and PDA Exhibition. IEEE International*. DOI: 10.1109/FREQ.2002.1075965.